Constraints on the ability of Cl- and F- bearing aqueous fluid to dissolve and transport trace elements (Y, Nb, Zr) in subduction zone environments

by

Elizabeth Anne Tanis

A dissertation submitted in partial fulfillment
of the requirements for the degree of
Doctor of Philosophy
(Earth and Environmental Sciences)
in the University of Michigan
2014

Doctoral Committee:

Associate Professor Adam C. Simon, Chair
Professor Rebecca A. Lange
Research Scientist Gordon Moore
Assistant Professor Donald J. Siegel
Professor Youxue Zhang

For my amazing family

ACKNOWLEDGEMENTS

I would first and foremost like to thank my parents, Belle and Fred Tanis, without their love, encouragement, understanding and believing in me, I could not have achieved anything, and my brother, Erick, for inspiring me everyday to persevere through the challenges that life brings.

I would like to express gratitude to my advisor, Adam Simon. His guidance during the past four years was instrumental to the success of this work. I would also like to express my gratitude to Oliver Tschauner, who has supported and encouraged me from physics to geology. I wish to acknowledge my committee members, Rebecca Lange, Youxue Zhang, Gordon Moore, Donald Seigal for their helpful guidance and suggestions along the way. I am also greatful to all the faculty, staff and students from the geology department at UNLV, specifically Pamela Burnley and Gene Smith and from the Earth and Environmental Sciences Department at University of Michigan. Thank you for all of your collaboration and encouragement. I would like to thank the APS beamline staff at HPCAT for their help and support during my experiments, especially, Tom Toellner, Paul Chow and Yuming Xiao.

Finally, I would like to thank my friends for their support. You give true meaning to "your friends become your family, wherever you live."Thank you to my long time friends, Ashley Ramirez, Brandon Burke, Jessica Colvin, Christin Dostalek for checking up on me and reminding me that there is more to life then school. I would like to thank Laura Bilenker, my housemate, officemate, labmate, soulmate and Laura Waters, my adopted academic older sister for your endless support and motivation.

My Las Vegas family Kelly Robertson, Jordan Drew, Swapan Sahoo and Denise Kilburg. My Michigan family whom helped me survive the winters and made life more enjoyable: Xiaofei Pu, Tom Hudgins, Joe El Aldi, Samantha Reeves, Trever Hines, Lorena Medina Luna, Sara Walker, our Germs, Jaayke and Adrian and our Frenchies, Anaïs and Thomas.

TABLE OF CONTENTS

LIST OF FIGURES

Figure

LIST OF TABLES

Table

LIST OF APPENDICES

Appendix

ABSTRACT

Constraints on the ability of Cl- and F- bearing aqueous fluid to dissolve and transport trace elements (Y, Nb, Zr) in subduction zone environments

by

Elizabeth Anne Tanis

Chair: Adam C. Simon

Geologic source regions are often characterized by their trace element concentrations. For example, arc magmas show a depletion in high field strength elements (HFSE) relative to mid ocean ridge basalts. This depletion has been the topic of many debates, as arc petrologists largely attribute this to residual minerals (e.g., rutile) in the source sequestering these elements, while metamorphic petrologists studying exhumed terrains find evidence of trace element mobility. In addition, previously published experimental studies of the partitioning of trace elements involving aqueous fluids are often conducted at pressure and temperature conditions not appropriate for slab-mantle wedge conditions and are extrapolated to higher pressures (>2 GPa) and lower temperatures (<700°C). Therefore, constraining mass transfer of the rare earth elements (REE) and HFSE from subducted oceanic crust and metasediments to the mantle wedge is fundamental toward interpreting and modeling processes that affect trace element mobility in subduction zone environments.

This dissertation discusses the experimental techniques, results and application, to quantitatively determine trace element concentrations and mineral solubilities in aqueous fluids at geologically relevant conditions (0.5-6 GPa and 250-900°C). The

effect of multicomponent aqueous fluids (e.g., H_2O + Cl, F, K, Na) on the solubility of xenotime and rutile are investigated. Experimental methods to achieve pressure and temperature include a hydrothermal diamond anvil cell in conjunction with synchrotron x-ray fluorescence to probe the fluid directly, and traditional mineral mass loss experiments using a piston cylinder apparatus. The results indicate that fluid composition exerts the greatest control on xenotime and rutile solubility in aqueous fluids, and that increasing temperature has a positive, albeit less pronounced, effect.

The results are consistent with field studies of exhumed terranes, which demonstrate that normally fluid immobile minerals and elements (HFSE and REE) are mobile over short (e.g., mm to m), and possibly long (e.g., tens of m) distances. Given that each arc has a slightly different rate, angle, and sediment deposit during subduction; the order of magnitude variation of HFSE and REE from arc rocks may likely be a function the composition of fluids evolved during prograde metamorphism.

CHAPTER 1

Introduction

1.1 Context and Motivation

Subduction zones are the Earth's largest recycling systems. Subduction is a process that occurs at convergent boundaries where one tectonic plate sinks under another tectonic plate into the Earths mantle, returning oceanic lithosphere, terrigenous sediments, and seawater to the mantle. Increasing pressure and temperature (e.g., high pressures, >2.5 GPa; 250-800°C) along the subduction path result in a series of metamorphic transitions. Hydrothermally altered basalt metamorphoses to greenschist then to lawsonite-bearing blueschist and finally to eclogite. During these transitions water and dissolved solutes (aqueous fluid) are continuously being released. As some of the aqueous fluid travels from the subducting plate into the mantle wedge that overlies the subducting ocean plate, the melting solidus of the mantle is lowered, which triggers partial melting of the mantle. The partial melting generates basalt that rises into the overlying plate, and leading to arc volcanism and the formation of plutons (Marshak, 2004; Aizawa et al., 1999). Meanwhile, material that is not transferred into the mantle wedge remains in the subducting slab and sinks further into the mantle (Stern, 2002) or in some cases (e.g., Tian Shan, Monviso, Franciscan) is exhumed back to the surface.

The concentration/distribution of elements in arc environments is affected by the

partitioning of elements between mineral phase assemblages, the partial melt and/or source fluid. The chemical and physical characteristics of an element determines how compatible or incompatible it is in a mineral, compared to a coexisting liquid or volatile phase. An element compatible with a mineral will prefer a solid phase whereas an incompatible element will prefer a liquid or volatile phase. The geochemical signature is comprised of trace elements, defined as elements present at less than 1000 parts per million (ppm or μg g^{-1}) within a rock. Common trace elements categories include large ion lithophile elements (LILE), high field strength elements (HFSE) and rare earth elements (REE). Mid-ocean ridge basalts (MORB) are depleted in LILE, (e.g., Rb, Ba, Sr, K) whereas ocean island basalts (OIB) are enriched in LILE (Figure 1.1, Hawksworth, 1993). The fluids causing partial melting during subduction have been postulated to leave an imprint on the trace element patterns of arc volcanic and plutonic rocks (Bebout et al., 1999; Kay et al., 1984) resulting in an increase in the LILE and depletion of HFSE, thus creating a characteristic trough or dip when plotted in a MORB normalized diagram (Figure 1.1, Hawksworth, 1993).

Throughout the past decades there still remain different viewpoints on the nature and role of fluids during subduction contributing to the characteristic depletion in HFSE found in arc rocks and more broadly trace element mobility and mineral solubility (Saunders et al., 1980; Kelemen et al., 1990; McCulloch and Gamble, 1991). The source of this debate can be attributed to incomplete knowledge of trace element mobility between minerals, melts and fluids during the subduction process. Natural samples of exhumed metamorphic terranes are limited by their availability and are often hampered by retrograde overprinting acquired during exhumation or water loss (Philippott and Selverstone, 1991; Scamberelli and Philippot, 2001; Gao et al., 2007). Experiments are complicated by replicating high-pressure high-temperature conditions, retrieval of fluid and solid phases, and extrapolation of the data to relevant time scales (e.g., slow kinetics). Although much work has been done, some fundamen-

tal questions remain: Why does the metamorphic rock record measure major fluid and trace element transfer and arc rocks do not? What is the cause of the HFSE depletion in the arc rock signature (especially if HFSE can be mobile)? If the HFSE are being mobilized, but do not make it into the mantle wedge, where do they go? What are the mechanisms, volumes and compositions of fluids that are released during subduction and how do they play a role in trace element mobility? The problem broadly falls into the hands of arc petrologists studying surface samples of arc volcanoes and plutons; metamorphic petrologists studying exhumed blueschist/eclogite terranes; and experimentalists. Experiments can be designed to investigate solubility and/or partitioning between trace elements and minerals/fluids/melts at the conditions at which these subduction processes occur. Fluid-mediated element transfer processes that occur during subduction recycling are characterized by observations and are quantified by these experiments. Both observations and experiments are fundamental to accurately model and thus predict element partitioning and distribution. At this stage, there is a need for more experimental data that provide constraints on fluid compositions, mineral solubility, mineral/melt/fluid partitioning and the mechanisms behind these processes; that exhibit reproducibility; and that can be directly applied to the pressure and temperature conditions during subduction.

Broadly speaking, arc petrologists examine the geochemistry, textures, and mineral assemblages of igneous rocks collected from the near-surface. They have developed three working hypotheses to explain the geochemical signature of arc magmas. The first is that ascending aqueous fluids from the slab are enriched in LILE and LREE, relative to HFSE, and thus transfer this signature to partial melts produced in the mantle. The magma produced from the partial melts interacts with the mantle and/or depleted upper mantle wall rock during ascent and relative to the REE, the HFSE fractionate from olivine or orthopyroxene. (Hawkesworth, 1993a,b; Kelemen et al., 1990; Foley et al., 2000; Audétat and Keppler, 2005). The second hypothesis

is that melt extraction from the mantle at a back-arc spreading center depletes the mantle in HFSE prior to its interaction with slab-derived fluid at the base of the arc volcano plumbing system (McCulloch and Gamble, 1991; Woodhead et al., 1993). This hypothesis requires the mantle wedge to be re-fertilized by LILE and LREE enriched fluids during melt extraction. The downward motion of the subducted slab drags this depleted mantle material into the mantle wedge above the slab, yielding a strong depletion of HFSE during subsequent partial melting of the depleted mantle. The third and most widely accepted hypothesis is that rutile in the subducted slab retains the HFSE during slab dehydration; hence, rutile moderates the HFSE chemistry of fluids that ascend into the mantle (Saunders et al., 1980; Green, 1981; Brophy and Marsh, 1986; Ryerson and Watson, 1987; Morris et al., 1990). The resulting trace element abundance patterns are preserved in arc magma owing to the very low abundances of the HFSE in the mantle and slab-evolved fluid.

In contrast, metamorphic petrologists examine exhumed terranes. These are rocks from various stages of the subduction process that are brought to the surface which contain a prehistoric imprint that can be analyzed to determine the rock petrogenesis. There is a growing body of evidence (i.e., hydrothermal alteration textures, veins formed from fluids, and fluid inclusions) that demonstrates HFSE and REE are mobile in aqueous fluids evolved during prograde metamorphic dehydration reactions that occur during subduction. Spandler et al. (2011) reported that high-pressure veins cutting through eclogite facies ($\sim$ 2 GPa, $\sim$ 600°C) Fe-Ti metagabbros in the Monviso Lago Superiore region were enriched in rutile. They suggested that subsolidus influx of multiple generations of internally- and externally-derived fluid were the cause of the rutile enriched veins. The veins contain rutile, garnet, talc and accessory zircon, which were assumed to co-precipitate from aqueous fluid because they were found in the same vein. They concluded that the composition of the externally derived fluid was rich in Cr, Ni, B, As, Sb and light and middle rare earth elements. Dehydration

of serpentinite was invoked as the most plausible source of fluid that would provide multiple episodes of fluid influx and produce the chemistry of the veins (Spandler et al., 2011). While Nb and other elements such as Ti, Zr, Hf, Cr and Ni, are generally regarded as fluid-immobile in subduction zone environments, Spandler et al. (2011) pointed out that the chemical signatures of the veins at Monviso require fluid mobility of Nb and these other elements. In fact, high salinity fluid inclusions have been reported for the Monviso gabbros, consistent with the presence of a saline fluid during prograde metamorphism (Barnicoat and Cartwright, 1997; Philippot et al., 1998).

Gao et al. (2007) reported the presence of rutile crystals in hydrothermal veins located at the contact between blueschist and eclogite in exhumed rocks in the Tian Shan complex, northwest China. These hydrothermal veins were interpreted by Gao et al. (2007) as evidence for local (i.e., cm to m) transport of HFSE in aqueous fluid evolved during prograde metamorphic dehydration. The eclogite and vein underwent similar prograde conditions of $\sim$1.9 GPa and 500 to 600°C. These authors reported the presence of aqueous fluid inclusions with salinities of 1.57 to 4.49 wt% NaCl equivalent, and concluded that Nb, Ti and Ta were scavenged and fractionated from Zr and Hf (which were sequestered by titanite) by aqueous fluid evolution and migration from metamorphic dehydration of blueschist to eclogite. They also reported that rutile and apatite co-precipitated in the hydrothermal veins. Precipitation of Cl- and F-bearing apatite would result in rapid depletion of these halogens in the fluid, resulting in destabilization of HFSE-fluorine and/or HFSE-chlorine complexes in the fluid. In turn, this would result in precipitation of rutile, which would sequester Nb and other HFSE from the fluid.

Metamorphic petrologists and arc petrologists agree that rutile is the dominant carrier of Nb and Ta, containing more than 90% of the Nb and Ta budget of eclogites (Rudnick et al., 2000; Zack et al., 2002; Spandler et al., 2003; Schmidt et al., 2009)

and metasomatic, rutile-bearing peridotites (Kalfoun et al., 2002). Experimental studies of rutile solubility in pure H_2O also demonstrate low solubility contributing to the acceptance of the third hypothesis (Audétat and Keppler, 2005; Tropper and Manning, 2005). However, the addition of dissolved Na-Al silicates, Cl or F to the fluid has been experimentally shown to increase mineral solubility, specifically rutile (Rapp et al., 2010; Antignano and Manning, 2008; Hayden and Manning, 2011; Manning et al., 2008), but also for quartz, hornblende (Wu and Konga, 2013), monazite and xenotime (Tropper and Manning, 2011, 2013; Tanis et al., 2012).

1.1.1 Fluid mobilization and composition during subduction

There is a wealth of isotopic and geochemical evidence that arc magmas contain a significant proportion of slab-derived volatiles and trace elements (Perfit et al., 1980; Hawkesworth et al., 1993; Pearce and Peate, 1995). Previous research has demonstrated that the liberation of water is strongly linked to the breakdown of hydrous phases during the blueschist to eclogite transition (Peacock, 1993; Schmidt and Poli, 1998). In contrast, it remains unclear whether or not trace element liberation is related to the breakdown and/or solubility of trace element-rich host phases and/or the scavenging of trace elements by aqueous fluid (i.e., trace element partitioning) that equilibrate with a trace-element-bearing mineral. Scambelluri and Philippot (2001) concluded that small-scale fluid cycling has the ability to mobilize trace elements in subduction zones. Small scale fluid cycling is defined as the episodic release of low volumes of fluids. The fluid inclusions they investigated were found in primary relict kyanite and omphacite, and contained variable amounts of solutes (e.g., chlorides with 17-21 and 32-45 wt% NaCl equivalent) with minor CO_2 and N_2. These fluids represent remnants of prograde dehydration and the early stages of eclogitization. The fluid inclusions also contained a wide assortment of daughter minerals (e.g., calcite, rutile, apatite, monazite, etc.) contributing up to 50% by weight of dissolved solutes,

which suggest element fractionation during hydration of the host rock (Svensen et al., 1999). The field evidence they provided suggests increased mineral solubility was due to silicate-rich aqueous solutions. The high amount of dissolved ligands cause the geochemical behavior and transport capacity to approach that of and perhaps eventually produce a melt phase. The experimental work showing solubility of silicate components in fluids at high pressures supports this (Brenan et al., 1995, Manning, 1996, 1998; Hayden and Manning, 2011). However, natural examples of inclusions trapping such fluids and quantitative analyses of major and trace element compositions are scarce. Due to the small scale cycling of fluids, Scambelluri and Philippot (2001) propose that exhumed high pressure rocks have trapped only a fraction of the fluid and therefore do not accurately represent the total amount of fluid released to the slab/mantle wedge, with the remainder returned to the surface via magmatism.

Spandler et al. (2003) proposed a different model for the redistribution of trace elements in the slab. During the transition from lawsonite blueschist to eclogite (1-1.4 GPa, 300-500°C), about 75% of the H_2O content is lost. They concluded that trace elements are released by mineral breakdown reactions during early stages of prograde metamorphism, and are immediately redistributed into new host mineral phases (i.e., rutile, allanite, zircon). Due to the fact that these important host minerals are stable over a large pressure-temperature range, breakdown reactions of the trace element host phases do not occur. Trace element mobility is then dictated by trace element partitioning between the mineral host phase and the aqueous fluid, which is controlled by the diffusivity of the trace element in the mineral host phase. Furthermore, the data from Spandler et al. (2003) indicate that at higher pressures (>1.4 GPa) and in the temperature range of 550-600°C, removing large quantities of the trace elements is not possible due to the low (e.g., 3%) amount of fluid generated by further dehydration of mafic rocks. However, they do not rule out the possibility that significant trace element transport from the slab can be possible at higher temperatures and/or in

zones with very high fluid/rock ratios, and advocate for an alternative model based on fluxing of fluid to transfer trace elements from the slab to the mantle wedge. The fluid is derived from the dehydration of lawsonite, amphibole, chlorite and serpentinite and may flow into relatively hot zones in the slab, such as the slab/mantle-wedge interface (Bebout and Barton 1989; Peacock 1993). However, the elements that are distinctively enriched in arc magmas are a consequence of trace elements (e.g., LILE) being stripped from mafic rocks and/or fluid-assisted partial melting of sediments from the slab.

In contrast to the two previous ideas, John et al. (2008) suggest a hypothesis where fluids in high-pressure rocks are able to mobilize trace elements, despite low mineral solubilities, owing to the fluid movement along high permeability reaction zones. The nature of the fluid-rock ratio, non-steady state flow, and high concentrations of dissolved components, such as Na, Si and F, are the controlling factors in trace element mobility versus the previous studies which focus primarily on trace element partitioning and mineral assemblages.

One common attribute among the aforementioned studies, is the emphasis that slab-derived fluids are not pure H_2O, but rather contain significant amounts of alkalis (Na, K), halogens (Cl, F) and aluminosilicate components (i.e., Si, Al) (Giaramita and Sorensen, 1994; Scambelluri et al., 2001; Poli and Schmidt, 2002; Breeding 2004; Manning 2004; Sharp and Barnes, 2004; Frezzotti, 2012; Kawamoto, 2013). Overall, trace element transport in the slab is complex and might be more significant in local areas where there are high fluid fluxes and chemical gradients between fluids and rock, and where fluids are channelized into pathways with high fluid extraction rates (Spandler et al., 2003, 2004; Spandler and Hermann, 2006; Gao et al., 2007; Zack and John, 2007; John et al., 2008; Beinlich et al., 2010). The knowledge of parameters that control trace element distribution and transport requires experimental work that mimics these processes. However, solid/fluid trace element partition coefficients and

diffusion data at realistic parameters (e.g., P-T-X during subduction) are generally scarce and have not kept pace with the analytical techniques (Keppler, 1996; Brenan et al., 1998; Johnson and Plank, 1999; Najorka et al., 1999; Melzer and Wunder, 2000; Blundy and Wood, 2003; Kessel et al., 2005).

1.1.2 How to model fluid composition and transport of subduction zone rocks?

Van Hinsberg (2010) demonstrated that the composition of fluids, and their trace element content in particular, could be reconstructed from the mineral composition when mineral/fluid partition coefficients are known. As a mineral grows in an aqueous environment, its composition will reflect that of the surrounding fluid through characteristic partitioning of trace elements. After the mineral is separated from the fluid, it can preserve this information. Given partition coefficients for appropriate physical and chemical conditions (e.g., pressure, temperature), the fluid composition can be reconstructed. Minerals from the subducting slab, exhumed from within Earth by the actions of plate tectonics, allow the compositions of fluids released during subduction to be qualitatively determined. This provides insight into the elements released during slab dehydration and helps to constrain the element fluxes of the mantle and crust associated with subduction. However, precise mineral/fluid partition coefficients for relevant pressure-temperature conditions are required.

The residence of trace elements in mantle rocks is an important factor that must be taken into account in geochemical models of subduction processes. Modeling based on the experimentally determined phase diagrams and mineral/melt partition coefficients can approximate the behavior of elements that largely reside in modally abundant minerals (e.g., olivine, orthopyrxene, clinopyroxene, garnet) during melting and metasomatism (Van Hinsberg, 2010; Shervais and Jean, 2012). However, melting relationships and partitioning values of accessory phases are poorly known. Even

small amounts of trace element-rich phases, such as allanite, monazite and rutile, in reacting rocks might govern the trace element budget during metamorphism (e.g., Hermann, 2002; Hermann and Rubatto, 2003), and thus influence the composition of slab-derived fluids and arc volcanics (e.g., Plank et al., 2009). Such models (e.g., Van Hinsberg, 2010; Shervais and Jean, 2012) depend critically on experimentally determined partition coefficients for accessory phases from select seminal papers such as Brenan et al. (1995); Keppler (1996); Ayers, (1998); Stalder et al. (1998); and Green, (2003). The results from these seminal papers are sometimes contradicitory and also suggest that partitioning may strongly depend on volatile concentration and other minor components. The ability to model the mobility of trace elements in subduction zone environments is further challenged by the fact that almost all experimental data for the partitioning of trace elements between mineral and fluid phases were generated at P-T-X conditions that do not overlap with prograde fluid evolution in such environments.

1.1.3 Experimental Paradox: Closing the P-T-X gap and the link between methods

The piston-cylinder apparatus has traditionally been used to experimentally determine mineral solubility at high pressures (0.5-3 GPa) and temperatures (500-1500°C) by using the mass-loss recovery method (Ayers and Watson, 1991, 1993; Ayers et al., 1992; Tropper and Manning, 2005; Antignano and Manning, 2008; Rapp et al., 2010; Hayden and Manning, 2011), as well as element partitioning by analyzing the trace elements in the minerals and melts/fluids (Green and Pearson, 1987; Brenan et al., 1994; Stalder et al., 1998; Foley et al., 2000; Green and Adam, 2003). Figure 1.2 demonstrates the pressure-temperature pathways of hot and cold subduction, modeled after Hacker (2008) and the pressure-temperature regime of experiments conducted on rutile solubility. In brief, solubility experiments contain a single mineral

and fluid in a capsule, the sample is run for several hours to days at a specific pressure-temperature condition and is then rapidly quenched. The crystal is weighed before and after the experiment to determine the mass loss, and the solubility of the mineral in the fluid is calculated. These experiments are often plagued with the precipitation of transport crystals, due to thermal gradients or small quench crystals, both of which can be difficult to weigh, and thus add uncertainty to the mass loss calculations. To counter the problem of transport/quench crystals, a fluid permeable double capsule or envelope technique was developed to separate the main crystal from the fluid. If the experiment contains a melt phase, the rapid quenching results in a glass and the mineral(s)/melt or fluid can be analyzed by instrumental techniques (e.g, EMPA, LA-ICP-MS, SIMS, etc.) to determine the relative trace element concentrations, and thus the partition coefficients. However, there is often difficulty separating out the fluid/melt phase from the solid phase. To address this problem, Baker and Stolper, (1994) developed a diamond trap technique in which, the pore space between the diamond crystals was preserved at high pressure-temperature conditions, so that the fluid was able to communicate with the solid starting material throughout the experiment. During quenching the dissolved silicate material precipitated into the pore space between the diamond grains and was physically separated from the residual phases (Stalder et al., 1998; Kessel et al., 2005).

By using a hydrothermal diamond anvil cell (HDAC; Basset et al., 1993, 2000, 2003; Chou, 2008; Smith 2009), a larger pressure range (e.g., 0.01- 20 GPa) than the piston cylinder can be achieved. Furthermore, solubility and speciation measurements can be done in situ. Direct observations can be made visually (Shen and Keppler, 1997; Audétat and Keppler, 2005) or by using spectroscopic techniques such as synchrotron radiation x-ray florescence, (Bureau, 2003, 2007; Sanchez-Valle et al., 2003, 2004; Schmidt et al., 2003, 2006, 2007, 2010; Manning et al., 2008; Borchert et al., 2009, 2010; Stechern, 2009; Tanis et al., 2012, 2014 In Review) and Raman

spectroscopy (Anderson et al., 2002; Wilke et al., 2012; Louvel et al., 2013; Sanchez-Valle, 2013). For example, Sanchez-Valle et al. (2003) reported that the dissolution of strontianite into the fluid increased as a function of increasing pressure and temperature. Schmidt et al. (2006) investigated the solubility of zircon in H_2O + HCl + SiO_2 fluids and found that the solubility of zircon decreases with increasing temperature. Manning et al. (2008) reported that the solubility of rutile was positively correlated with the concentration of dissolved $NaAlSi_3O_8$. Stechern et al. (2009) measured the solubility of zircon in aqueous fluid that contained variable concentrations of dissolved HCl and $Na_2Si_2O_5$ and showed that there was no correlation between the solubility of zircon and the concentrations of HCl and $Na_2Si_2O_5$ in the fluid. Many of these studies used an HDAC configuration that was designed with a cylindrical recess in the lower anvil which permitted collection of the element specific fluorescence signal specifically from fluid in the recessed part of the chamber; however, this limits the maximum achievable pressure (e.g., <1.5GPa).

In this dissertation, higher pressures (e.g., 0.5-6.5 GPa) were achieved by using un-modified diamonds. Also, the solubility of rutile was determined by doping it with Zr and assuming congruent dissolution because direct measurement of Ti was not possible due to the low binding energy of Ti. The energy of the synchrotron beam used was 27 keV, which is high enough to excite the K_α energy of Nb=16.6 keV and Zr=15.7 keV, respectively. This method could be applied to many mineral systems where the main elements are below the detectable K_α binding energy. Due to the in situ analytical advantage, use of the HDAC has many future possibilities to enhance studies on of mineral solubility and element speciation in aqueous fluids It has the ability to achieve a broad pressure (0.01- 20 GPa) and temperature (50-1200°C) range that is unachievable with the piston cylinder and has removed some of the complications with quench crystals and sample retrieval.

Early experiments investigated simple systems such as rutile and water (Ayers

and Watson, 1991, 1993; Ayers et al., 1992; Tropper and Manning, 2005; Antignano and Manning, 2008) and have developed to become more complex by including multi-component mineral, melt and fluid phases (Rapp et al., 2010; Hayden and Manning, 2011, Louvel et al., 2013, 2014). The diligence of experimental petrologists has contributed vastly to the database of partition coefficients and solubility; however, more work is required to close the gap between what P-T-X is achievable experimentally and what is relevant to natural systems. There remain a limited number of partitioning and mineral solubility experiments that are very specific. The work from this dissertation has expanded the P-T-X window for rutile and xenotime solubility and given valuable insight to the important role of adding components such as, Cl and F, to the fluid. Yet, more experiments and method development are required to provide a complete dataset to be used to model the relative mobility of trace elements in fluid-bearing magmatic and metamorphic systems. This is imperative to understanding the origin of the variation of absolute element abundances and element ratios in subduction zone settings.

The goal of this dissertation is to produce new experimental data that quantify the following aspects of trace element mobility during subduction fluid migration:

1. The mobility of REE (by using Y as a proxy) and HFSE (Nb and Zr) in aqueous fluid from host minerals such as xenotime (YPO_4) and rutile (the primary host for HSFE) during slab dehydration (1 to 6 GPa and 300 to 900°C)

2. The effect of multicomponent fluids (e.g., H_2O + Cl, F, K, Na) on the solubility of xenotime and rutile.

1.2 Thesis Overview

In order to generate new experimental data, high pressure, high temperature experiments were conducted by using an HDAC and a piston cylinder press. The analytical methods of synchrotron x-ray fluorescence and mineral mass loss were used

to measure the solubility of xenotime and rutile that contain key trace elements (Y, Nb, Zr) in aqueous fluids containing H_2O with added F, Cl, K, Na and associated HCl. These experiments constrain the solubility of important minerals that carry geochemical tracers in aqueous fluid as a function of pressure, temperature and fluid composition.

Each of the subsequent chapters of this dissertation were written as original manuscripts already published, submitted or intended for submission in a peer reviewed scientific journal. A summary of the manuscript, co-authors, dates of submission, and journals to which the manuscripts were /will be submitted are described in brief below.

Chapter 2 discusses the solubility of xenotime in a 2 *M* HCl aqueous fluid investigated by using a HDAC and and in situ SXRF. The concentration of yttrium (Y), an important trace element often used as a proxy for the heavy REE in geologic systems, was quantified from 1.2 to 2.6 GPa and 300 to 500°C. These new data, combined with published data constrain the effects of pressure and temperature and fluid composition on the ability of aqueous fluid to scavenge and transport Y, and by analogy the HREE. Although the physical properties of Y are similar to the high field strength elements, Y exhibits geochemical behavior that is analogous to the heavy rare earth elements (HREE). The data indicate that the effect of temperature on the solubility of xenotime in aqueous fluid decreases with increasing pressure. The concentration of Y also decreases with increasing fluid density. If xenotime solubility as a function of pressure and temperature can be applied to the extraction of yttrium from slab material during devolatilization, then our data suggest that the ability of aqueous fluid to scavenge yttrium, and by analogy the HREE, is not markedly affected by pressure variations at conditions at the base of arc volcano plumbing systems. The data indicate that HCl, relative to NaCl, has a greater influence on the solubility of xenotime.

The chapter was co-authored by Dr. Adam Simon of the University of Michigan and Dr. Oliver Tschauner of the University of Nevada Las Vegas, whom helped with collection and interpretation of the data. Drs. Paul Chow, Yuming Xiao, and Guoyin Shen of APS-HPCAT, Carnegie Institute of Washington, whom assisted in the beamline setup and collection of data. Dr. John Hanchar of the Department of Earth Sciences, Memorial University of Newfoundland, whom synthesized the xenotime crystals. Dr. Mark Frank of Department of Geology and Environmental Geosciences, Northern Illinois University, whom provided expertise in the use of the HDAC. This chapter was published in American Mineralogist, volume 97, pages 1708-1713 in 2012.

Chapters 3 and 4 focus on the role of rutile (TiO_2), which has been proposed as an important host for HFSE such as, Nb and Zr, in metamorphic and subduction zone environments. Chapter 3 investigates the effect of ligands on the mobility of Nb from Nb- bearing rutile to the aqueous fluid by adding 10 and 20 wt% NaCl, and 4 wt% NaF to the fluid phase. Nb concentrations in the fluid were constrained by using two complementary experimental techniques: (1) A HDAC in conjunction with SXRF to probe the fluid directly, and (2) a Griggs type piston cylinder apparatus in conjunction with traditional mass loss experiments. The experimental techniques achieved pressure and temperature conditions directly applicable to fluid evolution during the blueschist to eclogite transition (e.g., 1 to 6.5 GPa, 300-700°C). Our data show that the addition of dissolved NaCl, or NaF to H_2O results in the increase of Nb solubility in dense aqueous fluids similar to those released during subduction.

This chapter was co-authored by Dr. Adam Simon of the University of Michigan and Drs. Oliver Tschauner and Pamela Burnley, and graduate student Christopher Cline of the University of Nevada Las Vegas (UNLV), whom helped with collection and interpretation of the data. Drs. Paul Chow, Yuming Xiao, and Guoyin Shen of APS-HPCAT, Carnegie Institute of Washington, whom assisted in the beamline setup and collection of data. Dr. John Hanchar of the Department of Earth Sciences,

Memorial University of Newfoundland, whom synthesized the Nb-doped rutile crystals. Dr. Thomas Pettke of the Institute of geological sciences, Bern, Switzerland, whom preformed the laser ablation inductively coupled plasma mass spectroscopy. Dr. Yusheng Zhao of UNLV, whom provided funding from the UNLV high pressure science and engineering center (HiPSEC). This chapter was submitted to American Mineralogist, May 2, 2014 and was accepted provisionally pending revisions.

Chapter 4 discusses rutile solubility in aqueous fluid based on SXRF measurements of Zr in Zr-doped rutile-saturated NaF-, NaCl-, KCl-, bearing aqueous fluids from 0.5-2.79 GPa and 250-650°C. The Zr/Ti ratio of the starting rutile was quantified, and at the pressure-temperature conditions of the experiments, published diffusion data indicate that Zr is effectively immobile ($\log D_{Zr}$ $\sim 10^{25} m^2/s$ at 650°C and $10^{30} m^2/s$ at 250°C; diffusion length scales <0.01 μm in rutile. Hence, the Zr/Ti ratio of the starting rutile does not change during the experiment, and the measured concentration of Zr in the fluid was used to calculate the concentration if Ti (i.e., solubility of rutile) in the fluid. The results indicate that fluid composition, exerts the greatest control on rutile solubility in aqueous fluid, consistent with previous studies, and that increasing temperature has a positive, albeit less pronounced, effect. The measured concentration of Zr in the fluid, and the calculated solubility of rutile, exhibit a positive linear relationship between with the NaF concentration in the fluid. The solubility increases by an order of magnitude from a 2 wt% NaF-bearing aqueous solution to a 4 wt% NaF-bearing aqueous solution. These new data are consistent with observations from field studies of exhumed terranes that indicate that rutile is soluble in complex aqueous fluids, and that fluid composition is the dominant control on rutile solubility and HFSE mobility.

This chapter was co-authored by Drs. Adam Simon and Youxue Zhang of the University of Michigan and Dr. Oliver Tschauner of the University of Nevada Las Vegas (UNLV), whom helped with interpretation of the data. Drs. Paul Chow,

Yuming Xiao, and Guoyin Shen of APS-HPCAT, Carnegie Institute of Washington, whom assisted in the beamline setup and collection of data. Dr. John Hanchar of the Department of Earth Sciences, Memorial University of Newfoundland, synthesized the Zr-doped rutile crystals. Drs. Yusheng Zhao and Pamela Burnley of UNLV, whom provided funding from the UNLV high pressure science and engineering center (HiPSEC) and NSF EAR 1264560, respectively. This chapter will be submitted to American Mineralogist, September, 2014.

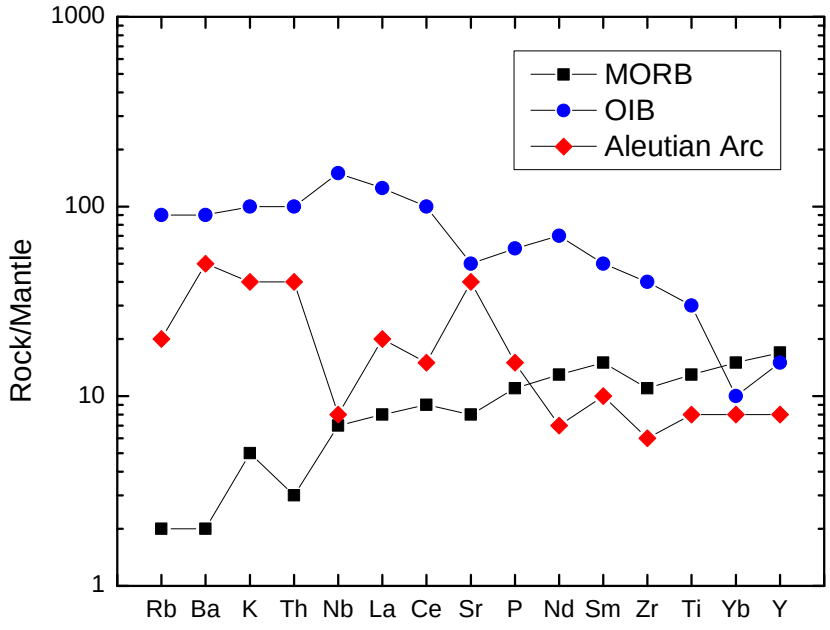

Figure 1.1: Primitive mantle normalized diagram modified from Hawksworth, 1993. This diagram illustrates the distinctive trace element patterns of magmas from selected geologic source regions; MORB and OIB (from Sun and McDonough, 1989) as compared to the Aleutian arc .

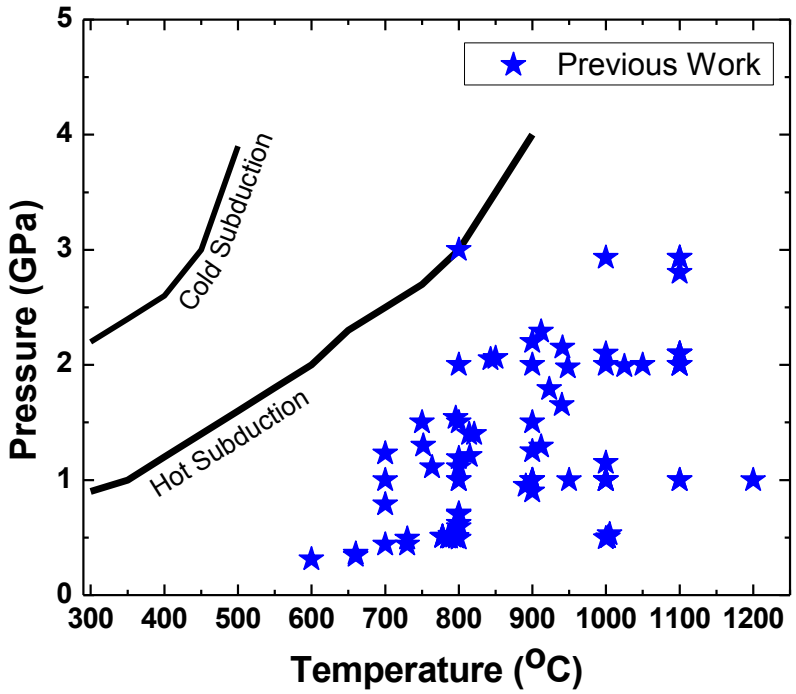

Figure 1.2: Average pressure-temperature pathways for hot and cold subducting slabs, modeled from Hacker, 2008. The starts represent the pressure and temperature conditions for solubility experiments containing rutile and pure water from Ayers and Watson (1991), (1993); Tropper and Manning, (2005); Audetat and Keppler, (2005); Antignano and Manning, (2008), Manning, (2008); Rapp et al., (2010), and Hayden and Manning, (2011).

1.3 References

Aizawa, Y., Tatsumi, Y., and Yamada, H. (1999) Element transport during dehydration of subducting sediments: implications for arc and ocean island magmatism. The Island Arc, 8, 38-46.

Anderson, A.J., Jayanetti, S., Mayanovic, R.A., Bassett, W.A., and Chou, I-M. (2002) X-ray spectroscopic investigations of fluids in the hydrothermal diamond anvil cell: The hydration structure of aqueous La^{3+} up to 300°C and 1600 bars. American Mineralogist, 87, 262-268.

Antignano, A., and Manning, C.E. (2008) Rutile solubility in H_2O, H_2O-SiO_2, and H_2O-$NaAlSi_3O_8$ fluids at 0.7-2.0 GPa and 700-1000°C: Implications for mobility of nominally insoluble element. Chemical Geology, 255, 283-293.

Audétat, A., and Keppler, H. (2005) Solubility of rutile in subduction zone fluids, as determined by experiments in the hydrothermal diamond anvil cell. Earth and Planetary Science Letters, 232, 393-402.

Ayers, J.C. and Watson, E.B., (1991) Solubility of apatite, monazite, zircon, and rutile in supercritical aqueous fluids with implications for subduction zone geochemistry. Philosophical Transactions of the Royal Society of London. A 335, 365375.

Ayers, J.C., Brenan, J.B., Watson, E.B., Wark, D.A., and Minarik, W.G. (1992) A new capsule technique for hydrothermal experiments using the piston-cylinder apparatus. American Mineralogist, 77, 1080-1086.

Ayers, J.C., and Watson, E.B. (1993) Rutile solubility and mobility in supercritical aqueous fluids. Contributions to Mineralogy and Petrology, 114, 321-330.

Ayers, J.C. (1998) Trace element modeling of aqueous fluid - peridotite interaction in the mantle wedge of subduction zones. Contributions to Mineralogy and Petrology, 132, 390-404.

Baker, M.B. and Stolper, E.M. (1994) Determining the composition of high-pressure mantle melts using diamond aggregates. Geochimica et Cosmochimica Acta, 58, 2811-2827.

Barnicoat, A.C., and Cartwright, I. (1997) The gabbro-eclogite transformation: an oxygen isotope and petrographic study of west Alpine ophiolites. Journal of Metamorphic Geology, 15, 93-104.

Bassett, W.A., Shen, A.H., Bucknum, M., and Chou, I.-M. (1993) A new diamond anvil cell for hydrothermal studies to 2.5 GPa and from 190 to 1200°C. Reviews

of Scientific Instruments, 64, 2340-2345.

Bassett, W.A., Anderson, A.J., Mayanovic, R.A., Chou, I-M. (2000) Hydrothermal diamond anvil cell for XFAS studies of first-row transition elements in aqueous solutions up to supercritical conditions. Chemical Geology, 167, 3-10.

Bassett, W.A. (2003) High pressure-temperature aqueous systems in the hydrothermal diamond anvil cell (HDAC). European Journal of Minerlogy, 15, 773-780.

Bebout, G.E., and Barton, M.D. (1989) Fluid flow and metasomatism in a subduction zone hydrothermal system: Catalina Schist terrane, California. Geology, 17, 976-981.

Bebout, G.E., Ryan, J.G., Leeman, W.P., and Bebout, A.E. (1999) Fractionation of trace elements by subduction zone metamorphism- effect of convergent- margin thermal evolution. Earth and Planetary Science Letters, 171, 63-81.

Beinlich, A., Klemd, R., John, T., Gao, J. (2010) Trace-element mobilization during Ca-metasomatism along a major fluid conduit: Eclogization of blueschist as a consequence of fluid-rock interaction. Geochimica et Cosmochimica Acta, 74, 1892-1922.

Borchert, M., Wilke, M., Schmidt, C., and Rickers, K. (2009) Partitioning and equilibration of Rb and Sr between silicate melts and aqueous fluids. Chemical Geology, 259, 39-47.

Borchert, M., Wilke, M., Schmidt, C., Cauzid, J., and Toculou, R. (2010) Partitioning of Ba, La, Yb and Y between haplogranitic melts and aqueous solutions: An experimental study. Chemical Geology, 276, 225-240.

Breeding, C.M., Ague, J.J., and Bröker, M. (2004) Fluidmetasedimentary rock interactions in subduction-zone mélange: Implications for the chemical composition of arc magmas. Geology, 32,1041-1044.

Brenan, J.M., Shaw, H.F., Phinney, D.L., and Ryerson, F.J. (1994) Rutile-aqueous fluid partitioning of Nb, Ta, Hf, Zr, U and Th: implications for high field strength element depletions in island-arc basalts. Earth ad Planetary Science Letters, 128, 327-339.

Brenan, J.M., Shaw, H.F., Ryerson, F.J. Phinney, D.L. (1995) Mineral-aqueous fluid partitioning of trace elements at 900°C and 2.0 GPa: Constraints on the trace element chemistry of mantle and deep crustal fluids. Geochimica et Cosmochimica Acta, 59, 3331-3350.

Brenan, J.M., Ryerson, J.F., and Shaw, H.F. (1998) The role of aqueous fluids in

the slab-to-mantle transfer of boron, beryllium, and lithium during subduction: Experiments and models. Geochimica et Cosmochimica Acta, 62, 3337-3347.

Brophy, J.G., and Marsh, B.D. (1986) On the Origin of High-Alumina Arc Basalt and the Mechanics of Melt Extraction. Journal of Petrology, 27, 763-789.

Bureau, H., Ménez, B., Khodja, H., Daudin, L., Gallien, J-P., Massare, D., Shaw, C., Métrich, N. (2003) The partitioning of barium and lead between silicate melts and aqueous fluids at high pressures and temperatures. Nuclear Instruments and Methods in Physics Research B, 210, 434-440.

Bureau, H., Ménez, B., Malavergnes, V., Somogyi, A., Simionovici, A., Massare, D., Khodja, H., Daudin, L., Gallien, J-P., Shaw, C., Bonnin-Mosbah, M. (2007) In situ mapping of high-pressure fluids using hydrothermal diamond anvil cells. High Pressure Research, 27, 235-247.

Chou, I-M., Bassett, W.A., Anderson, A.J., Mayanovic, R.A., and Shang, L. (2008) Containment of fluid samples in the hydrothermal diamond-anvil cell without the use of metal gaskets: Performance and advantages for in situ analysis. Review of Scientific Instruments, 79, 115103.

Frezzotti, M.L., Ferrando, S., Tecce, F., Castelli, D. (2012) Water content and nature of solutes in shallow-mantle fluids from fluid inclusions. Earth and Planetary Science Letters, 351-352, 70-83.

Foley, S.F., Jackson, S.E., Fryer, B.J., Greenouch, J.D., and Jenner, G.A. (1996) Trace element partition coefficients for clinopyroxene and phlogopite in an alkaline lamprophyre from Newfoundland by LAM-ICP-MS. Geochimica et Cosmochimica Acta, 64, 629-638.

Foley, S.F., Barth, M.G., and Jenner, G.A. (2000) Rutile/melt partition coefficients for trace elements and an assessment of the influence of rutile on the trace element characteristics of subduction zone magmas. Geochimica et Cosmochimica Acta, 64, 933-938.

Gao, J., John, T., Klemd, R., and Xiong, X. (2007) Mobilization of Ti-Nb-Ta during subduction: Evidence from rutile-bearing dehydration segregations and veins hosted in eclogite, Tianshan, NW China. Geochimica et Cosmochimica Acta, 71, 4974-4996.

Giaramita, M.J., and Sorensen, S.S. (1994) Primary fluids in low-temperature eclogites: evidence from two subduction complexes(DominicanRepublic,and California, USA). Contributions to Mineralogy and Petrology, 117, 279-292.

Green T.H. (1981) Experimental evidence for the role of accessory phases in magma

genesis. Journal of Volcanology and Geothermal Research, 10, 405-422.

Green T.H. and Pearson, N.J. (1987) An experimental study of Nb and Ta partitioning between Ti-rich minerals and silicate liquids an high pressure and temperature. Geochimica et Cosmochimica Acta, 51, 55-62.

Green T.H. and Adam, J. (2003) Experimentally-determined trace element characteristics of aqueous fluid from partially dehydrated mafic oceanic crust at 3.0 GPa, 650-700°C. European Journal of Moneralogy, 15, 815-830.

Hacker, B.R. (2008) H_2O subduction beyond arcs. Geochemistry Geophysics Geosystems, 9, 1-24.

Hawksworth, C.J., Gallagher, K., Hergt, J.M., and McDermott, F. (1993a) Mantle and slab contributions in arc magmas. Annual Review of Earth and Planetary Sciences, 21, 175-204.

Hawkesworth, C.J. (1993b) Trace Element Fractionation Processes in the Generation of Island Arc Basalts. Philosophical Transactions of the Royal Society of London, Series A, 342, 179-191.

Hayden, L.A., and Manning, C.E. (2011) Rutile solubility in supercritical $NaAlSi_3O_8$-H_2O fluids. Chemical Geology, 284, 74-81.

Hermann, J., Spandler, C., Hack, A., and Korsakov, A.V. (2006) Aqueous fluids and hydrous melts in high-pressure and ultra high pressure rocks: Implications for element transfer in subduction zones. Lithos, 92, 399-417.

Hermann, J., Zheng, Y-F., and Rubatto, D. (2013) Deep fluids in subducted continental crust. Elements, 9, 281-287.

John, T., Klemd, R., Gao, J., and Garbe-Schönberg (2008) Trace-element mobilization in slabs due to non steady-state fluid-rock interaction: Constraints from and eclogite-faces transport vein in blueschists (Tianshan, China). Lithos, 103, 1-24.

Johnson, K.T.M. (1998) Experimental determination of partition coefficients for rare earth and high-field-strength elements between clinopyroxene, garnet, and basaltic melt at high pressures. Contributions to Mineralogy and Petrology, 133, 60-68.

Kalfoun, F., Ionov, D., and Merlet, C. (2002) HFSE residence and Nb/Ta ratios in metasomatised, rutile-bearing mantle peridotites. Earth and Planetary Science Letters, 199, 49-65.

Kawamoto, T., Kanzaki, M., Mibe, K., Matsukage, K.N., and Ono, S. (2013) Separation of supercritical slab-fluids to form aqueous fluid and melt components in

subduction zone magamatism. Proceedings of the National Academy of Sciences, 109, 18695-18700.

Kay, R.W. (1984) Elemental abundances relevant to identification of magma sources. Philosophical Transactions of the Royal Society of London, Series A, 310, 535-547.

Kelemen, P.B., Johnson, K.T.M., Kinzler, R.J., and Irving, A.J. (1990) High-field-strength element depletions in arc basalts due to mantlemagma interaction. Nature, 345, 521-524.

Keppler, H. (1996) Constraints from partitioning experiments on the composition of subduction zone fluids. Nature, 380, 237-240.

Kessel, R., Schmidt, M.W., Ulmer, P., and Pettke, T. (2005) Trace element signature of subduction-zone fluids, melts and supercritical liquids at 120-180 km depth. Nature 437, 724-727.

Kodolányi, J., and Pettke, T. (2011) Loss of trace elements from serpentinites during fluid-assisted transformation of chrysotile to antigorite -An example from Guatemala. Chemical Geology, 284, 351-362.

Louvel, M., Sanchez-Valle, C., Malfait, W.J., Testemale, D., and Hazemann, J-L. (2013) Zr Complexation in high pressure fluids and silicate melts and implications for mobilization of HFSE in subduction zones. Geochimica et Cosmochimica Acta, 104, 281-299.

Louvel, M., Sanchez-Valle, C., Malfait, W.J., Cardon, H., Testemale, D., and Hazemann, J-L. (2014) Constraints on the mobilization of Zr in magmatic-hydrothermal processes in subduction zones from in situ fluid-melt partitioning experiments. American Mineralogist, 99, 1616-1625.

Manning, C.E., Wilke, M., Schmidt, C., and Cauzid, J. (2008) Rutile solubility in albite-H_2O and $Na_2Si_3O_7$-H_2O at high temperatures and pressures by in-situ synchrotron radiation micro-XRF. Earth and Planetary Science Letters, 272, 730-737.

Manning, C.E. (1996) Effect of sediment on aqueous silica transport in subduction zones. Subduction: Top to Bottom, American Geophysical Union Monograph, 96, 277-284.

Manning, C. E. (1998) Fluid composition at the blueschist-eclogite transition in the model system Na_2O-MgO-Al_2O_3-SiO_2-H_2O-HCl. Swiss Bulletin of Mineralogy and Petrology, 78, 225-242.

Manning, C.E. (2004) The chemistry of subduction-zone fluids. Earth and Planetary Science Letters, 223, 1-16.

Manning, C.E., Wilke, M., Schmidt, C., and Cauzid, J. (2008) Rutile solubility in albite-H_2O and $Na_2Si_3O_7$-H_2O at high temperatures and pressures by in-situ synchrotron radiation micro-XRF. Earth and Planetary Science Letters, 272, 730-737.

Marshak, S. (2004) Essentials of Geology, W.W. Norton Company, Inc.

McCulloch, M.T., and Gamble, J.A. (1991) Geochemical and geodynamical constraints on subduction zone magmatism. Earth and Planetary Science Letters, 102, 358-374.

Melzer, S., and Wunder, B. (2000) Island-arc basalt alkali ratios: Constraints from phengite-fluid partitioning experiments. Geology, 28, 583-586.

Morris, J.D., Leeman, W.P., and Tera, F. (1990) The subducted component in island arc lavas: Constraints from Be isotopes and B-Be systematics. Nature, 344, 31-36.

Najorka, J., Gottschalk, M., Franz, G., and Heinrich, W. (1999) Ca-Sr distribution among amphibole, clinopyroxene, and chloride-bearing solutions American Mineralogist, 84, 596-606.

Peacock, S.M. (1993) The importance of blueschist $\rightarrow$ eclogite dehydration reactions in subducting oceanic crust. Geological Society of America Bulletin, 105, 684-694.

Pearce, J.A., and Peate, D.W. (1995) Tectonic implications of the composition of volcanic arc magmas. Annual Review of Earth and Planetary Sciences, 23, 251-285.

Perfit, M.R., Gust, D.A., Bence, A.R., Arculus, R.J., and Taylor, S.R. (1980) Chemical characteristics of island arc basalt: implications for mantle sources. Chemical Geology, 30, 227-256.

Philippot, P., Agrinier, P., and Scambelluri, M. (1998) Chlorine cycling during subduction of altered oceanic crust. Earth and Planetary Science Letters, 161, 33-44.

Plank, T., Cooper, L.B., and Manning, C.E. (2009) Emerging geothemometers for estimating slab surface temperatures. Nature Geoscience, 2, 611-615.

Poli, S., and Schmidt, M.W. (2002) Petrology of sub ducted slabs. Annual Review of Earth and Planetary Sciences, 30, 207-235.

Rapp, J.R., Klemme, S., Butler, I.B., and Harley, S.L. (2010) Extremely high solubility of rutile in chloride and fluoride-bearing metamorphic fluids: An experimental investigation. Geology, 38, 323.

Rudnick, R.L., Barth, M., Horn, I., McDonough, W.F. (2000) Rutile-Bearing Refrac-

tory Eclogites: Missing Link Between Continents and Depleted Mantle Science, 287, 278-281.

Ryerson, F.J., and Watson, E.B. (1987) Rutile saturation in magmas: implications for Ti Nb Ta depletion in island-arc basalts. Earth and Planetary Science Letters, 86, 225-239.

Sanchez-Valle, C., Martinez, I., Daniel, I., Philippot, P., Bohic, S., and Simionovici, A. (2003) Dissolution of strontianite at high P-T conditions: An in situ synchrotron X-ray fluorescence study. American Mineralogist, 88, 978985.

Sanchez-Valle, C., Saniel, I., Martinez, I., Simionovici, A., and Reynard, B. (2004) Progress in quantitative elemental analyses in high P T fluids using synchrotron x-ray fluorescence (SXRF). Journal or Physics: Condensed Matter, 16, S1197-S1206.

Sanchez-Valle, C. (2013) Structure and Thermodynamics of Subduction Zone Fluids from Spectroscopic Studies. Reviews in Mineralogy and Geochemistry, 76, 265-309.

Saunders A.D., Tarney J., and Weaver S.D. (1980) Transverse geochemical variations across the Antarctic Peninsula: implications for the genesis of calc-alkaline magmas. Earth and Planetary Science Letters, 46, 344360.

Scambelluri, M., and Philppot, P. (2001) Deep fluids in subduction zones. Lithos, 55, 213-227.

Schmidt, M.W. and Poli, S. (1998) Experimentally based water budgets for dehydrating slabs and consequences for arc magma generations. Earth and Planetary Science Letters, 163, 361-379.

Schmidt, C. and Rickers, K. (2003) In-situ determination of mineral solubilities in fluids using a hydrothermal diamond-anvil cell and SR-XRF: Solubility of AgCl in water. American Mineralogist, 88, 288-292.

Schmidt, C., Rickers, K., Wirth, R., Nasdala, L., and Hanchar, J. (2006) Low-temperature Zr mobility: An in situ synchrotron-radiation XRF study of the effect of radiation damage in zircon on the element release in H_2O + HCl $\pm$ SiO_2 fluids. American Mineralogist, 91, 1211.

Schmidt, C., Rickers, K., Bilderback, D.H., and Huang, R. (2007) In situ synchrotron radiation XRF study of REE phosphate dissolution in aqueous fluids to 800°C. Lithos, 95, 87-102.

Schmidt, A., Weyer, S., John, T., and Brey, G.P. (2009) HFSE systematics of rutile-

bearing eclogites: New insights into subduction zone processes and implicationsfor the earths HFSE budget Geochimica et Cosmochimica Acta, 73, 455-468.

Schmidt, C., Wilke, M., Appel, K., Borchert, M., and Vincze, L. (2010) Solubility of zircon in H_2O-$Na_2Si_3O_7$ solutions determined using a confocal setup for micro-XRF experiments with diamond-anvil cells. Abstract ???

Sharp, Z.D., and Barnes, J.D. (2004) Water-soluble chlorides in massive seafloor serpentinites: a source of chloride in subduction zones. Earth and Planetary Science Letters, 226, 243-254.

Shen, A.H. and Keppler, H. (1997) Direct observation of complete miscibility on albite-H_2O system. Letters to Nature, 385, 710-712.

Shervais, J.W. and Jean, M.M. (2012) Inside the subduction factory: Modeling fluid mobile element enrichment in the mantle wedge above a subduction zone. Geochimica et Cosmochimica Acta, 95, 270-285.

Smith Jr., R.L. and Fang, Z. (2009) Techniques, applications and future prospects of diamond anvil cells for studying supercritical water systems. Journal of Supercritical Fluids, 47, 431-446.

Spandler, C., Hermann, J., Arculus, R., and Mavrogenes, J. (2003) Redistribution of trace elements during prograde metamorphism from lawsonite blueschist to eclogite facies; implications for deep subduction-zone processes. Contributions to Mineralogy and Petrology, 146, 205-222.

Spandler, C., Hermann, J., Arculus, R., and Mavrogenes, J. (2004) Geochemical heterogeneity and element mobility in deeply subducted oceanic crust; insights from high-pressure mafic rocks from New Caledonia. Chemical Geology, 206, 21-42.

Spandler, C., and Hermann, J. (2006) High-pressure veins in eclogite from New Caledonia and their significance for fluid migration in subduction zones. Lithos, 89, 135-153.

Spandler, C., Pettke, T., and Hermann, J. (2009) The composition of serpentinite dehydration fluids in subduction zones: an experimental study. Geochimica et Cosmochimica Acta, 73, Supplement 1, A1256.

Spandler, C., Pettke, T., and Rubatto, D. (2011) Internal and External Fluid Sources for Eclogite-facies Veins in the Monviso Meta-ophiolite, Western Alps: Implications for Fluid Flow in Subduction Zones. Journal of Petrology 52, 1207-1236.

Stalder, R., Foley, S.F., Brey, G.P., and Horn, I. (1998) Mineral-aqueous fluid parti-

tioning of trace elements at 900-1200°C and 3.0-5.7 GPa: New experimental data for garnet, clinopyroxene, and rutile, and implications for mantle metasomatism. Geochimica et Cosmochimica Acta, 62, 1781-1801.

Stechern, A., Wilke, M., Schmidt, C., Rickers, K., Pascarelli, S., and Manning, C.E. (2009) XAFS measurements on Zr in aqueous fluids at high pressures and temperatures using a modified hydrothermal diamond-anvil cell. Journal of Physics: Conference Series, 190, 012058.

Stern, R.J. (2002) Subduction Zones. Reviews of Geophysics, 40, 1-42.

Sun, S.-s., and McDonough, W.F. (1989) Chemical and isotopic systematics of oceanic basalts: implications for mantle composition and processes. Geological Society, London, Special Publications, 42, 313-345.

Svensen, H., Jamtveit, B., Yardley, B.W., Engvik, A.K., Aus- trheim, H., Broman, C. (1999) Lead and Bromine enrichment in eclogite facies fluids: extreme fractionation during lower crustal hydration. Geology 27, 467-470.

Tanis, E.A., Simon, A.C., Tschauner, O. Chow, P., Xiao, Y. Shen, G., Hanchar, J.M., and Frank, M. (2012) Solubility of xenotime in a 2 *M* HCl aqueous fluid from 1.2 to 2.6 GPa and 300 to 500°C. American Mineralogist, 97, 17081713.

Tropper, P., and Manning, C.E. (2005) Very low solubility of rutile in H_2O at high pressure and temperature, and its implications for Ti mobility in subduction zones. American Mineralogist, 90, 502-505.

Tropper, P., Manning, C.E., and Harlov, D.E. (2011) Solubility of $CePO_4$ monazite and YPO_4 xenotime in H_2O and H_2ONaCl at 800°C and 1 GPa: Implications for REE and Y transport during high-grade metamorphism. Chemical Geology, 282, 58-66.

Tropper, P., Manning, C.E., and Harlov, D.E. (2013) Experimental determination of $CePO_4$ and YPO_4 solubilities in H_2O-NaF at 800°C and 1 GPa: implications for rare earth element transport in high-grade metamorphic fluids. Geofluids, 13, 372-380.

Van Hinsberg, V.J., Migdisov, A.A., and Williams-Jones, A.E. (2010) Reading the mineral record of fluid composition from element partitioning. Geology, 38, 847-850.

Wilke, M., Schmidt, C., Dubrail, J., Appel, K., Borchert, M., Kvashnina, K., and Manning, C.E. (2012) Zircon solubility and zirconium complexation in H_2O+Na_2O +$SiO_2Al_2O_3$ fluids at high pressure and temperature. Earth and Planetary Science Letters, 349-350, 15-25.

Woodhead, J., Eggins, S., and Gamble, J. (1993) High field strength and transition element systematics in island arc and back-arc basin basalts: evidences for multi-phase melt extraction and a depleted mantle wedge. Earth and Planetary Science Letters, 114, 491-504.

Wu, J. and Konga, K.T. (2013) Fluorine partitioning between hydrous minerals and aqueous fluid at 1 GPa and 770-947°C: A new constraint on slab flux. Geochimica et Cosmochimica Acta, 119, 77-92.

Zack, T., Foley, S.F., and Rivers, T. (2002a) Equilibrium and disequilibrium trace element partitioning in hydrous eclogites (Trescolmen, Central Alps). Journal of Petrology 43, 19471974.

Zack, T., Kronz, A., Foley, S.F., and Rivers, T. (2002b) Trace element abundances in rutiles from eclogites and associated garnet mica schists. Chemical Geology 184, 97122.

Zack, T. and John, T. (2007) An evaluation of reactive fluid flow and trace element mobility in subducting slabs. Chemical Geology, 239, 199-216.

CHAPTER 2

Solubility of xenotime in a 2 *M* HCl aqueous fluid from 1.2 to 2.6 GPa and 300 to 500°C

2.1 Abstract

Constraining mass transfer of the rare earth elements (REE) and high-field strength elements (HFSE) from subducted oceanic crust and metasediments to the mantle wedge is fundamental towards interpreting processes that affect trace element mobility in subduction zone environments. Experimental studies of the partitioning of trace elements involving aqueous fluids at P-T conditions appropriate for slab-mantle wedge conditions are complicated by the difficulties in retrieving the fluid. Here we present the results from an application of an in situ technique that permits quantitative determination of element concentrations in aqueous fluid at geologically relevant supercritical conditions. We focus on pressures and temperatures appropriate for devolatilization-induced element transfer in subduction zone environments, and conditions obtained during regional metamorphism. In this study, we used a hydrothermal diamond-anvil cell (HDAC) and in situ synchrotron X-ray fluorescence (SXRF) to quantify the concentration of Y, an important trace element often used as a proxy for the heavy REE in geologic systems, in a xenotime-saturated 2 *M* HCl-aqueous fluid at 1.19 to 2.6 GPa and 300-500°C. At these pressures and temperatures

the solubility of yttrium ranges from 2400 to 2850 ppm. We find that the concentration of Y decreases with increasing fluid density. These new data, combined with published data generated from experiments done at lower pressure, in fluids of nearly identical composition and also NaCl-H_2O fluids, constrain the effects of pressure and temperature on the ability of aqueous fluid to scavenge and transport Y, and by analogy the HREE. Although the physical properties of Y are similar to the high field strength elements, Y exhibits geochemical behavior that is analogous to the heavy rare earth elements (HREE).

2.2 Introduction

Arc volcanoes and their plutonic counterparts are the surface and crustal manifestations, respectively, of processes originating with the transfer of aqueous fluids (± melt) from subducted ocean lithosphere and overlying metasediments to the mantle wedge. These fluids induce partial melting of the mantle wedge (e.g., Aizawa et al., 1999) and have been postulated to contribute to the fractionation of trace elements, which in turn may leave an imprint on the trace element composition of the arc volcanic rocks (Kay et al., 1984; Bebout et al., 1999). It has also been proposed that the fluid triggers partial melting of the mantle and that trace element patterns are controlled by the partitioning of elements between the ascending melt and mantle (Kessel et al., 2005). Quantifying the nature of fluid (± melt) transfer at the pressure and temperature conditions appropriate for the subduction zone environment is crucial for evaluating the role of fluids in such opposing models. More generally, quantitative data that constrain the trace element-scavenging ability of aqueous fluid at elevated pressure and temperature will lead to a better understanding of the recycling of elements between ocean lithosphere, metasediments, mantle wedge, and crust. To this end, significant effort has been made to constrain the relative mobility of major, minor, and trace elements in fluid-bearing magmatic and metamorphic systems in order

to understand the origin of variation in absolute element abundances and element ratios.

Most previous studies designed to quantify the partitioning of elements between aqueous fluid and minerals or melt at elevated pressure and temperature have been of the recovery type. Element distribution and concentrations in such experiments were determined by measuring the change in the concentration of a particular element in the starting and final phase assemblages. In the past decade, efforts have been made to develop an in situ technique that permits quantification of element distribution between fluid and minerals. These efforts have focused on the use of an externally heated diamond-anvil cell (DAC) as the pressure vessel. Sanchez-Valle et al. (2003) measured the solubility of strontianite in H_2O by using a DAC to subject the charge to 0.4 to 3.6 GPa and from 25°C to 250°C, respectively. They directly measured the concentration of Sr by using in situ synchrotron x-ray fluorescence (SXRF). Those authors reported that the dissolution of strontianite into the fluid increased as a function of increasing pressure and temperature. Schmidt et al. (2006) investigated the solubility of zircon in H_2O + HCl ± SiO_2 fluids at temperatures between 200 and 500°C and pressures of ∼2 GPa by using a hydrothermal diamond-anvil cell (HDAC) and in situ time-resolved synchrotron-radiation XRF analyses. They reported that the solubility of Zr decreases with increasing temperature. Schmidt et al. (2007) used the HDAC and in situ SXRF to quantify the solubility of monazite in aqueous fluid at 250 to 800°C and a maximum pressure of 2 GPa, and the solubility of xenotime in aqueous fluid at 250 to 600°C and a maximum pressure of 1.32 GPa. Their HDAC configuration was designed with a cylindrical recess in the lower anvil that permitted collection of the element specific fluorescence signal specifically from fluid in the recessed part of the chamber. Manning et al. (2008) measured rutile solubility in $NaAlSi_3O_8$-bearing aqueous fluids at 0.31 to 1.23 GPa and 600 to 800°C. They also used an HDAC configuration that contained one anvil that was modified with

a recess. Manning et al. (2008) reported that the solubility of rutile was strongly positively correlated with the concentration of dissolved $NaAlSi_3O_8$. Manning et al. (2008) reported that the solubility of rutile was strongly positively correlated with the concentration of dissolved $NaAlSi_3O_8$. Stechern et al. (2009) measured the solubility of zircon in aqueous fluid that contained variable concentrations of dissolved HCl and $Na_2Si_2O_5$ from 0.33 to 0.63 GPa and 500 to 750°C; they also used a recessed-anvil HDAC. Their results showed no correlation between the solubility of zircon and the concentrations of HCl and $Na_2Si_2O_5$ in the fluid.

There have been two high-pressure studies on the solubility of yttrium in aqueous fluid. Schmidt et al. (2007) used the SXRF technique with an HDAC. Their study reported data that constrain the solubility of xenotime in a 1.88 *M* HCl aqueous fluid at pressures from 0.0045 to 1.32 GPa and temperatures from 250 to 600°C, respectively. The results indicate that the solubility of yttrium in the fluid increases from 220 to 4231 ppm with increasing pressure and temperature. Tropper et al. (2011) also studied the solubility of xenotime in NaCl-bearing aqueous fluid, at variable NaCl concentrations, at 1 GPa and 800°C by using the recovery technique and a piston-cylinder apparatus to generate pressure. Their results indicate that the concentration of yttrium in NaCl-bearing aqueous fluid increases with increasing NaCl concentration at constant pressure and temperature. Pressure, temperature, and fluid composition all contribute to the structure and density of the fluid and thus, affect the activity and partitioning of yttrium. In this study, we constrained the behavior of Y in aqueous fluid as a function of these parameters to evaluate the hypothesized role that aqueous fluid plays in moderating the mobility of Y and, by analogy, the heavy rare earth elements (HREE) in subduction zone environments.

2.3 Experimental Methods

The synthetic end-member xenotime (YPO_4) crystals used in this study were prepared in the experimental geochemistry laboratory at Memorial University of Newfoundland following the method described in Hanchar et al. (2001). Briefly, high-purity Y_2O_3 and ammonium dihydrogen phosphate ($NH_4H_2PO_4$), obtained from Alfa Aesar, were thoroughly mixed in stoichiometric proportions of 1.5 mol% Y_2O_3; and 3 mol% $NH_4H_2PO_4$, in an HNO_3-cleaned agate mortar and pestle under absolute ethanol and allowed to dry. Once dried, the powders were mixed under absolute ethanol with the fluxing agents Li_2MoO_4 and MoO_3 in the following proportions: 86 mol% MoO_3; 9.5 mol% Li_2MoO_4; and the 4.5 mol% mixture of Y_2O_3 and $NH_4H_2PO_4$ mixture mentioned above and allowed to dry. The mixture was then transferred to a clean platinum crucible with a tightly fitted Pt lid. The crucible was lowered into the "hot spot"of a preheated (1250°C) Deltech $MoSi_2$ vertical tube furnace for seven days, at constant temperature, permitting the flux to evaporate. When xenotime saturation was reached, the xenotime crystals began to grow in the residual flux. Using a type S control thermocouple, the temperature in the hot spot was measured to within ±5°C. Upon completion of the synthesis no residual flux remained in the crucible. The xenotime crystals were simply removed from the Pt crucible with tweezers, and cleaned in concentrated HNO_3.

The SXRF experiments were done at undulator beamlime 16-IDD (HPCAT) at the Advanced Photon Source (APS) synchrotron facility at Argonne National Laboratory. The incident beam energy was 20.1 keV. The beam was focused to 35 μm by 50 μm full width at half maximum (FWHM) by using a pair of Kirkpatrick-Baez mirrors and a 100 μm round pinhole was used just before the HDAC to clean up the tails of the incident beam, which contained a flux of 1.14 x 10^{12} photons/s/mm^2. The incident beam was projected through the diamonds of the HDAC into the sample chamber. The fluorescence from the sample was collected in a 170° backscattering

geometry by using a Vortex-EX silicon drift detector that was positioned ∼0.8 meters from the sample (Figure 2.1, left). To reduce the background, a pair of large collimating slits was placed before the detector, therefore requiring more distance from the sample. The energy channels of the multi-channel analyzer were calibrated with Fe-55, Co-57 and Cd-109 radioactive sources. The position and aperture of the detector was optimized by using a powder Y_2O_3 commercial plasma-grade standard that was centered on the experimental stage.

The HDAC that was used in the current study described in detail by Bassett et al. (1993) was equipped with two opposing 500 μm culet diamonds, and had resistive molybdenum wires coiled around a tungsten carbide seat that supported each diamond anvil. Two K-type (NiCr-NiAl) thermocouples were used to measure temperature, one on each diamond. The HDAC was heated resistively by using variable transformers that facilitated flexible heating rates and allowed us to maintain temperature to ±5°C. The HDAC had been previously calibrated up to 645°C by observing the melting point of CsCl, which was found to be within 5°C of the thermocouple reading. The HDAC has been calibrated up to 800°C by observing the melting point or phase transition of $NaNO_3$, CsCl, and NaCl, and measured temperatures were systematically lower by 0.85% over the entire range studied (Kerrigan, R.J., 2010). A 1% H_2-Ar gas mixture was flowed constantly through the HDAC during the measurements in order to prevent corrosion of the diamonds and the heaters.

A laser-drilled Re gasket was filled with Au, compressed and re-drilled; hence forming a Au liner that acted as an inert barrier to minimize, if not altogether eliminate, chemical interaction between the experimental aqueous fluid and the Re gasket (Figure 2.1, right). The Au served also as an in situ reference material for pressure calibration. X-ray diffraction (XRD) patterns of gold were recorded by using a MAR 165 CCD detector in the forward scattering direction during the experiments. The patterns were integrated and corrected for geometric distortions using Fit2D (Ham-

mersley, 1997). A NIST standard CeO_2 pattern was collected and used to calibration. A synthetic, end-member, single xenotime crystal that measured 15x15x10 μm was loaded into the HDAC, and then 2 M HCl-aqueous fluid was added to the sample chamber by using a micro syringe (Figure 2.1, right). The HDAC was centered on the sample stage and then rotated into a position that prevented any fluorescence from the xenotime crystal from entering the detector.

The HDAC was heated at experimental P to 300°C, and pressure was monitored by collecting XRD patterns of Au throughout the run using the pressure scale by Dorogokupets and Dewaele (2007). Fluorescence spectra were collected iteratively in 300 s intervals. We assessed equilibrium by evaluating the time-dependence of the fluorescence signal. Once the Y peak area, at a unique pressure and temperature condition, became time-invariant it was interpreted to reflect the attainment of steady-state conditions and proximity to chemical equilibrium. This is shown in Figure 2.2. This took approximately 30-40 minutes at each unique P-T point. The time to reach steady-state is consistent with observations reported by Manning et al. (2008), Schmidt et al. (2007), and Sanchez-Valle et al. (2003). After steady state conditions were achieved, spectra were collected in 300 s intervals for $\sim$3 h. The temperature was then increased to 450°C, and subsequently to 500°C, and the data collection procedure was repeated at each temperature. The temperature was then decreased from 500°C to 450°C and subsequently to 300°C following the same data collection protocol. The experimental results are reported in Table 2.1. During heating and cooling, there is some relaxation of the HDAC. This can cause deformation in the gasket sample chamber and result in a slight change in pressure. We observed this change and, therefore, measured pressure before and after each sequence of fluorescence data.

After collecting the experimental spectra, the xenotime and fluid were removed and the gasket was cleaned. The detector response was found to be linear up to 1000

ppm by using two different calibrant solutions (600, 1000 ppm) of Y in the HDAC. Previous SXRF studies reported that a valid fluorescence calibration can be achieved by a multi-point calibration (Sanchez-Valle et al., 2003) as well as a single-point calibration (Manning et al., 2008). Sanchez-Valle et al. (2004) confirmed the validity of the calibration technique as a function of pressure and temperature by analyzing Rb and Sr up to 3.2 GPa and 200°C. They found that there was no characteristic change in the Kα fluorescence peaks. In these experiments a 600 and 1000 ppm Y standard aqueous solutions (prepared from an Alfa Aesar plasma standard) were loaded into the same gasket held in the same HDAC. This was done to ensure that the fluorescence spectra collected from the standards and the experimental fluid originated from the same excitation volume. The spectra for the standard solutions were collected in 300 s intervals for a total time of 3,600 s (Figure 2.3). Note that prior to the experiments, fluorescence spectra of the empty HDAC were collected and Y was not detected. This established a zero concentration for the standard calibration. Self-absorption of Y was assessed by evaluating by the energy of the Y absorption edges and the corresponding photoionization cross section and determined that self absorption is negligible.

The fluorescence spectra from the standard solutions and high P-T experiments were each separately summed, and normalized to transmitted beam flux and time. We monitored beam flux and used this to normalize fluorescence spectra in order to account for beam flux variations. The background and area of the Y fluorescence peak was fit by using Fityk (Wojdr, 2010). The Y peak was sufficiently distinct from the Compton scattering signal arising from diamond, which justified a local linear background fit (Figure 2.4). The background was determined by selecting the minimum point from each side of the Y peak and then subtracting the linear fit between the two points. The background subtracted integrated peak area for the 600 and 1000 ppm Y standards and the zero parts per million Y reference point were used to define a linear calibration curve that was used to calculate Y concentrations in

the experimental fluid (Figure 2.5). The weighted uncertainties for the experimental concentrations were calculated from peak fitting of the experimental data, and by propagating the uncertainty from the standards, which were composed from the uncertainty of the standards peak fit and the calibration curve.

2.4 Results and Discussion

Xenotime solubility in supercritical aqueous fluid is relatively insensitive to changes in pressure and temperature at the experimental conditions in the current study (Figure 2.6 and Table 2.1). However, when plotted with the xenotime solubility data from Schmidt et al. (2007) (Figure 2.6a and 2.6b), conclusions can be drawn about the effect of pressure and temperature. Their data were collected at the same temperatures as those of the current study, but at lower pressures, between 0.01 and 0.29 GPa. The fluid composition in the current study (2 *M* HCl) was nearly identical to that reported by Schmidt et al. (2007; 1.8 *M* HCl). The combined data indicate that the effect of pressure on the solubility of xenotime in aqueous fluid decreases with increasing temperature. At 300°C, the concentration of yttrium in aqueous fluid increases from 500 to ∼2500 ppm as pressure increase from 0.01 to ∼2 GPa, respectively. At 450°C, the concentration of yttrium in aqueous fluid increases from 1760 to ∼2500 ppm as pressure increases from 0.2 to ∼2 GPa, respectively. At 500°C, the concentration of yttrium in aqueous fluid is 2355 ppm at 0.29 GPa and 2575 ppm at 2.3 GPa. There is an ongoing discussion about the liquid/liquid structure transition in water around 1 GPa because the density of water changes non-linearly (Kawamoto et al., 2004; Strassle et al., 2006). Changes in the first coordination shell of water may occur in the fluid state and affect the solubility of xenotime and the way Y is coordinated by Cl^- and water molecules at pressures above 1 GPa. Therefore, it is interesting to look at the evolution of xenotime solubility as a function of density of water. In this study, the density of water was calculated from the equation of state of

Abramson and Brown (2004). The log density of water versus log molality YPO_4 plot (Figure 2.6c) reveals that, as density increases, the solubility of xenotime in the fluid decreases. This observation for the solubility of xenotime is opposite that of trends reported and discussed in Dolejs and Manning (2010) for minerals such as apatite, rutile, quartz, corundum, calcite, fluorite, and portlandite, which display an increase in their solubility in aqueous fluid with increasing temperature and fluid density. We hypothesize that the changes in density and the structure of water at the pressure and temperature conditions of the current study may affect the affinity of Y and Cl^- to coordinate with one another in the fluid. This will be investigated in a future study.

The xenotime solubility data from the current study are plotted in Figure 2.7 as a function of the total chloride concentration in the fluid. Also plotted are data from Schmidt et al. (2007) and data from Tropper et al. (2011). Whereas in the present study and the study of Schmidt et al. (2007), Cl was added as HCl, Tropper et al. (2011) added Cl as NaCl. In comparison, these data place first order constraints on the role of HCl vs. NaCl to dissolve xenotime. The data indicate that HCl, relative to NaCl, has a greater influence on the solubility of xenotime. For example, at 1.19 GPa and 300°C, an aqueous fluid that contains ∼8 wt% Cl in the form of HCl can dissolve 2700 ppm yttrium. Whereas, Tropper et al. (2011) reported that at 1 GPa and 800°C, an aqueous fluid requires ∼16 wt% Cl in the form of NaCl to dissolve ∼2700 ppm yttrium. This observation suggests that fluid composition, in addition to the role of fluid density, as discussed above, plays a critical role in dissolving xenotime. If the following two reactions describe dissolution of xenotime in HCl and NaCl bearing fluid, then the available data indicate that the equilibrium constant for reaction 2.1 is much greater than for reaction 2.2 in accordance with expectations from aqueous chemistry at ambient conditions.

$$YPO_{4(s)} + 3HCl_{(aq)} \rightarrow YCl_{3(aq)} + H_3PO_{4(aq)} \quad (2.1)$$

$$YPO_{4(s)} + 3NaCl_{(aq)} \rightarrow YCl_{3(aq)} + Na_3PO_{4(aq/s)} \quad (2.2)$$

In the absence of an extensive data set for the partitioning of trace elements at the pressure and temperature where aqueous fluids evolve from the subducted slab into the mantle wedge, the data presented in this study can be used to illustrate the potential role of aqueous fluid at moderating trace element ratios in natural systems. If we take the results published by Sanchez-Valle et al. (2003) for the solubility of strontianite ($SrCO_3$) in aqueous fluid from 0.4 to 3.6 GPa and 25 to 250°C as representative for the combined pressure and temperature effects on the solubility of the light ion lithophile elements (LILE) in aqueous fluids, and consider Y as a representative of the HREE, the combined data suggest that the pressure effect on the ability for aqueous fluid to scavenge the LILE is much greater than HREE. For instance, Sanchez-Valle et al. (2003) reported a solubility of Sr of ∼15,500 ppm (1.55 wt%) in pure H_2O at 3.6 GPa and 252°C. The solubility of yttrium at similar conditions (2.6 GPa, 310°C) measured in the current study in 2 M HCl aqueous fluid is ∼2400 ppm (0.24 wt%). While strontianite is not the LILE bearing phase in subduction zone settings, the experimental data yield a model Sr/Y mass ratio of ∼6.

As discussed above, fluid chemistry plays a major role in controlling the solubility of xenotime, and likely strontianite, in aqueous fluid. Therefore, considering the strong effect of HCl on the solubility of xenotime, the solubility of Sr is expected to increase in acidic solutions. Thus the model Sr/Y ratio most likely underestimates Sr/Y ratios in natural fluids. Nonetheless, the combined data suggest that the release

of aqueous fluid from slab material may efficiently fractionate LILE from HREE, which is consistent with observations of the LILE/HREE ratios in arc magmas where aqueous fluid has been postulated to play a role in stimulating melting of the sub-arc mantle.

Table 2.1: Xenotime solubility experimental conditions

Run	1	2	3	4	5
Temperature (°C)	310(±2.6)	450(±3.8)	500(±4.3)	430(±3.6)	300(±2.5)
Pressure (GPa)	2.6(±0.1)	2.17(±0.1)	2.33(±0.2)	1.86(±0.15)	1.19(±0.15)
Cum. Run Duration (min)	0-300	300-600	600-900	900-1060	1060-1420
Conc. of Y in Fluid (ppm)	2400(±215)	2450(±222)	2575(±231)	2850(±258)	2700(244))
HCl (M)	2	2	2	2	2

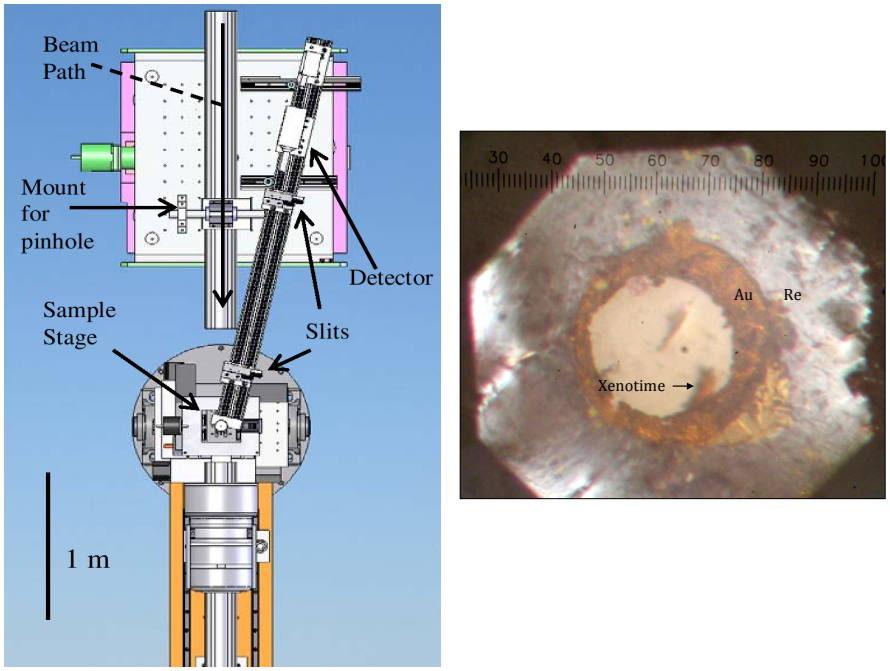

Figure 2.1: The SXRF experimental setup. (Left) The experimental setup at 16 ID-D features a 170° back scatter orientation. The location of the detector, slits, sample stage and the X-ray beam path are noted in the figure. A CCD X-ray detector is mounted behind the sample stage. (Right) The Au lined Re gasket.

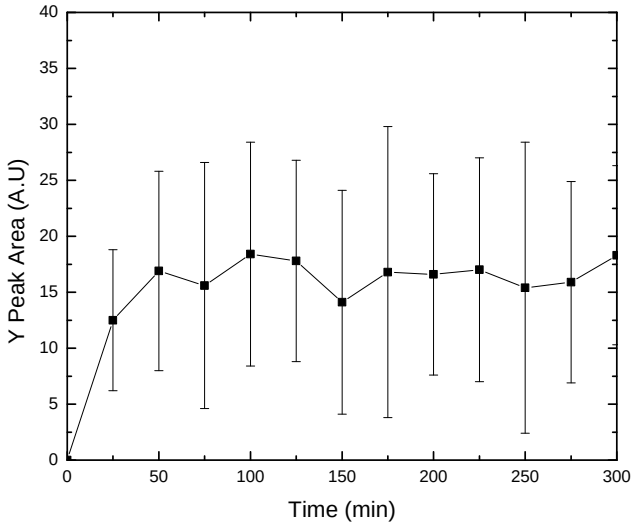

Figure 2.2: The integrated yttrium peak area as a function of time. The integrated peak area from the sum of 30 min intervals at 300°C plotted as a function of time. Once the Y peak area, at a unique pressure and temperature condition, became time-invariant it was interpreted to reflect the attainment of steady-state conditions and proximity to chemical equilibrium. The error bars are determined by propagating the uncertainties in the fitting procedure to the integrated peak area.

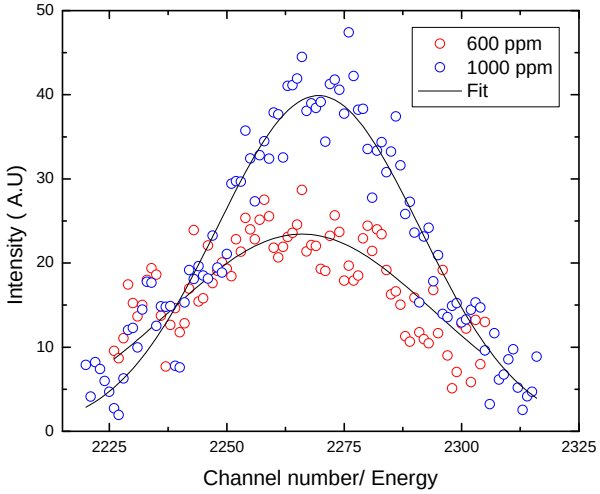

Figure 2.3: The summed XRF spectra of the Y standard solutions. The squares represent 1000 ppm Y and the circles represent 600 ppm Y. The solid lines represent the fit of the curves.

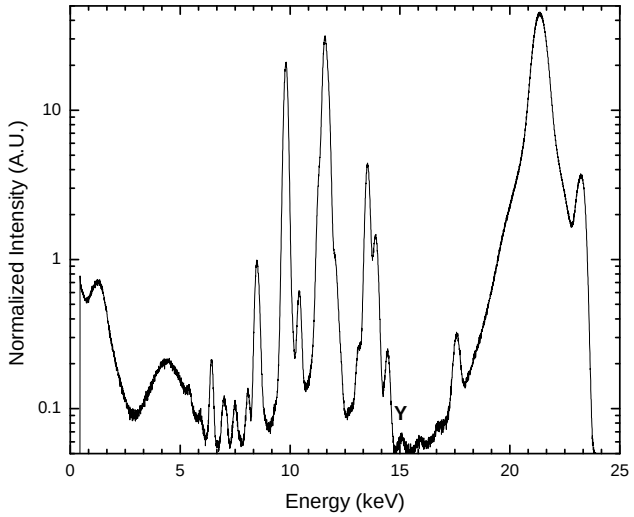

Figure 2.4: The summed and normalized XRF spectra of the 1000 ppm Y standard solution. The Y peak was sufficiently distinct from the Compton scattering signal arising from diamond, which justified a local linear background fit.

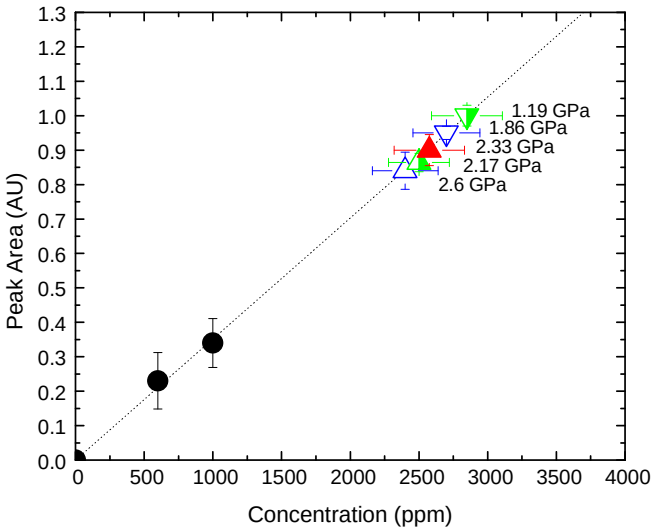

Figure 2.5: The HP-HT data plotted along the calibration curve. The integrated peak area of the Y standard solutions (black dots) demonstrate a linear relationship (dotted line) between concentration and peak area. The upward pointing triangles represent data that were collected as temperature was increased from ambient to run conditions. The downward pointing triangles represent data that were collected after temperature was decreased. See text for details. The open symbols represent 300°C, half-filled triangles represent 450/430°C, and the solid triangle represents 500°C.

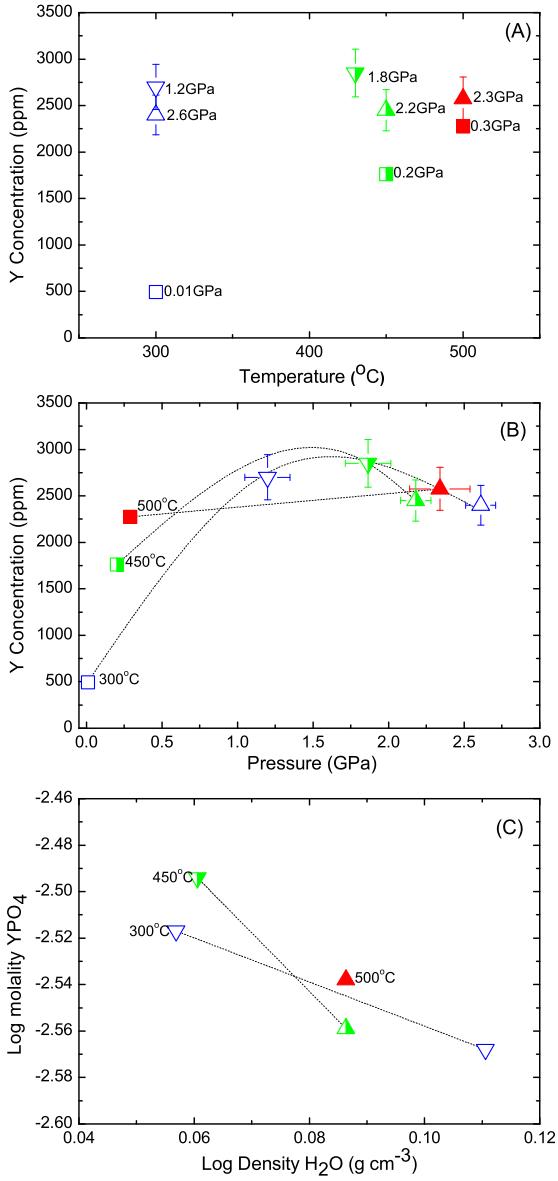

Figure 2.6: The SXRF experimental data for xenotime solubility in 2 *M* HCl aqueous fluid quantified as a function of temperature (a), pressure (b), and density (c). These data from the current study (triangles) are combined with the xenotime solubility data of Schmidt et al. (2007) (squares) in figures a and b. The upward pointing triangles represent data collected as temperature was increased from ambient to run conditions. The downward triangles represent data that were collected as temperature was decreased. The open symbols represent 300°C, half filled are 450/430°C, and solid are 500°C. The dashed lines are to guide the eye between the isotherms. The combined data indicate that the effect of temperature on the solubility of xenotime in aqueous fluid decreases with increasing pressure and temperature.

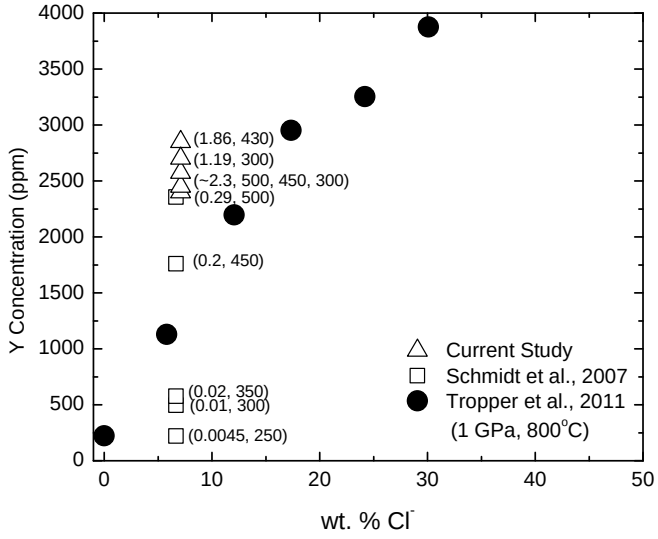

Figure 2.7: The experimental data for xenotime solubility in aqueous fluid plotted as a function of Cl concentration of the fluid. The Schmidt et al. 2007 study (squares) covers a P-T range of 0.04 -1.3 GPa and 250-600°C and the Cl is added in the form of HCl. In the Tropper et al. 2011 study (circles) the Cl is added in the form of NaCl and all experiments are at 1GPa and 800°C. The current study (triangles) covers a P-T range of 1.19-2.6GPa and 300-500°C.

2.5 Acknowledgements

This study was partially sponsored by the National Nuclear Security Administration under the Stewardship Science Academic Alliances program through DOE Cooperative Agreement No. DE-FC52-06NA27684. HPCAT Sector 16 of the Advanced Photon Source at Argonne National Laboratory is supported by DOE-BES, DOE-NNSA, DOD-TACOM, and the W.M. Keck Foundation. We acknowledge COMPRESS and GSECARS for the use of the laser drilling system. The Advanced Photon Source is supported by the U.S. Department of Energy, Office of Science, Office of Basic Science, under Contract No. DE-AC02-06CH11357. JMH thanks the Canadian Natural Sciences and Research Council for partial support for this research in

the form of a Discovery Grant, and Memorial University of Newfoundland, for additional financial support for this project. We thank Craig Manning and an anonymous reviewer for detailed constructive comments that helped significantly to improve the manuscript.

2.6 References

Abramson, E.H., and Brown, J.M. (2004) Equation of state of water based on speeds of sound measured in the diamond-anvil cell. Geochimica et Cosmochimica Acta. 68, 1827-1835.

Aizawa, Y., Tatsumi, Y., and Yamada, H. (1999) Element transport during dehydration of subducting sediments: implications for arc and ocean island magmatism. The Island Arc, 8, 38-46.

Bassett, W.A., Shen, A.H., Bucknum, M., and Chou, I.-M. (1993) A new diamond anvil cell for hydrothermal studies to 2.5 GPa and from 190 to 1200°C. Reviews of Scientific Instruments, 64, 2340 -2345.

Bebout, G.E., Ryan, J.G., Leeman, W.P., and Bebout, A.E. (1999) Fractionation of trace elements by subduction zone metamorphism- effect of convergent- margin thermal evolution. Earth and Planetary Science Letters, 171, 63-81.

Dolejs, D., and Manning, C.E. (2010) Thermodynamic model for mineral solubility in aqueous fluids: theory, calibration and application to model fluid-flow systems. Geofluids, 10, 20-40.

Dorogokupets, P.I, and Dewaele, A. (2007) Equations of state of MgO, Au, Pt, NaCl-B1, and NaCl-B2: Internally consistent high-temperature pressure scales. High Pressure Research: An International Journal, 27, 431-446.

Hammersley, A.P. (1997) ESRF Internal Report, ESRF97HA02T, FIT2D: An Introduction and Overview.

Hanchar, J.M., Finch, R.J., Hoskin, P.W.O, Watson, E.B., Cherniak, D.J., and Mariano, A.N. (2001) Rare earth elements in synthetic zircon: Part 1. Synthesis, and rare earth element and phosphorus doping. American Mineralogist, 86, 667-680.

Kawamoto, T., Ochiai, S., and Kagi, H. (2004) Changes in the structure of water deduced from the pressure dependence of the Raman OH frequency. Journal of Chemical Physics, 120, 5867-5870.

Kay, R.W. (1984) Elemental abundances relevant to identification of magma sources. Philosophical Transactions of the Royal Society of London, Series A, 310, 535-547.

Kessel, R., Schmidt, M.W., Ulmer, P., and Pettke, T. (2005) Trace element signature of subduction zone fluids, melts, and supercritical liquids at 120-180 km depth. Nature, 437, 724-727.

Kerrigan, R.J. (2011) Reaction Rates and textural development of hydrolysis reactions in the system MgO-SiO_2-H_2O. Dissertation, University of Maryland.

Manning, C.E., Wilke, M., Schmidt, C., and Cauzid, J. (2008) Rutile solubility in albite-H_2O and $Na_2Si_3O_7$-H_2O at high temperatures and pressures by in-situ synchrotron radiation micro-XRF. Earth and Planetary Science Letters, 272, 730-737.

Sanchez-Valle, C., Martinez, I., Daniel, I., Philippot, P., Bohic, S., and Simionovici, A., (2003) Dissolution of strontianite at high P-T conditions: An in-situ synchrotron X-ray fluorescence study. American Mineralogist, 88, 978-985.

Sanchez-Valle, C., Daniel, I., Martinez, I., Simionovici, A., and Reynard, B. (2004) Progress in quantitative elemental analyses in high P-T fluids using synchrotron x-ray fluorescence (SXRF). Journal of Physics: Condensed Matter, 16, S1197-S1206.

Schmidt, C., Rickers, K., Wirth, R., Nasdala, L., and Hanchar, J. (2006) Low-temperature Zr mobility: An in situ synchrotron-radiation XRF study of the effect of radiation damage in zircon on the element release in H_2O + HCl $\pm$ SiO_2 fluids. American Mineralogist, 91, 1211.

Schmidt, C., Rickers, K., Bilderback, D.H., and Huang, R. (2007) In situ synchrotron-radiation XRF study of REE phosphate dissolution in aqueous fluids to 800°C. Lithos, 95, 87-102.

Stechern, A., Wilke, M., Schmidt, C., Rickers, K., Pascarelli, S., and Manning, C.E. (2009) XAFS measurements on Zr in aqueous fluids at high pressures and temperatures using a modified hydrothermal diamond-anvil cell. Journal of Physics: Conference Series, 190, 012058.

Strassle, T., Saitta, A.M., Le Godec, Y., Hamel, G., Klotz, S., Loveday, J.S., and Nelmes, R.J. (2006) Structure of dense liquid water by neutron scattering to 6.5 GPa and 670 K. Physcal Review Letters, 96, 067801.

Tropper, P., Manning, C.E., and Harlov, D.E. (2011) Solubility of $CePO_4$ monazite and YPO_4 xenotime in H_2O and H_2O-NaCl at 800°C and 1 GPa: Implications for REE and Y transport during high-grade metamorphism. Chemical Geology, 282, 58-66.

Wojdyr, M. (2010) Fityk: a general-purpose peak fitting program. Journal of Applied Crystallography, 43, 1126-1128.

CHAPTER 3

The mobility of Nb in rutile-saturated NaCl- and NaF-bearing aqueous fluids from 1-6.5 GPa and 300-800°C

3.1 Abstract

Rutile (TiO_2) is an important host for high field strength elements (HFSE) such as Nb in metamorphic and subduction zone environments. The observed depletion of Nb in arc rocks is often explained by the hypothesis that rutile sequesters HFSE in the subducted slab and overlying sediments, and is chemically inert with respect to aqueous fluids evolved during prograde metamorphism in the forearc to subarc environment. However, field observations of exhumed terranes, and experimental studies indicate that HFSE may be soluble in complex aqueous fluids at high pressure (i.e., >0.5 GPa) and moderate to high temperature (i.e., <300°C). In this study, we investigated experimentally the mobility of Nb in NaCl- and NaF-bearing aqueous fluids in equilibrium with Nb-bearing rutile at pressure-temperature conditions applicable to fluid evolution in arc environments. Niobium concentrations in aqueous fluid were measured directly by using a hydrothermal diamond anvil cell (HDAC) and synchrotron x-ray fluorescence (SXRF) at 2.1 to 6.5 GPa and 300-500°C, and indirectly by performing mass loss experiments in a piston-cylinder (PC) apparatus

at ∼1 GPa and 700-800°C. The concentration of Nb in a 10 wt% NaCl aqueous fluid increases from 6 to 11 ppm as temperature increases from 300 to 500°C, over a pressure range from 2.1 to 2.8 GPa, consistent with a positive temperature dependence. The concentration of Nb in a 20 wt% NaCl aqueous fluid varies from 55 to 150 ppm at 300 to 500°C, over a pressure range from 1.8 to 6.4 GPa; however, there is no discernible temperature or pressure dependence. The Nb concentration in a 4 wt% NaF-bearing aqueous fluid increases from 180 to 910 ppm as temperature increases from 300 to 500°C over the pressure range 2.1 to 6.5 GPa. The data for the F-bearing fluid indicate that the Nb content of the fluid exhibits a temperature dependence between 300 and 500°C at ≥2 GPa, but there is no observed dependence on pressure. Together, the data demonstrate that the hydrothermal mobility of Nb is strongly controlled by the composition of the fluid, consistent with published data for Ti. At all experimental conditions, however, the concentration of Nb in the fluid is always lower than coexisting rutile, consistent with a role for rutile in moderating the Nb budget of arc rocks.

3.2 Introduction

Arc magmas bear a characteristic geochemical trace element signature consisting of a depletion of high field strength elements (HFSE) and enrichment in large ion lithophile elements (LILE) and light rare earth elements (LREE) relative to mid-ocean ridge basalts (Gill, 1981; Hawkesworth et al., 1991). Three working hypotheses have been developed to explain the geochemical signature of arc magmas. The first hypothesis is that ascending aqueous fluids from the slab are enriched in LILE and LREE, relative to HFSE, and thus transfer this signature to partial melts produced in the mantle. This hypothesis suggests that mineral phases (e.g., clinopyroxene) in the mantle control the HFSE budget of mantle-derived silicate melt (Hawkesworth, 1993a,b; Kelemen et al., 1990; Foley et al., 2000; Audétat and Keppler, 2005). The

second hypothesis is that melt extraction from the mantle at a back-arc spreading center depletes the mantle in HFSE prior to its interaction with slab-derived fluid at the base of the arc volcano plumbing system (McCulloch and Gamble, 1991; Woodhead et al., 1993). This hypothesis requires the mantle wedge to be re-fertilized by fluids during melt extraction. The downward motion of the subducted slab drags this depleted mantle material into the mantle wedge above the slab, yielding a strong depletion of HFSE during subsequent partial melting of the depleted mantle.

The third and most widely accepted hypothesis is that specific minerals in the subducted slab retain the HFSE during slab dehydration; for example, rutile moderates the Nb and Ta and zircon moderates Zr and Hf partitioning of the fluids that ascend into the mantle (Saunders et al., 1980; Green, 1981; Brophy and Marsh, 1986; Ryerson and Watson, 1987; Morris et al., 1990). The resulting trace element abundance patterns are preserved in arc magma owing to the very low abundances of the HFSE in the mantle and slab-evolved fluid. Experimental studies of rutile solubility in pure H_2O support this hypothesis (Audétat and Keppler, 2005; Tropper and Manning, 2005). However, Manning (2004) emphasized that slab-derived fluids are not pure H_2O, but rather contain significant amounts (i.e., up to and exceeding 10 wt% dissolved solutes) of alkalis (Na, K), halogens (Cl, F) and aluminosilicate components (i.e., Si, Al). Experimental data generated at 0.5-2 GPa and 700-1100°C demonstrate that the addition of these solutes to aqueous fluid increases the solubility of pure rutile in the fluid by several orders of magnitude relative to pure water (Audétat and Keppler, 2005; Antignano and Manning, 2008; Manning et al., 2008; Rapp et al., 2010; Hayden and Manning, 2011). For example, at 800°C and 1 GPa, the solubility of pure rutile in aqueous fluid increases from 18 ± 5 ppm Ti in pure water to 152 ± 5 ppm Ti in aqueous fluid that contains 3.162 - 2.423 wt% dissolved silicate (Antignano and Manning, 2008). Rapp et al. (2010) reported that at 800°C and 0.5 GPa, the solubility of pure rutile in aqueous fluid increased from 212 ± 18 ppm Ti

in pure water to 11,912 ppm Ti in fluid that contains 10 wt% dissolved NaF. These experimental data evince that the solubility of pure rutile in aqueous fluid varies with fluid chemistry. However, existing experimental data do not overlap with the pressure-temperature paths for subduction zones (Figure 3.1; Hacker, 2008) and require extrapolation when applied to the conditions of fluid evolution during prograde metamorphic devolatilization, which begins in the forearc at temperatures as low as 300°C (cf. Bebout et al., 1999; Hacker, 2008). Notably, all of the aforementioned studies used the solubility of pure rutile in aqueous fluid as a proxy to predict the fluid mobility of all HFSE. It has been shown that this may be appropriate for Zr (Kelemen et al., 1990). However, Jenner et al. (1994) reported much higher rutile / tonalite melt partition coefficients for Nb ($D_{Nb}^{rutile/fluid}$= 52.6) and Ta ($D_{Ta}^{rutile/fluid}$= 99.5) then for Zr ($D_{Zr}^{rutile/fluid}$= 4.76), indicating the potential error of inferring the mobility of Nb and Ta based on Ti.

The enhanced fluid compatibility of Ti in complex aqueous solutions suggests that Nb may be compatible in such fluids. There is an absence of data that constrain the mobility of HFSE such as Nb in aqueous fluid. Brenan et al., (1994) and Stalder et al. (1998) experimentally investigated the partitioning of Nb between rutile and aqueous fluid at 1-5 GPa and 900-1100°C. These pressures overlap with those in the forearc to subarc, but the temperatures are higher by several hundred degrees then those obtained by subduction (Figure 3.1). The experimental assemblage of Stalder et al. (1998) contained only pure H_2O, whereas Brenan et al. (1994) added 3 wt% SiO_2, in addition to HCl, NaCl and Al, to the fluid in three separate experiments. Brenan et al. (1994) reported that the addition of NaCl, HCl and Al to the fluid-rutile assemblage affected the value of $D_{Nb}^{rutile/fluid}$. For example, at 900°C and 1 GPa, the value of $D_{Nb}^{rutile/fluid}(\pm 1\sigma)$ was on average 193 ± 44 for water with 3 wt% SiO_2, and increased to 217 ± 72 with the addition of $1m$ HCl-fluid; 325 ± 107 with the addition of $1m$ NaCl-fluid; and 484 ± 140 for fluid that contained 300 ppm Al.

Similar results were reported for Ta (Brenan et al., 1994). These results suggest that the compatibility of HFSE in aqueous fluid in equilibrium with rutile is quite low and that the partitioning of HFSE from rutile to aqueous fluid actually decreases with increasing complexity of the aqueous fluid. This finding is at odds with solubility data for pure rutile in complex aqueous fluids as mentioned above (Audétat and Keppler, 2005; Antignano and Manning, 2008; Manning et al., 2008; Rapp et al., 2010; Hayden and Manning, 2011).

To quantitatively evaluate the fluid mobility of HFSE in light of the more recent experimental studies mentioned above that support a strong role of fluid chemistry in dissolving rutile (i.e., up to 1 wt% Ti in the fluid), and presumably other HFSE, there is the critical need to assess experimentally the effects of prograde metamorphic devolatilization and the relationship between fluid chemistry and trace element mobility at pressures and temperatures where fluids evolve during subduction. In this study, new experimental data is presented that quantify the mobility of Nb in rutile-saturated NaCl- and NaF-bearing aqueous fluids from 1 to 6.5 GPa and 300 to 800°C, pressure and temperature conditions appropriate for prograde devolatilization paths in cold to hot subduction zones (Figure 3.1).

3.3 Experimental Methods

3.3.1 Rutile Synthesis and Characterization

The synthetic Nb-doped rutile (Nb-TiO_2) crystals used in this study were prepared following the method described in Hanchar et al. (2001). High-purity TiO_2 and Nb_2O_5 were weighed to achieve 6 mol% TiO_2 and 0.09 mol% Nb_2O_5, then mixed in an HNO_3-cleaned agate mortar and pestle under absolute ethanol and allowed to dry. Once dried, the powders were mixed under absolute ethanol with the fluxing agents Li_2MoO_4 and MoO_3 in the following proportions: 84 mol% MoO_3 and 10 mol%

Li_2MoO_4; and the remaining TiO_2 - Nb_2O_5 mixture, mentioned above, then allowed to dry. The mixture was then transferred to an HNO_3 -cleaned Pt crucible with a tightly fitted Pt lid. The crucible was lowered into the "hot spot"of a preheated (1200°C) Deltech $MoSi_2$ vertical tube furnace and held at constant temperature for seven days, permitting the flux to evaporate. Using a type S control thermocouple, the temperature in the hot spot was measured to be stable within ±5°C. When rutile saturation was reached, the rutile crystals began to grow in the residual flux. Upon completion of the synthesis, no residual flux remained in the crucible. The crystals were removed from the Pt crucible with tweezers and cleaned in concentrated HNO_3. Powder x-ray diffraction was done to ensure that the rutile structure was obtained and not the TiO_2 polymorphs brookite or anatase.

The concentrations of Nb, Ti and Mo in the starting rutile were quantified by using wavelength dispersive spectroscopy on a Cameca SX100 electron probe microanalyzer (EPMA) and laser ablation inductively coupled mass spectroscopy (LA-ICP-MS). For EMPA, a beam current of 50 nA (calibration and analysis) and an accelerating voltage of 15 kV were used. Counting times (30 s at the peak) yielded detection limits for Nb, Ti, and Mo of approximately 330, 590 and 300 ppm, respectively. Standard ZAF techniques were used for the matrix corrections. The standards used included pure rutile (TiO_2), Nb_2O_5, and pure Mo metal. A different crystal and detector combination was used for each element: LIF for Ti; and LPET for Nb and Mo. Each crystal was imaged by using back scattered electrons (BSE), and then a EMPA line traverse across the length of the sample was performed to evaluate chemical homogeneity. The concentrations of Nb and Mo of starting crystals were 0.95 ± 0.1 wt%, and 0.02 ± 0.03 wt%, respectively; Mo would be sourced from the flux used during mineral synthesis. Some crystals displayed zoning in BSE images, and for these crystals an analytical line traverse from the rim to the core of the crystal was preformed. The beam spot measured 5 μm and the step size for the rim to core line

traverse was 2 μm (Figure 3.2a,b). All totals summed to 100 $\pm$ 1%. Depth profiles of the Nb concentration through starting (Figure 3.2c,d and Figure 3.3a) and piston cylinder run-product (Figure 3.3b) crystals were also obtained by using LA-ICP-MS, by drilling perpendicular to crystal growth surfaces and integrating single pulses individually. The ablation rate of a single pulse amounted to about 0.10 μm depth. The LA-ICP-MS analyses were performed following the analytical method outlined in Pettke (2006) and Pettke et al. (2012). The data indicate that the starting crystals contain an average of 1.03 $\pm$ 0.2 wt% Nb, which is consistent with the EMPA results. The LA-ICP-MS data also indicate that some starting crystals have a rim (of several μm thickness) that is enriched in Nb and Mo (Figures 3.2c,d and 3.3a). For example, the LA-ICP-MS depth profile shown in Figure 3.2d indicates that the concentration of Nb at the rim of this starting rutile crystal was $\sim$8 wt%, and decreased to $\sim$1 wt% over a distance of 2 μm into the center of the crystal. This Nb-enriched rim likely reflects either a quench-effect during synthesis, or the kinetics of Nb incorporation into rutile during synthesis.

3.3.2 SXRF experiments

The HDAC (Bassett et al., 1993) used in the current study was equipped with two opposing 500 or 800 μm culet diamonds. Molybdenum wires, coiled around a tungsten carbide seat that supported each diamond anvil, provided resistive heating. Two K-type (NiCr-NiAl) thermocouples, one on each diamond, were used to measure temperature. The HDAC was heated resistively by using variable transformers that facilitated flexible heating rates and allowed us to maintain temperature stability to $\sim$5°C. The HDAC was calibrated up to 800°C by observing the melting point or phase transition of $NaNO_3$, CsCl, and NaCl, and measured temperatures were systematically lower by $\sim$0.85% relative to the actual melting point or phase transition (Kerrigan, 2011). A 1% H_2-Ar gas mixture flowed constantly through the HDAC

during the measurements to prevent corrosion of the diamonds and the heaters.

A gold-lined rhenium gasket was pre-indented to a thickness of ∼120 μm and a hole of 200 μm or 400 μm diameter was drilled for 500 and 800 μm culets, respectively. A Nb-rutile crystal, measuring approximately 40x40x20 μm by using a optical microscope, was loaded into the sample chamber. Fluids were prepared by adding known masses of NaCl and NaF to deionized, lab grade H_2O to make either a 10 wt% NaCl, 20 wt% NaCl or 4 wt% NaF aqueous solution. The fluid was then added by using a micro syringe and the HDAC was immediately sealed and pressurized to ∼0.5 GPa. There was no evaporation during loading; hence, we are confident that the salinity of the added fluid represents that added to the cell.

The SXRF experiments were done at undulator beamline 16-IDD (HPCAT) at the Advanced Photon Source (APS) synchrotron facility at Argonne National Laboratory. The incident beam energy was 27 keV. The beam was focused to a spot size of 35x50 μm full-width at half maximum (FWHM) by using a pair of Kirkpatrick-Baez mirrors. A 100 μm round pinhole was used before the HDAC to reduce the tails of the incident beam, which contained a flux of $1.14\text{x}10^{12}$ photons/s. The incident beam was projected into the sample chamber through the diamonds of the HDAC. The fluorescence from the sample was collected in a 170° backscattering geometry by using a Vortex-EX silicon drift detector that was positioned ∼0.8 m from the sample. To reduce the background, a pair of large collimating slits were placed before the detector. The energy channels of the multi-channel analyzer were calibrated with ^{55}Fe, ^{57}Co, and ^{109}Cd radioactive sources. The position and aperture of the detector was optimized by using the SXRF peak of pure Nb metal. There was no Nb contamination from any component of the HDAC, which was confirmed by SXRF analyses of an empty cell.

SXRF of the empty HDAC (0 ppm Nb) and the same HDAC containing standard solutions of 600, and 1000 ppm Nb were collected before each experimental run and

used to build a calibration curve to determine the Nb concentration of experimental fluids, similar to the process described in Tanis et al. (2012) and shown in Figure 3.5. The Nb-rutile crystal position was found visually by using an online optical microscope and confirmed by SXRF. The beam was then positioned $\geq$50 μm away from the crystal and the HDAC was rotated 5° to ensure no signal contamination from the crystal. The HDAC was heated to 300°C once the starting pressure was reached. The XRD data were collected by using a MAR 165 CCD detector placed in the forward scattering direction, and pressure was monitored throughout the run by collecting XRD patterns from the Au gasket liner. The variation of the Au lattice parameters change with pressure and thus, act as an internal pressure standard. The Au XRD patterns showed no evidence of grain growth and displayed well-defined Debye rings at all temperatures. The XRD patterns were integrated and corrected for geometric distortions by using Fit2D (Hammersley, 1997). A NIST standard CeO_2 pattern was collected and used for the XRD calibration. Gold pressure was determined by using the equation of state (EOS) developed by Dorogokupets and Dewaele (2007). The diamonds used in our HDAC assembly did not contain any modifications, such as a recess for SXRF collection (e.g., Schmidt and Rickers, 2003) which allowed us to make measurements at pressures higher than published studies in the HDAC and to collect SXRF data in a 170° backscattering geometry.

Fluorescence spectra for Nb were collected iteratively in 300 s intervals (Figure 3.4). Once the Nb peak, at a unique pressure and temperature condition, became time-invariant, it was interpreted to reflect the attainment of steady-state conditions. This took approximately 30-40 minutes at each unique pressure-temperature point. The time to reach steady state is consistent with observations reported by Sanchez-Valle et al. (2003), Schmidt et al. (2007), Manning et al. (2008), and Louvel et al. (2014). Once steady-state conditions were achieved, spectra were collected in 300 s intervals for $\sim$3 h. The temperature was then increased to 400°C, and subsequently

to 500°C, and the data collection procedure was repeated at each temperature. The SXRF experimental run conditions and results are reported in Table 3.1. Increasing the temperature of the HDAC results in a change in the pressure of the sample chamber, owing to relaxation of the Re-Au gasket. Pressure at each run temperature was quantified by using XRD patterns of Au as previously described, which allowed us to monitor changes in pressure before and after each sequence of fluorescence data were collected. The reported pressure is the average of starting and final pressure. The fluorescence spectra from the standard solutions (Figure 3.5) and high P-T experiments were separately summed, and normalized to the intensity of the incoming beam. Peak intensities were corrected for absorption in the fluid using the fluid composition and density, following the procedure described in Sanchez-Valle et al. (2003), Schmidt et al. (2007), Manning et al. (2008), and Louvel et al. (2014). A linear background was subtracted and the area of the Nb fluorescence peak was fit and integrated by using the program Fityk (Wojdyr, 2010). The integrated peak area was then normalized to time (Tanis et al., 2012). The density of the aqueous fluid was calculated after the experiment based on the experimental pressure and temperature of the run conditions by using the EOS of NaCl-H_2O fluids from Mantegazzi et al. (2013). There are no published EOS data for NaF-bearing aqueous fluid; hence, the EOS of 4 wt% NaCl-H_2O fluid was used as a proxy for the NaF-bearing aqueous fluid.

Uncertainties for the Nb concentration of the fluids measured in the SXRF experiments at high pressures and temperatures were calculated based on the fitting errors of the summed spectra, and also include propagating the fitting errors from the standard calibration. Due to the iterative nature of the SXRF experimental technique and the small crystal size, recovering and analyzing the rutile crystal from each unique pressure-temperature condition was not possible. Thus, partition coefficients for Nb between fluid and rutile were not determined. The concentration of Nb in aqueous fluid that was equilibrated with rutile was measured and the results reported

here.

3.3.3 SXRF Mapping

For experimental run 20130205 (4 wt% NaF, 300-600°C, 2.13-3.07 GPa), data were collected by using a SXRF mapping technique. The cell was positioned in direct line of the detector (versus angled to hide the crystal signal) to maximize Nb count rate. The position of the HDAC was moved in steps of 25 μm in the x (horizontal) and y (vertical) directions and SXRF spectra were taken at each x-y position, as well as, the values of the incoming and out going beam intensity. Figures 3.6a and b demonstrate how the sample chamber was mapped in 2-D (x and y position, where the color scale is beam intensity) and in 3-D (x and y position, where the z-axis and color scale are intensity), respectively. Figures 3.6c and d are similar 2-D and 3-D figures that show how the spatial position of the Nb-rutile crystal was constrained. The concentration of Nb in the fluid was determined by summing and integrating the normalized spectra, significantly away (50-75 μm) from the Nb-rutile crystal spectra. A SXRF map of the HDAC containing 300 and 600 ppm Nb standard were also collected for calibration.

3.3.4 Piston Cylinder Mass Loss Experiments

The mass loss experiments were conducted in a Griggs-type modified piston cylinder apparatus. Piston cylinder run conditions and results are provided in Table 3.2. Temperature gradients were modeled by using the "CellAssembly"thermal modeling program (Hernlund et al., 2006), and confirmed by using two thermocouples placed on each side of the capsule. The temperature gradient was a maximum of 5°C across all dimensions ($\sim$7 mm long, 5 mm outer diameter) of the capsule. Confining pressure on the sample was derived from the oil pressure in the piston cylinder ram, which was measured with an Omegadyne pressure transducer. The nominal sample pressure

was calculated by dividing the load exerted by the ram by the area of the confining pressure piston. The nominal sample pressure can deviate from the actual pressure by up to 10% owing to frictional effects (Bose and Ganguly, 1995; Burnley and Getting, 2012), which are more pronounced at low pressure. The experimental charges contained a single crystal of Nb-rutile and 30 μg fluid in a platinum capsule. The capsule design was made by cutting a $\sim$7 mm length piece of Pt tubing and welding a circular disk "lid"onto the bottom and top (after the crystal and fluid were loaded). The capsule was weighed before and after welding to ensure no fluid was lost. The starting crystal was weighed 4 times by using a Mettler XP26 DeltaRange balance, and the values averaged for accuracy, before being loaded into the capsule. The hot piston-in technique of Manning and Boettcher (1994) was used to cold compress to $\sim$50 MPa and then heating and compressing in alternating increments to minimize compression and expansion of the capsule relative to other sample assembly parts. Conditions were maintained for $\geq$8 hours once the desired pressure and temperature were attained. The sample was quenched by shutting off power to the apparatus, which results in a temperature drop to $<$30°C in $<$30 s. This minimizes, if not eliminates, back-reaction between the crystal and fluid during quench (Antignano and Manning, 2008). After quench, the capsule was cleaned and weighed, then punctured and dried at 120°C for 1 hour. The capsule was weighed again, opened, and the crystal was removed. Comparison of the total capsule weight before and after the experiments showed no fluid was lost during the experiment. The crystal was cleaned with isopropanol and weighed 4 times, and then averaged to determine the mass loss during the experiment.

Piston cylinder run products included the partially dissolved starting crystal and fine-grained quench "roe"crystals (ca. 20 μm diameter, run 20130522), consistent with crystals that formed during quench (cf. Antignano and Manning, 2008). In experiment 20130527, broken crystal fragments (ca. 0.5 mm) were recovered along with

the primary crystal. Final concentrations of Nb and Mo of rutile crystals recovered from the mass-loss experiments were determined by using EMPA and LA-ICP-MS, as previously described (Table 3.2). The EMPA and LA-ICP-MS (Figure 3.3b) results demonstrate that run-product crystals were homogeneous with respect to Nb and Ti, and contained no detectable Mo. Uncertainties for Nb concentrations in the fluid from the mass loss experiments reflect propagation of weighing errors, the analytical error from the EMPA and LA-ICP-MS analysis, as well as consideration of a thin Nb-enriched rim on the starting rutile crystal. To account for the starting crystal containing a Nb-enriched rim, a minimum value of mass loss was calculated by using the final (bulk) Nb concentration of the recovered rutile crystal from each experiment, determined by LA-ICP-MS, and a maximum value assuming 8 wt% Nb (Table 3.2). For example, in experiment 20130314, the mass loss is 24 μg. If a spherical crystal is assumed, this corresponds to a radius difference of $\sim$5 μm, which is on the order of the rim distance for some of the starting crystals. Therefore, it can be assumed that if the crystal is homogeneous, the minimum amount of Nb dissolved into the fluid based on the final composition (0.9 wt%) is 11 ppm. The maximum amount of Nb dissolved into the fluid, if 8 wt% Nb is assumed, is 95 ppm.

3.4 Results

The concentration data for Nb in a 10 wt% NaCl - H_2O fluid, 20 wt% NaCl - H_2O fluid, and 4 wt% NaF - H_2O fluid are provided in Tables 3.1 (HDAC) and 3.2 (piston cylinder), respectively. Niobium concentrations in the fluid as a function of: a) temperature; b) pressure; and c) density are presented in Figure 3.7. Lines in Figure 3.7 are to provide qualitative insight to the general trends of the data and are not statistical best fits.

The diffusion coefficient of Nb in rutile ranges from D=5.6x10^{-19} to 3x10^{-21} m^2/s at 800°C (Sheppard et al., 2007; Marschall et al., 2013) and would be lower when

extrapolated to the experimental conditions of this study. Over the timescales of the experiments (t <10 hrs) the diffusion distance would be less then 0.14 μm. Therefore, it can be assumed that the Nb:Ti ratio of the rutile did not change during the experiments and Nb concentrations are controlled by rutile solubility. However, due to the high uncertainty of the Nb concentrations of the starting rutile crystals, discussed previously, Ti concentrations of the fluid cannot be calculated.

Niobium concentrations in 10 wt% NaCl-bearing aqueous fluid at 2.1-2.8 GPa range from 6 ppm at 300°C to 11 ppm at 500°C (Table 3.1; Figure 3.7), and at 1 GPa from 11-95 ppm (minimum to maximum, see previous text) at 700°C to 80-600 ppm (minimum to maximum) at 800°C (Table 3.2; Figure 3.7a). The data indicate positive temperature dependence for the concentration of Nb in the 10 wt% NaCl-bearing aqueous fluid, and a negative pressure and density dependence (Figure 3.7). The concentration of Nb in a 20 wt% NaCl-bearing aqueous fluid over the temperature range of 300 to 600°C varies from 55 to 150 ppm, which is an increase of 2 to 3 times that of the 10 wt% NaCl-bearing fluid. However, there is no temperature, pressure and density dependance observed for the 20 wt% NaCl-bearing aqueous fluid. The Nb concentration of the 4 wt% NaF-bearing fluid ranges from 180 ppm at 300°C and 2.13 GPa to 980 ppm at 500°C and 3.07 GPa, and is 220-1715 ppm (minimum to maximum) at 700°C and 1 GPa. Thus, the addition of NaF to the aqueous fluid increases the concentration of Nb in the fluid by 1 to 2 orders of magnitude relative to the addition of NaCl. The concentration of Nb in the 4 wt% NaF-bearing fluid exhibits a positive temperature dependence between 300 and 500°C at >2 GPa, and no pressure or density dependence. Overall, the new data presented here indicate that concentration of Nb and rutile solubility in saline fluids is strongly dependent on the nature and concentration of the predominant anion (i.e., Cl vs. F) of the fluid.

3.5 Discussion

In Figure 3.7, the experimentally determined Nb concentrations of rutile-saturated aqueous fluids from two published studies are plotted with data from the current study for comparison. Stalder et al. (1998) equilibrated a solid assemblage of clinopyroxene and rutile with pure H_2O at 5 GPa and 1000°C; the clinopyroxene:rutile ratio was 9:1 and 1:1 in the two experiments. They reported that the fluid contained 10.9 ppm and 37.6 ppm Nb in the two assemblages, respectively, and that the value of $D_{Nb}^{fluid/solid}$ decreased from 0.12 to 0.05, respectively. Brenan et al. (1994) equilibrated rutile and aqueous fluid at 1 and 2 GPa and 900 and 1100°C. The experimental fluids in that study contained ∼3 wt% dissolved SiO_2, and varied from pure SiO_2-bearing H_2O, to 3.6 wt% HCl-bearing H_2O, to 5.8 wt% NaCl-bearing H_2O, and one experiment with ∼300 ppm dissolved Al. Their data indicate that the concentration of Nb in the fluid phase varies by one order of magnitude, from ∼20 to 300 ppm, for pure H_2O, and was ∼30 ppm for a 5.8 wt% NaCl-bearing fluid.

The data for pure H_2O from Brenan et al. (1994) and Stalder et al. (1998) indicate that the concentration of Nb in rutile-saturated H_2O exhibits a positive temperature dependence over the range 900 to 1100°C (Figure 3.7a). This is consistent with the new data presented here for the concentration of Nb in a 10 wt% NaCl- and 4 wt% NaF-bearing aqueous fluid (Figure 3.7a). These observations suggest that temperature has a strong effect on (Ti, Nb)-Cl and (Ti, Nb)-F complexes at moderate to high temperature. However, at higher dissolved salt concentrations the anion abundance dominates over temperature. This is demonstrated by comparing the pure water data to the 10 and 20 wt% NaCl-bearing data, the temperature dependence decreases as the salinity of the fluid increases until there is an absence of a temperature dependence in the 20 wt% NaCl-bearing aqueous fluid. The temperature dependence of Nb in 4 wt% NaF- bearing fluid is also not as pronounced as in pure water or 10 wt% NaCl, while the overall concentration of Nb in the fluid is an order of magnitude

higher.

The data from Brenan et al. (1994) for the concentration of Nb in pure H_2O also indicate that the concentration of Nb in the fluid decreases with pressure (Figure 3.7b) and density (Figure 3.7c). This is consistent with results presented here for the concentration of Nb in a 10 wt% NaCl-bearing aqueous fluid. This suggests that the stability of the (Ti, Nb)-Cl complex(es) in the fluid decreases with pressure - either in total or by replacement of the dominant complex at low pressure by a different complex at high pressure, which does not complex with Ti or Nb as strongly. The data for 4 wt% NaF- and 20 wt% NaCl- bearing fluids do not exhibit any pressure dependence. This can be rationalized as a pressure-invariant stability of Nb-halogen complexes. However, it does also imply that these complexes may be different than those dominant in the 10 wt% NaCl- bearing fluid. The absence of a temperature dependence of (Ti, Nb)-solubility for the 20 wt% NaCl-bearing fluid and the weak dependence of the solubility on the 4 wt% NaF-bearing fluid are consistent with this.

The new experimental data presented here demonstrate that at temperatures of 300 to 800°C and pressures $\geq$1 GPa, the addition of NaCl and NaF to rutile-saturated aqueous fluid increases the concentration of Nb in the fluid to values higher than predicted from down-temperature extrapolations of experimental data for pure H_2O (Figure 3.7a). These new results for Nb are consistent with Rapp et al. (2010), who reported that the solubility of pure rutile in aqueous fluid, at 800-1000°C and 0.5 GPa, increased by approximately two orders of magnitude in aqueous fluid that contained 10 wt% NaCl and 10 wt% NaF, relative to pure H_2O. The new data suggest that Ti and Nb are complexed as (Ti, Nb)-chloride and (Ti, Nb)-fluoride in the NaCl-bearing and NaF-bearing experimental fluids, respectively. The determination that NaF enhances the solubility of rutile in aqueous fluid is consistent with predictions based on hard acid - soft base (HASB) considerations (Pearson, 1963), and observations from natural systems that Ti and Nb are hydrothermally transported during the evolution

of ore deposits associated with alkaline magmatic systems (i.e., carbonatites; Singer, 1986; Verplanck and Van Gosen, 2011).

Timofeev et al. (2014) measured experimentally the solubility of Nb-oxide in F-bearing aqueous fluids at temperatures of 150 to 250°C and saturated water vapor pressure (SWVP). The activity of fluoride (a(F)), and pH were varied from $\sim 10^{5}$ to 10^{-2} mF and 2.1 to 2.4, respectively. They reported that at low a(F) the concentration of Nb in the fluid was pH dependent, interpreted to indicate that Nb-fluoride complexes are present in the fluid. The concentration of Nb in the fluid increased with increasing a(F), independent of pH, which was interpreted to indicate that Nb in the fluid was present as a hydroxyfluoride complex. The relative strength of Nb-halide complexes was assessed computationally by Siegbahn (1993) who performed ab initio calculations to constrain the binding energies of Nb-halide complexes. Siegbahn (1993) reported that the binding energy of Nb-F (135 kcal/mol; bond distance of 1.97Å) is greater than Nb-Cl (101 kcal/mol; bond distance of 2.46Å), which is consistent with the the measured increase of Nb in the F-bearing aqueous fluid relative to the Cl-bearing aqueous fluid in the present study. In general, binding energies for metal-halide complexes increase in the order Y > Zr > Nb > Mo > Tc > Ru > Rh > Pd, which is also consistent with findings for the strongly enhanced concentration of Y in Cl-bearing aqueous fluids at pressure-temperature conditions similar to those in the present study (Tanis et al., 2012). Siegbahn (1993) found that the increased strength of Nb-F relative to Nb-Cl is related to the interaction between the $4d_{\pi}$ orbital and the lone pairs of halides, which yields a symmetry that is conducive to attraction by electron donation. The consistency among experimental data sets reported by Timofeev et al. (2014) and Rapp et al. (2010), as well as the ab initio results reported by Siegbahn (1993), with the new data seems to convincingly demonstrate that Nb is fluid-mobile as a Nb-halide complex in saline aqueous fluids.

3.6 Implications

The new data presented in this study have implications for the mobility of HFSE in aqueous fluids evolved during prograde metamorphic dehydration reactions that occur during subduction. Brouwer et al. (2012) reported an order of magnitude variation in the concentration of Nb in eclogites from the Franciscan Complex (California) and the Monviso Complex (Western Alps Lago Superiore region). These exhumed terranes equilibrated at a pressure of 1.05 GPa and 600 and 500°C, respectively. Brouwer et al. (2012) invoked the composition of the fluid and degree of fluid-rock interaction as the cause of the order-of-magnitude variation in measured Nb concentrations of the residual rock. The new data presented here indicate that moderately saline aqueous fluid could effect the variability observed in the Franciscan and Monviso Complexes.

Spandler et al. (2011) reported that high-pressure veins that cut through eclogite facies (∼2 GPa, ∼600°C) Fe-Ti metagabbros in the Monviso Lago Superiore region record subsolidus influx of multiple generations of internally- and externally-derived fluid. The veins contain rutile, garnet, talc and accessory ziron, and the authors reported that rutile grains exhibit zonation of Nb similar to that displayed by other trace elements (e.g., Cr). They also reported extreme Nb enrichment of other minerals such as high-Cr omphacite and garnet, which were assumed to co-precipitate from aqueous fluid. They concluded that the composition of the externally derived fluid responsible for the precipitation of these Cr-rich and Nb-bearing vein minerals (e.g., omphacite, garnet and rutile) was not only rich in Cr, but also rich in Ni, B, As, Sb and LREE/MREE. The authors noted that Nb might also have been enriched in the fluid phase, although they did not rule out that crystal-chemical effects might dominate Nb incorporation into rutile. Dehydration of serpentitite was invoked as the most plausible source of fluid that would provide multiple episodes of fluid influx and produce the chemistry of the veins (Spandler et al., 2011). Serpentinite dehydration can liberate up to 90% of Cl, more than 80% of B and about 50% of Sr from the

serpentinite into the fluid, and such fluids can be enriched in Nb, Zr, and LREE (Spandler et al., 2009; Kodolnyi and Pettke, 2011). While Nb and other elements such as Ti, Zr, Hf, Cr and Ni, are generally regarded as fluid-immobile in subduction zone environments, Spandler et al. (2011) pointed out that the chemical signatures of the veins at Monviso require fluid mobility of Nb and these other elements. Elevated Cl abundances in aqueous fluid would favor scavenging and transport of Nb, as indicated by the data presented in the current study. In fact, high salinity fluid inclusions have been reported for the Monviso gabbros, consistent with the presence of a saline fluid during prograde metamorphism (Barnicoat and Cartwright, 1997; Philippot et al., 1998).

Gao et al. (2007) reported the presence of rutile crystals in hydrothermal veins located at the contact between blueschist and eclogite in exhumed rocks in the Tian Shan complex, NW China. These hydrothermal veins were interpreted by Gao et al. (2007) as evidence for local (i.e., cm to m) transport of HFSE in aqueous fluid evolved during prograde metamorphic dehydration. The eclogite records conditions of ∼1.9 GPa and 500 to 600°C, and the vein records conditions of 1.9 GPa and 490 to 580°C. These authors reported the presence of aqueous fluid inclusions with salinities of 1.57 to 4.49 wt% NaCl equivalent, and concluded that Nb, Ti and Ta were scavenged by an aqueous fluid during the dehydration of blueschist to eclogite. The new experimental data indicate that Nb would be increasingly mobile in a fluid of this composition. Gao et al. (2007) reported that fluid evolution and migration fractionated Nb, Ti and Ta from Zr and Hf, which were sequestered by titanite. Gao et al. (2007) reported that rutile and apatite co-precipitated in the hydrothermal veins. Precipitation of Cl- and F-bearing apatite would result in rapid depletion of these halogens in the fluid, resulting in destabilization of HFSE-fluorine and/or HFSE-chlorine complexes in the fluid. In turn, this would result in precipitation of rutile, which would sequester Nb and other HFSE from the fluid.

The sum of observations from natural and experimental systems demonstrate that HFSE are mobile in aqueous fluid, and that hydrothermal transport is a function of fluid composition, temperature, and for fluids with $\leq$10 wt% NaCl equivalent, also dependent on pressure and fluid density. Even in assemblages where rutile is a stable residual phase during prograde fluid evolution, effective mass transfer of Nb in the fluid phase is favored. This was demonstrated by Kessel et al. (2005) who equilibrated aqueous fluid and basalic eclogite at 4 and 6 GPa and 700 to 1200°C, and reported that $D_{Nb}^{fluid/solid}$ varies by less than a factor of about 5 between rutile absent and rutile present assemblages. Kessel et al. (2005) reported that the key parameter, at a given pressure, influencing the fluid mobility of the HFSE in aqueous subcritical fluids, melts and supercritical liquids is temperature. The new data reported here suggest that the findings of Kessel et al. (2005) could represent conservative behavior, and by adding F and Cl to the aqueous fluid the mobility of Nb (and thus most of, if not all HFSE) prominently increase (Figure 3.7), consistent with observations from exhumed terranes.

Table 3.1: Nb-rutile HDAC-SXRF experimental conditions and results

Experiment[a]	Fluid Type ($wt\%$)	Temperature (°C)	Pressure (GPa)($\pm 1\sigma$)	Fluid Density (g/cm^3)	ppm Nb in the fluid ($\pm 1\sigma$)[b,c]
20110801	10% NaCl	300	2.10(0.1)	1.25	6(1)
20110801	10% NaCl	400	2.80(0.1)	1.28	8(1)
20110801	10% NaCl	500	2.80(0.1)	1.25	11(2)
20110804	20% NaCl	300	2.05(0.1)	1.38	140(20)
20110804	20% NaCl	400	2.62(0.1)	1.41	150(20)
20110804	20% NaCl	500	4.56(0.2)	1.54	150(20)
20110804	20% NaCl	600	6.36(0.2)	1.63	140(20)
20110805	20% NaCl	300	1.80(0.1)	1.21	75(7)
20110805	20% NaCl	400	2.60(0.1)	1.27	65(7)
20110805	20% NaCl	500	4.50(0.2)	1.38	55(7)
20120802	4% NaF	308	5.14(1.1)	1.50	190(25)
20120802	4% NaF	401	5.19(1.1)	1.49	560(65)
20120802	4% NaF	503	6.53(1.4)	1.54	700(70)
20130202	4% NaF	300	3.21(0.4)	1.39	200(40)
20130202	4% NaF	400	3.48(1.0)	1.37	420(80)
20130205	4% NaF	300	2.13(0.6)	1.29	180(20)
20130205	4% NaF	400	2.48(0.3)	1.30	910(90)
20130205	4% NaF	500	3.07(0.4)	1.32	980(50)

[a]Each experimental SXRF run allows us to measure the concentration of Nb in aqueous fluid at multiple P-T conditions. Rutile crystals are not recovered at each unique PT point; thus, partition coefficients are not reported.

[b]The reported uncertainty for the SXRF data reflects propagation of error from the standard calibration and peak fitting.

[c]Corrected for absorption and density as described in the text.

Table 3.2: Nb-rutile piston cylinder experimental conditions and results

Experiment ID	20130314	20130522	20130527[b]
Fluid Composition (wt%)	10% NaCl	10% NaCl	4% NaF
Time (h)	8:31	27:15	12:00
Temperature(°C) $\pm\ \sigma$)	687(2)	793(11)	692(7)
Pressure(GPa)($\pm\sigma$)	1.09(0.06)	1.04(0.02)	0.97(0.02)
Fluid (mg)	23.4	31.2	29.5
Fluid Density (g/cm^3)	1.06	1.01	0.91
[a]Crystal weight in(μg $\pm\sigma$)	547(12)	887(5)	1088(1)
[a]Crystal weight out(μg $\pm\sigma$)	523(6)	734(5)	813(162)
Mass loss(μg)	24	153	275
[c]Wt% Nb in product crystal	0.9307(.04)	1.0456(0.06)	1.0275(0.22)
[d]ppm Nb in Fluid min($\pm\sigma$)	11(1)	80(5)	220(50)
[e]ppm Nb in Fluid max($\pm\sigma$)	95(5)	600(35)	1715(370)

[a]The crystal was weighed four times and the average mass is reported. The one sigma standard deviation of the average mass is provided in parentheses.

[b]Run products contained broken crystal fragments as well as the primary crystals.

[c]Wt% Nb for final run products are from LA-ICP-MS analysis.

[d]Minimum Nb concentration in the fluid calculated by using the final wt% Nb from LA-ICP-MS. Error is calculated by propagating the error from weighing and the analytical error from the LA-ICP-MS.

[e]Maximum Nb concentration in the fluid is calculated by using 8 wt% Nb (see text for discussion).

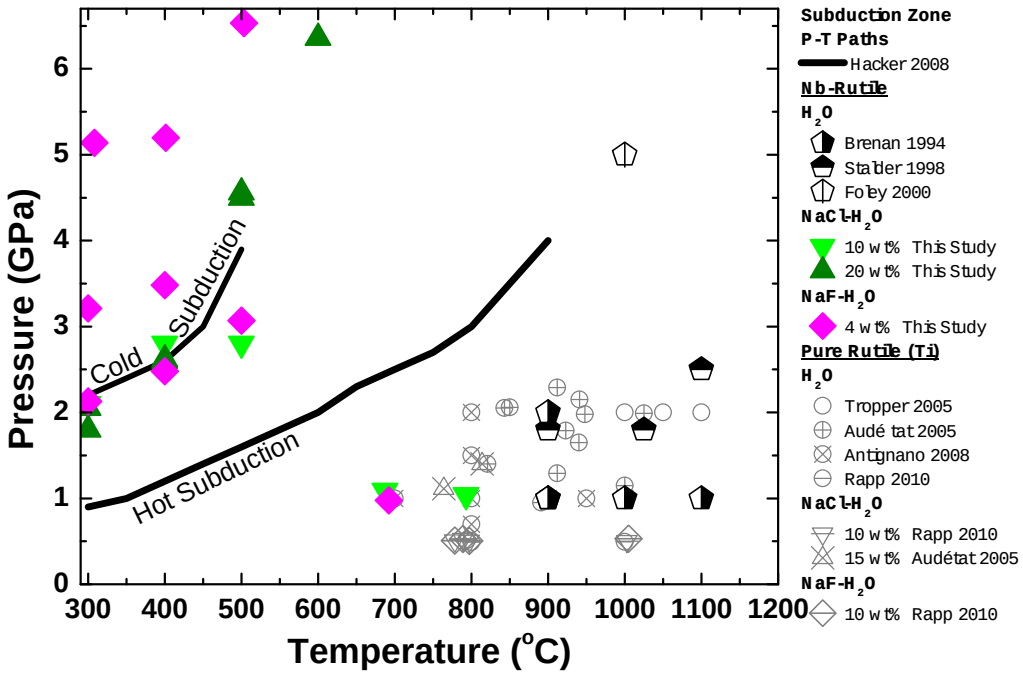

Figure 3.1: The experimental P-T conditions for the current study are plotted with respect to subduction paths for cold and hot subduction (cf. Hacker et al., 2008). The P-T conditions for published experimental data for the solubility of pure rutile in H_2O (circles, Tropper and Manning, 2005; Audétat and Keppler, 2005; Antignano and Manning 2008; Rapp et al., 2010), NaCl- aqueous fluids (triangles, Rapp et al., 2010) and NaF-aqueous fluids (diamonds, Rapp et al., 2010) bearing aqueous fluids. The P-T conditions of studies of Nb partitioning between rutile and aqueous fluid and silicate melt are also plotted (pentagons, Brenan et al., 1994, Stalder et al., 1998, Foley et al., 2000).

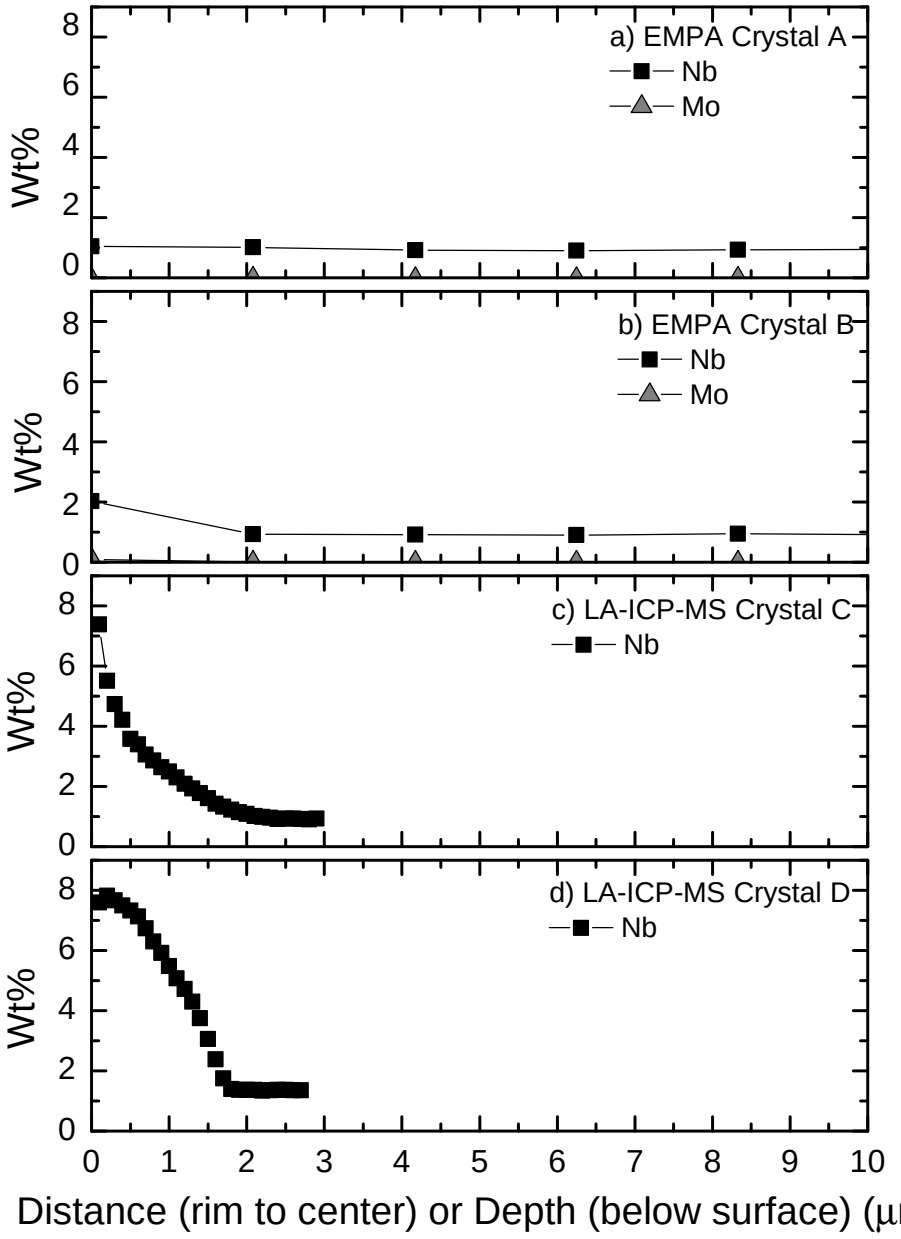

Figure 3.2: EMPA and LA-ICP-MS depth profiles of starting Nb-rutile crystals. EPMA-determined Nb (squares) and Mo (triangles) concentrations (wt%) of polished, randomly selected starting crystals as a function of distance from the rim towards the center of the crystal (a, b), and LA-ICP-MS depth profiles into the crystals perpendicular to the growth surface (c, d). The error is within the size of the symbol.

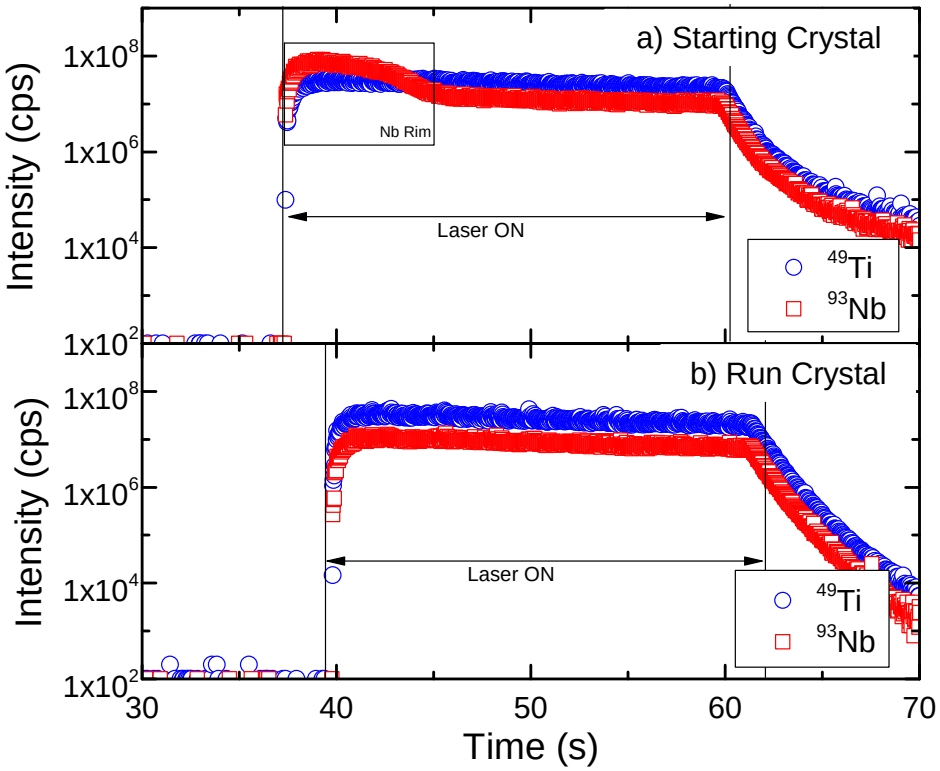

Figure 3.3: LA-ICP-MS depth profiles of starting and run-product crystals. The LA-ICP-MS depth profiles of ^{4}9Ti (blue circles) and ^{9}3Nb (red squares) concentrations in the (a) starting crystal and (b) run-product crystal from the piston cylinder-mass loss experiment 20130314. Gas background is measured for the first 30-40 seconds at which time the laser is turned on and used to ablate into the crystal. The elevated Nb signal duration in (a) corresponds to several μm thickness ablated at the LA-ICP-MS conditions employed.

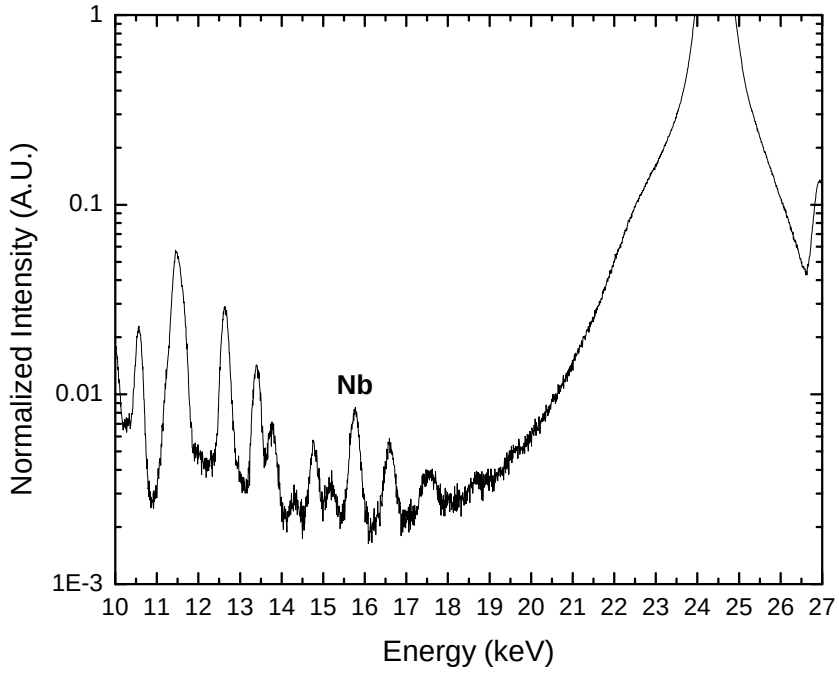

Figure 3.4: The normalized experimental spectra of the 1000 ppm Nb standard.

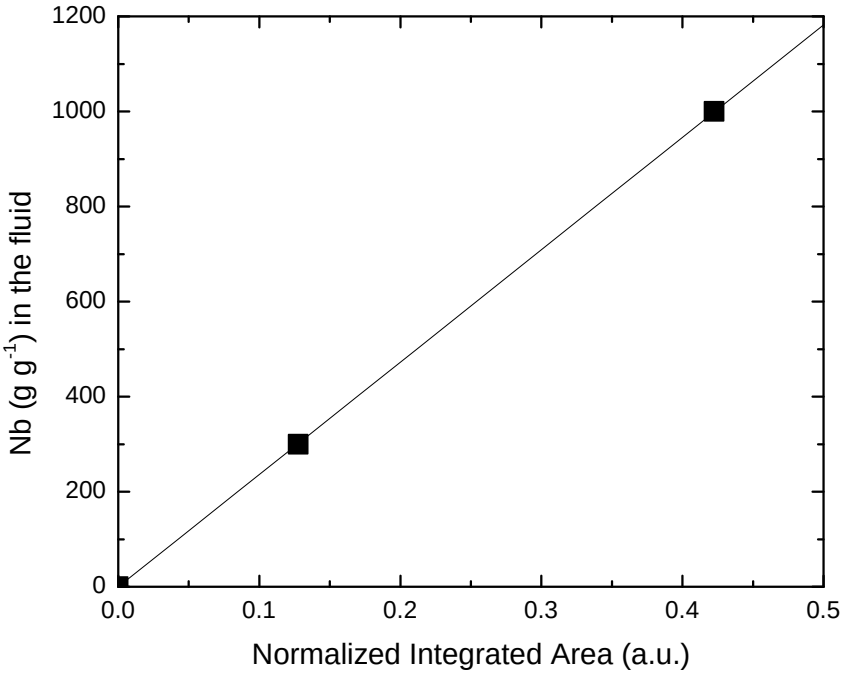

Figure 3.5: The Nb standard calibration. The normalized integrated peak area of SXRF spectra from the 300 and 1000 ppm Nb standard plotted against concentration to demonstrate linearity of the calibration.

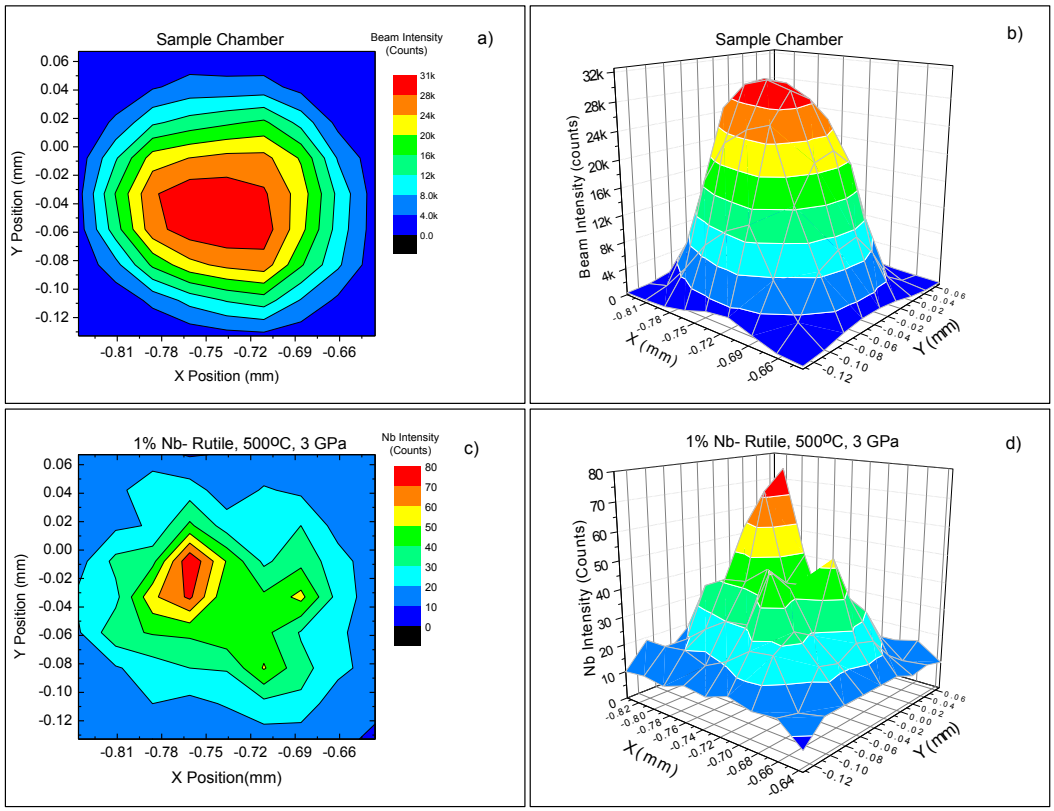

Figure 3.6: SXRF maps of the sample chamber. a) (top left) and b) (top right) 2-D and 3-D, respectively, false-color maps of x-ray beam intensity that passed through sample chamber. c) (bottom left) and d) (bottom right) 2-D and 3-D false-color maps, respectively, of the Nb signal intensity from the sample chamber. The color bar is based on beam (for a and b) or Nb intensity (for c and d). Red colors are high intensity and purple colors are low intensity. The scale is divided into 4000 count increments for beam intensity and 10 count increments for Nb intensity.

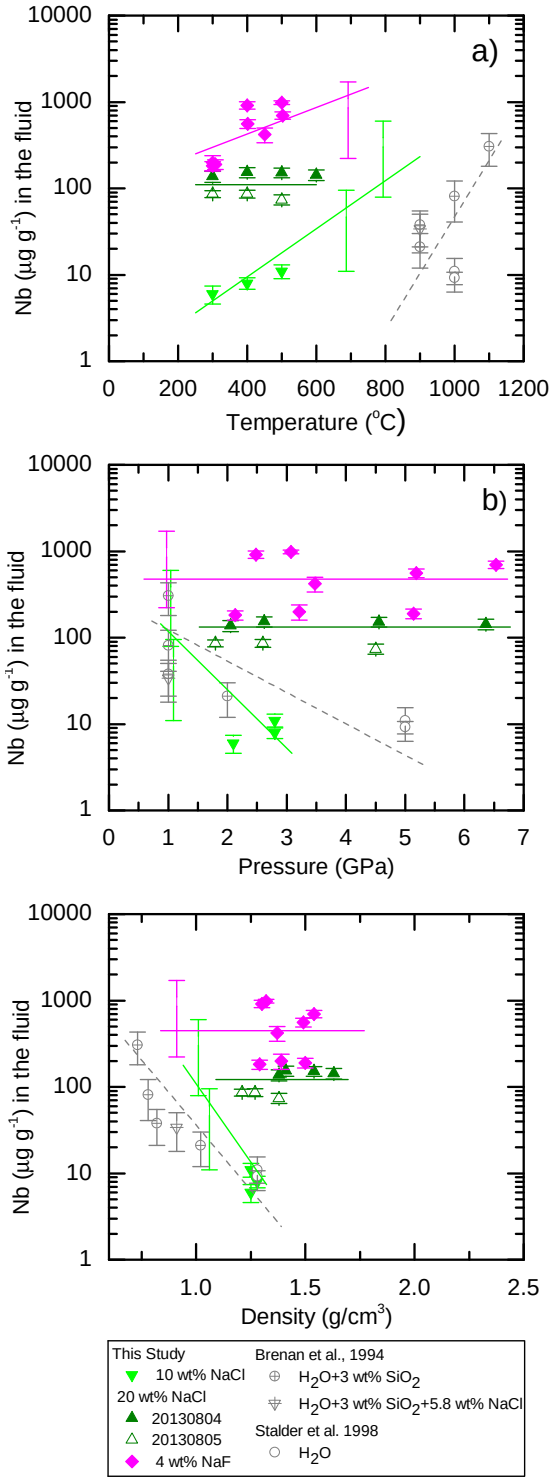

Figure 3.7: Nb concentrations in experimental aqueous fluids plotted as a function of (a) temperature, (b) pressure, and (c) fluid density. Also plotted are published data from Brenan et al., (1994) and Stalder et al., (1998). Uncertainties for Nb (ppm) are discussed in the text. The bars without symbols represent the piston cylinder data (1 GPa, 700 and 800°C) minimum and maximum Nb concentrations as described in the text.

3.7 Acknowledgements

We acknowledge NSF EAR 1264560 to Simon, Tschauner and Burnley. Portions of this work were performed at HPCAT (Sector 16), Advanced Photon Source (APS), Argonne National Laboratory. HPCAT operations are supported by DOE-NNSA under Award No. DE-NA0001974 and DOE-BES under Award No. DE-FG02-99ER45775, with partial instrumentation funding by NSF. HiPSEC provided the HDACs and part of the beamtime. HiPSEC is supported by the National Nuclear Security Administration through DOE Cooperative Agreement DE-NA0001982. APS is supported by DOE-BES, under Contract No. DE-AC02-06CH11357. We acknowledge COMPRESS and GSECARS for the use of the laser drilling system. J.M.H. thanks the Canadian Natural Sciences and Research Council (NSERC) for partial support for this research in the form of a Discovery Grant, and Memorial University of Newfoundland, for additional financial support for this project.

3.8 References

Abramson, E.H., and Brown, J.M. (2004) Equation of state of water based on speeds of sound measured in the diamond-anvil cell. Geochimica et Cosmochimica Acta, 68, 18271835.

Antignano, A., and Manning, C.E. (2008) Rutile solubility in H_2O, H_2O-SiO_2, and H_2O-$NaAlSi_3O_8$ fluids at 0.7-2.0 GPa and 700-1000°C: Implications for mobility of nominally insoluble element. Chemical Geology, 255, 283-293.

Audétat, A., and Keppler, H. (2005) Solubility of rutile in subduction zone fluids, as determined by experiments in the hydrothermal diamond anvil cell. Earth and Planetary Science Letters, 232, 393-402.

Barnicoat, A.C., and Cartwright, I. (1997) The gabbro-eclogite transformation: an oxygen isotope and petrographic study of west Alpine ophiolites. Journal of Metamorphic Geology, 15, 93-104.

Bassett, W.A., Shen, A.H., Bucknum, M., and Chou, I.-M. (1993) A new diamond anvil cell for hydrothermal studies to 2.5 GPa and from 190 to 1200°C. Reviews

of Scientific Instruments, 64, 2340-2345.

Bebout, G.E., Ryan, J.G., Leeman, W.P., and Bebout, A.E. (1999) Fractionation of trace elements by subduction zone metamorphism- effect of convergent- margin thermal evolution. Earth and Planetary Science Letters, 171, 63-81.

Bose, K., and Ganguly, J. (1995) Experimental and theoretical studies of the stabilities of talc, antigorite and phase A at high pressures with applications to subduction processes. Earth and Planetary Science Letters, 136, 109.

Brenan, J.M., Shaw, H.F., Phinney, D.L., and Ryerson, F.J. (1994) Rutile-aqueous fluid partitioning of Nb, Ta, Hf, Zr, U and Th: implications for high field strength element depletions in island-arc basalts. Earth ad Planetary Science Letters, 128, 327-339.

Brophy, J.G., and Marsh, B.D. (1986) On the Origin of High-Alumina Arc Basalt and the Mechanics of Melt Extraction. Journal of Petrology, 27, 763-789.

Brouwer, F.J., Sorensen, S.S., and Philippot, P. (2012) Physical and chemical evolution of subduction-related eclogites: Interplay of inheritance, alteration, deformation and metamorphism. AGU fall meeting abstract, V43C-2861.

Burnley, P.C., and Getting, I.C. (2012) Creating a high temperature environment at high pressure in a gas piston cylinder apparatus. Review of Scientific Instruments, 83, 014501.

Dorogokupets, P.I., and Dewaele, A. (2007) Equation of state of MgO, Au, Pt, NaCl-B1 and NaCl-B2: Internally consistent high-temperature pressure scales. High Pressure Research, 27, 431-446.

Foley, S.F., Barth, M.G., and Jenner, G.A. (2000) Rutile/melt partition coefficients for trace elements and an assessment of the influence of rutile on the trace element characteristics of subduction zone magmas. Geochimica et Cosmochimica Acta, 64, 933-938.

Gao, J., John, T., Klemd, R., and Xiong, X. (2007) Mobilization of Ti-Nb-Ta during subduction: Evidence from rutile-bearing dehydration segregations and veins hosted in eclogite, Tianshan, NW China. Geochimica et Cosmochimica Acta, 71, 4974-4996.

Gill, J.B. (1981) Orogenic Andesites and Plate Tectonics. Springer-Verlag, 390.

Green, T.H. (1981) Experimental evidence for the role of accessory phases in magma genesis. Journal of Volcanology and Geothermal Research, 10, 405-422.

Hacker, B.R. (2008) H_2O subduction beyond arcs. Geochemistry Geophysics Geosystems, 9, 1-24.

Hammersley, A.P. (1997) FIT2D: An Introduction and Overview. ESRF Internal Report, ESRF97HA02T.

Hanchar, J.M., Finch, R.J., Hoskin, P.W.O., Watson, E.B., Cherniak, D.J., and Mariano, A.N., (2001) Rare earth elements in synthetic zircon: Part 1. Synthesis, and rare earth element and phosphorus doping. American Mineralogist, 86, 667-680.

Hawkesworth, C.J., Hergt, J.M., Ellam, R.M., and McDermott, F. (1991) Element fluxes associated with subduction related magmatism. Philosophical Transactions of the Royal Society of London, 335, 393405.

Hawksworth, C.J., Gallagher, K., Hergt, J.M., and McDermott, F. (1993a) Mantle and slab contributions in arc magmas. Annual Review of Earth and Planetary Sciences, 21, 175-204.

Hawkesworth, C.J. (1993b) Trace Element Fractionation Processes in the Generation of Island Arc Basalts. Philosophical Transactions of the Royal Society of London, Series A, 342, 179-191.

Hayden, L.A., and Manning, C.E. (2011) Rutile solubility in supercritical $NaAlSi_3O_8$-H_2O fluids. Chemical Geology, 284, 74-81.

Hernlund, J., Leinenweber, K., Locke, D., and Tyburczy, J.A. (2006) A numerical model for steady-state temperature distributions in solid-medium high-pressure cell assemblies. American Mineralogist, 91, 295-305.

Jenner, G.A., Foley, S.F., Jackson, S.E., Green, T.H., Fryer, B.J., and Longerich, H.P. (1994) Determination of partition coefficients for trace elements in high pressure-temperature experimental run products by laser ablation microprobe-inductively coupled plasma-mass spectrometry (LAM-ICP-MS). Geochemica et Cosmochimica Acta, 58, 5099-5103.

Kelemen, P.B., Johnson, K.T.M., Kinzler, R.J., and Irving, A.J. (1990) High-field-strength element depletions in arc basalts due to mantlemagma interaction. Nature, 345, 521-524.

Kerrigan, R.J. (2011) Reaction Rates and textural development of hydrolysis reactions in the system MgO-SiO_2-H_2O. Dissertation, University of Maryland.

Kessel, R., Schmidt, M.W., Ulmer, P., and Pettke, T. (2005) Trace element signature of subduction-zone fluids, melts and supercritical liquids at 120-180 km depth.

Nature 437, 724-727.

Kodolányi, J., and Pettke, T. (2011) Loss of trace elements from serpentinites during fluid-assisted transformation of chrysotile to antigorite -An example from Guatemala. Chemical Geology, 284, 351-362.

Louvel, M., Sanchez-Valle, C., Malfait, W.J., Cardon, H., Testemale, D., and Hazemann, J-L. (2014) Constraints on the mobilization of Zr in magmatic-hydrothermal processes in subduction zones from in situ fluid-melt partitioning experiments. American Mineralogist, 99, 1616-1625.

Manning, C.E., Wilke, M., Schmidt, C., and Cauzid, J. (2008) Rutile solubility in albite-H_2O and $Na_2Si_3O_7$-H_2O at high temperatures and pressures by in-situ synchrotron radiation micro-XRF. Earth and Planetary Science Letters, 272, 730-737.

Manning, C.E. (2004) The chemistry of subduction-zone fluids. Earth and Planetary Science Letters, 223, 1-16.

Manning, C.E., and Boettcher, S.L. (1994) Rapid-quench hydrothermal experiments at mantle pressures and temperatures. American Mineralogist, 79, 1153-1158.

Mantegazzi, E., Sanchez-Valle, C., and Driesner, T. (2013) Thermodynamic properties of aqueous NaCl solutions to 1073 K and 4.5 GPa, and implications for dehydration reactions in subducting slabs. Geochimica et Cosmochimica Acta, 121, 263-290.

Marschall, H.R., Dohmen, R., and Ludwig, T. (2013) Diffusion-induced fractionation of niobium and tantalum during continental crust formation. Earth and Planetary Science Letters, 375, 361-371.

McCulloch, M.T., and Gamble, J.A. (1991) Geochemical and geodynamical constraints on subduction zone magmatism. Earth and Planetary Science Letters, 102, 358-374.

Morris, J.D., Leeman, W.P., and Tera, F. (1990) The subducted component in island arc lavas: Constraints from Be isotopes and B-Be systematics. Nature, 344, 31-36.

Pearson, R.G. (1963) Hard and soft acids and bases. Journal of the American chemical society, 85, 3533-3539.

Pettke, T. (2006) In situ laser-ablation-ICP-MS chemical analysis of melt inclusion and prospects for constraining subduction zone magmatism. Mineralogical Association of Canada Short Course, 36, 51-80.

Pettke, T., Oberli, F., Audétat, A., Guillong, M., Simon, A.C., Hanley, J.J., and Klemm, L.M. (2012) Recent developments in element concentration and isotope ratio analysis of individual fluid inclusions by laser ablation single and multiple collector ICP-MS. Ore Geology Reviews, 44, 10-38.

Philippot, P., Agrinier, P., and Scambelluri, M. (1998) Chlorine cycling during subduction of altered oceanic crust. Earth and Planetary Science Letters, 161, 33-44.

Rapp, J.R., Klemme, S., Butler, I.B., and Harley, S.L. (2010) Extremely high solubility of rutile in chloride and fluoride-bearing metamorphic fluids: An experimental investigation. Geology, 38, 323.

Ryerson, F.J., and Watson, E.B. (1987) Rutile saturation in magmas: implications for Ti-Nb-Ta depletion in island-arc basalts. Earth and Planetary Science Letters, 86, 225-239.

Sanchez-Valle, C., Martinez, I., Daniel, I., Philippot, P., Bohic, S., and Simionovici, A. (2003) Dissolution of strontianite at high P-T conditions: An in situ synchrotron X-ray fluorescence study. American Mineralogist, 88, 978985.

Saunders, A.D., Tarney, J., and Weaver, S.D. (1980) Transverse geochemical variations across the Antarctic Peninsula: implications for the genesis of calc-alkaline magmas. Earth and Planetary Science Letters, 46, 344360.

Schmidt, C., and Rickers, K. (2003) In-situ determination of mineral solubilities in fluids using a hydrothermal diamond-anvil cell and SR-XRF: Solubility of AgCl in water American Mineralogist, 88, 288-292.

Schmidt, C., Rickers, K., Bilderback, D.H., and Huang, R. (2007) In situ synchrotron radiation XRF study of REE phosphate dissolution in aqueous fluids to 800°C. Lithos, 95, 87-102.

Sheppard, L.R., Atanacio, A.J., Bak, T., Nowotny, J., and Prince, K.E. (2007) Bulk diffusion of niobium in single-crystal titanium dioxide. Journal of Physical Chemistry B, 111, 8126-8130.

Siegbahn, P.E.M. (1993) A comparative study of the bond strengths of the second row transition metal hydrides, fluorides, and chlorides. Theoretica Chimica Acta, 86, 219-228.

Singer, D.A. (1986) Grade and tonnage model of carbonatite deposits. In Cox, D.P. and Singerl, D.A., eds., Mineral deposit models. United States Geologial Survey Bulletin, 1693, 51.

Spandler, C., Pettke, T., and Hermann, J. (2009) The composition of serpentinite dehydration fluids in subduction zones: an experimental study. Geochimica et Cosmochimica Acta, 73, Supplement 1, A1256.

Spandler, C., Pettke, T., and Rubatto, D. (2011) Internal and External Fluid Sources for Eclogite-facies Veins in the Monviso Meta-ophiolite, Western Alps: Implications for Fluid Flow in Subduction Zones. Journal of Petrology 52, 1207-1236.

Stalder, R., Foley, S.F., Brey, G.P., and Horn, I. (1998) Mineral-aqueous fluid partitioning of trace elements at 900-1200°C and 3.0-5.7 GPa: New experimental data for garnet, clinopyroxene, and rutile, and implications for mantle metasomatism. Geochimica et Cosmochimica Acta, 62, 1781-1801.

Tanis, E.A., Simon, A.C., Tschauner, O., Chow, P., Xiao, Y., Shen, G., Hanchar, J.M., and Frank, M. (2012) Solubility of xenotime in a 2 M HCl aqueous fluid from 1.2 to 2.6 GPa and 300 to 500°C. American Mineralogist, 97, 17081713.

Timofeev, A., Migdisov, A.A., and Williams-Jones, A.E. (2014) The solubility and speciation of niobium in fluoride-bearing aqueous solutions. Goldschmidt Conference.

Tropper, P., and Manning, C.E. (2005) Very low solubility of rutile in H_2O at high pressure and temperature, and its implications for Ti mobility in subduction zones. American Mineralogist, 90, 502-505.

Verplanck, P.L., and Van Gosen, B.S. (2011) Carbonatite and alkaline intrusion-related rare earth element deposits A deposit model. United States Geological Survey Open File Report, 1256.

Wojdyr, M. (2010) Fityk: a general-purpose peak fitting program. Journal of Applied Crystallography, 43, 11261128.

Woodhead, J., Eggins, S., and Gamble, J. (1993) High field strength and transition element systematics in island arc and back-arc basin basalts: evidences for multi-phase melt extraction and a depleted mantle wedge. Earth and Planetary Science Letters, 114, 491-504.

CHAPTER 4

Rutile solubility in aqueous fluid based on SXRF measurements of Zr in Zr-doped rutile-saturated NaF-, NaCl-, KCl-, and mixed NaF-NaCl- bearing aqueous fluids from 0.5-2.79 GPa and 250-650°C

4.1 Abstract

The complex nature of trace element mobility in subduction zone environments is thought to be primarily controlled by fluid-rock interactions, episodic behavior of fluids released, mineral assemblages, and element partitioning during phase transformations and mineral breakdown throughout the transition from hydrated basalt to blueschist to eclogite. Quantitative data that constrain the partitioning of trace elements between fluid(s) and mineral(s) are required in order to model trace element mobility during prograde and retrograde metamorphic fluid evolution in subduction environments. The stability of rutile has been proposed to control the mobility of HFSE during subduction, accounting for the observed depletion of Nb and Ta in arc magmas. Recent experimental studies demonstrate that the solubility of rutile in aqueous fluids at temperatures >700°C and pressures <2 GPa increases by several orders of magnitude relative to pure H_2O as the concentrations of ligands (e.g., F and

Cl) in the fluid increase. Considering that prograde devolatilization in arcs begins at ∼300°C, there is a need for quantitative constraints on rutile solubility and the partitioning of HFSE between rutile and aqueous fluid over a wider range of temperature and pressure than is currently available. In this study, new experimental data are presented that quantify the solubility of rutile in aqueous fluids from 0.5 to 2.79 GPa and 250 to 650°C. Rutile solubility was determined by using synchrotron x-ray fluorescence to measure the concentration of Zr in a Zr-bearing rutile-saturated aqueous fluid within a hydrothermal diamond anvil cell. At the PT conditions of the experiments, published diffusion data indicate that Zr is effectively immobile (log $D_{Zr} \sim 10^{-25}$ m^2/s at 650°C and $\sim 10^{-30}$ m^2/s at 250°C); diffusion length-scales are <0.01 μm in rutile. Hence, the Zr/Ti ratio of the starting rutile, which was quantified, does not change during the experiment, and the measured concentration of Zr in the fluid was used to calculate the concentration of Ti (i.e., solubility of rutile) in the fluid. The salts NaF-, NaCl-, and KCl- were systematically added to the aqueous fluid, and the relative effects of fluid composition, pressure, and temperature on rutile solubility were quantified. The results indicate that fluid composition exerts the greatest control on rutile solubility in aqueous fluid, consistent with previous studies, and that increasing temperature has a positive, albeit less pronounced, effect. The solubility of Zr-rutile in aqueous fluid increases with the addition of halides in the order: 2 wt% NaF <30 wt% KCl <30 wt% NaCl <3 wt% NaF <10 wt% NaCl + 2 wt% NaF <4 wt% NaF. The measured concentration of Zr, and the calculated solubility of rutile, in the fluid exhibit a positive linear relationship with the NaF concentration of the fluid, increasing by an order of magnitude from 25-50 ppm for a 2 wt% NaF-bearing solution to 590-665 ppm for a 4 wt% NaF-bearing solution. These new data are consistent with observations from field studies of exhumed terranes that indicate that rutile is soluble in complex aqueous fluids, and that fluid composition is the primary control on rutile solubility and HFSE mobility.

4.2 Introduction

Rutile is an abundant accessory phase in amphibolites and eclogites where it can be the major repository of high-field-strength elements (HFSE) (Meinhold, 2010; Zack et al., 2002b), and is generally accepted as playing a role in the characteristic HFSE-depletion of arc rocks (Saunders et al., 1980; Green, 1981; Brophy and Marsh, 1986; Ryerson and Watson, 1987). The formula of rutile is TiO_2, with possible substitutions for Ti^{4+} by Nb^{5+}, Ta^{5+}, Zr^{4+}, Hf^{4+}, Cr^{3+} and Fe^{3+}. Experimental data for the partitioning of HFSE between rutile and melts indicate that rutile favors incorporation of HFSE in the order Zr > Hf > Ta > Nb (Foley et al., 2000, 2002; Klemme et al., 2005).

Rutile is generally thought to be chemically inert with respect to aqueous fluids evolved during prograde metamorphism, evinced by experimental data demonstrating that the solubility of rutile in pure water is very low (Audétat and Keppler, 2005; Tropper and Manning, 2005). However, there is a growing body of evidence from natural systems (Zack et al., 2002a,b; Manning, 2004; Gao et al., 2007, 2010; Chen and Li, 2008; Luvizotto and Zack, 2009; John et al., 2011; Spandler et al., 2011) and experimental studies (Antignano and Manning, 2008; Manning et al., 2008; Rapp et al., 2010; Hayden and Manning, 2011; Tanis et al., in review) that demonstrates that rutile is increasingly soluble in halogen-bearing aqueous fluids evolved during prograde metamorphism in subduction zone environments. Slab-derived fluids are not pure H_2O, but rather contain significant amounts of dissolved alkalis (Na, K), halogens (Cl, F) and aluminosilicate components (i.e., Si, Al) (Manning, 2004). For example, Fu et al. (2001) investigated the compositions of fluid inclusions in exhumed rocks from Shuanghe, Dabe Shan, China, and reported that the salinity of the fluid inclusions trapped during prograde metamorphic devolatilization range from almost pure water to brines that contain up to 30 wt% NaCl equivalent. Experimental data also indicate that such saline fluids have the potential to dissolve rutile (Rapp et al., 2010) during

fluid-rock interaction. Only a few studies investigated partitioning of Zr and rutile in mineral-fluid or mineral-melt experiments (Brenan et al., 1994; Jenner et al., 1994; Stalder et al., 1998; Foley et al., 2000), therefore, partitioning or solubility data involving rutile in complex aqueous fluids are critical to improving our understanding of the effects of fluid-rock interaction. In this study, new experimental data are presented that quantify the solubility of Zr-bearing rutile based on the concentration of Zr in NaF-, NaCl-, and KCl- bearing aqueous fluids at pressures of 0.5 to 2.79 GPa and temperatures of 250 to 650°C. The effect of fluid composition, pressure, and temperature on rutile solubility is studied.

4.3 Experimental Methods

4.3.1 Rutile Synthesis and Characterization

Synthetic Zr-doped rutile (Zr-TiO_2) crystals were prepared following the method described in Hanchar et al. (2001). High-purity TiO_2 (6 mol%) and ZrO_2 (0.28 mol%) were mixed to achieve 5 wt% ZrO_2 in the rutile crystals in an HNO_3-cleaned agate mortar and pestle under absolute ethanol and allowed to dry. Once dried, the powders were mixed under pure ethanol with the fluxing agents Li_2MoO_4 and MoO_3 in the following proportions: 84 mol% MoO_3 and 10 mol% Li_2MoO_4; and the remaining TiO_2 - ZrO_2 mixture, mentioned above, then allowed to dry. The mixture was then transferred to a clean Pt crucible with a tightly fitted Pt lid. The crucible was lowered into the hottest spot of a preheated (1200°C) Deltech $MoSi_2$ vertical tube furnace and held at constant temperature for seven days, permitting the flux to evaporate in air. Using a type S control thermocouple, the temperature in the hot spot was measured to be stable within ±5°C. When rutile saturation was reached, the rutile crystals began to grow in the residual flux. Upon completion of the synthesis, no residual flux remained in the crucible. The crystals were removed from the Pt

crucible with tweezers and cleaned in concentrated HNO_3. Powder x-ray diffraction was performed to ensure that the rutile structure was obtained and not the TiO_2 polymorphs brookite or anatase.

Each starting crystal was imaged by using back-scattered electrons (BSE), and most of the starting crystals displayed slight zoning (Figure 4.1). The concentrations of Zr, Ti and Mo were quantified in the starting crystals by using a Cameca SX100 electron probe microanalyzer (EPMA). A beam current of 50 nA (calibration and analysis) and an accelerating voltage of 15 kV were used. Counting times (30 s at the peak) yielded detection limits for Zr, Ti, and Mo of approximately 580, 290 and 465 ppm, respectively. Standard ZAF techniques were used for the matrix corrections. The standards included pure natural rutile (TiO_2), zircon ($ZrSiO_4$) and pure Mo metal. A different crystal and detector combination was used for each element: LIF for Ti and LPET for Zr and Mo. An EMPA line traverse, using a 5 μm focused beam with analyses spaced every 25 μm, was performed across the length of each crystal to evaluate chemical homogeneity. All totals summed to 100 $\pm$1%. The concentrations of TiO_2 and ZrO_2 in the rutile crystal chosen for the experiments were 95.74$\pm$0.35 and 4.49 $\pm$0.08 wt%, respectively, and the concentration of Mo, sourced from the flux, was 0.36 wt%. The concentration of ZrO_2 in the starting rutile is elevated relative to rutile in natural systems where rutile has been reported to contain as much as 2.98 wt% ZrO_2 (Kalfoun et al., 2002). Our experimental technique, described below, requires high enough Zr concentrations in the starting rutile in order to have sufficient Zr dissolve in the aqueous fluid to be measured at experimental conditions.

4.3.2 Experiments

A hydrothermal diamond anvil cell (HDAC, Bassett et al., 1993) was used in the current study and was equipped with two opposing 800 μm culet diamonds. Molybdenum wires, coiled around a tungsten carbide seat that supported each diamond anvil,

provided resistive heating. Two K-type (NiCr-NiAl) thermocouples, one on each diamond, were used to measure temperature. The HDAC was heated resistively by using variable transformers that facilitated flexible heating rates and allowed us to maintain temperature to ±5°C. The melting point or phase transition of $NaNO_3$, CsCl, and NaCl were used to calibrate the temperature of the HDAC up to 800°C. The measured temperatures were ∼0.85% lower then the reported melting point or phase transition of $NaNO_3$, CsCl, and NaCl (Kerrigan, 2011). A 1% H_2-Ar gas mixture flowed constantly through the HDAC during the measurements to prevent corrosion of the diamonds and the heaters.

A rhenium gasket was pre-indented to a thickness of ∼120 μm and then a hole of 600 μm diameter was drilled. The hole was filled with Au powder, compressed until the Au turned into a metallic solid and then a second 200-400 μm diameter hole was drilled. A single irregularly shaped Zr-rutile crystal measuring approximately 40x40x20 μm, as determined by using an optical microscope, was loaded into the sample chamber for each experimental run. Deionized H_2O containing either 2, 3, 4 wt% NaF, 30 wt% NaCl, 30 wt% KCl, or mixed 10 wt% NaCl + 2 wt% NaF, was then added by using a micro syringe. The HDAC was immediately sealed and pressurized to ∼0.5 GPa.

The synchrotron x-ray fluorescence (SXRF) experiments were performed at undulator beamline 16-IDD (HPCAT) at the Advanced Photon Source (APS) synchrotron facility at Argonne National Laboratory. The incident beam energy was 27 keV. The beam was focused to a spot size of 25x50 μm full-width at half maximum (FWHM) by using a pair of Kirkpatrick-Baez mirrors. A 100 μm round pinhole was used before the HDAC to reduce the tails of the incident beam, which contained a flux of 1.14×10^{12} photons/s. The incident beam was projected into the sample chamber through the diamonds of the HDAC. The fluorescence from the sample was collected in a 170° backscattering geometry by using a Vortex-EX silicon drift detector that

was positioned ∼0.8 m from the sample. To reduce the background, a pair of large collimating slits was placed before the detector. The energy channels of the multi-channel analyzer were calibrated with ^{55}Fe, ^{57}Co, and ^{109}Cd radioactive sources. The position and aperture of the detector was optimized by using the SXRF peak of pure Zr metal. SXRF data were collected by using a 2D mapping technique. The HDAC was positioned in direct line of the SXRF detector to maximize the Zr count rate. Then the HDAC was moved in steps of 25 μm in the horizontal (x) and vertical (y) directions and XRF spectra, as well as, the values of the incoming and outgoing beam intensities were collected and recorded in 30 s intervals at each x-y position (Louvel et al., 2014; Tanis et al., in review).

A SXRF map of the empty HDAC (0 ppm Zr) and the same HDAC containing standard solutions of 600, and 1000 ppm Zr were collected before each experimental run and used to build a calibration curve to determine the Zr concentration of experimental fluids, similar to the process described in Tanis et al. (2012) and shown in Figure 4.3. Before the experimental run started, the Zr-rutile crystal position was determined visually by using an online optical microscope. The pressure was increased to the starting pressure and then the temperature was increased at a steady rate of 5°C/min, until the desired temperature was reached. Fluorescence spectra (Figure 4.2) were collected in until the Zr peak area, at a unique pressure and temperature condition, became time-invariant, which was interpreted to reflect the attainment of steady-state conditions. This took approximately 30-40 minutes at each unique pressure-temperature point. The time to reach steady state is consistent with observations reported by Sanchez-Valle et al. (2003), Schmidt et al. (2007), Manning et al. (2008), Tanis et al. (2012), Wilke et al. (2012) and Tanis et al. in review. Once steady-state conditions were achieved, 2 to 3 SXRF maps were collected. The temperature was then increased to the next temperature point, and the pressure and SXRF data collection procedure was repeated.

During heating, there is some relaxation of the HDAC. This causes deformation of the Re-Au gasket sample chamber and results in a slight change in pressure. This change was observed and therefore pressure was measured before and after each sequence of fluorescence data were collected and the average pressure reported. Pressure was monitored throughout the run by collecting XRD patterns from the Au gasket liner by a MAR 165 CCD detector placed in the forward scattering direction. The XRD patterns were integrated and corrected for geometric distortions by using Fit2D (Hammersley, 1997). A NIST standard CeO_2 pattern was collected and used for the XRD calibration. Gold pressure was determined by using the equation of state (EOS) of Dorogokupets and Dewaele (2007). The experimental run conditions and results are reported in Table 4.1.

The concentration of Zr in the fluid was determined by integrating and then averaging the normalized Zr peak area from each (x, y) step significantly (50-75 μm) away from the Zr-rutile crystal. The fluorescence spectra from the standard solutions and high P-T experiments were corrected for absorption in the fluid using the fluid composition and density, then normalized to transmitted beam flux and time following the protocol described in Sanchez-Valle et al. (2003), Schmidt et al. (2007), Manning et al. (2008), and Louvel et al. (2014). . The density of the aqueous fluid was calculated after the experiment based on the experimental pressure and temperature of the run conditions by using the EOS of NaCl-H_2O fluids from Mantegazzi et al. (2013). There are no published high temperature-high pressure EOS for NaF- or KCl-bearing aqueous fluids; therefore, the EOS of NaCl-H_2O fluids were used as a proxy for the NaF- and KCl bearing fluids. A density of 2, 3, 4, and 30 wt% NaCl was used for 2, 3, 4 wt% NaF and 30 wt% KCl- bearing fluids, respectively. The density of 12 wt% NaCl was used for the mixed fluid containing 10 wt% NaCl + 2 wt% NaF (Mantegazzi et al., 2013). The background was determined by using the edges of the x, y scan where the beam hits the Re part of the gasket. The background values were consistent

with the values from the map of the empty HDAC (i.e., at 0 ppm Zr). The background was subtracted from the normalized integrated Zr fluorescence peak. Uncertainties for the Zr concentration of the fluids measured in the SXRF experiments were calculated based on the statistical deviation across the sample chamber (10-15%). Zirconium concentrations at run conditions also included propagating the fitting errors from the standard calibration. Due to the iterative nature of the SXRF experimental technique and the small size of the crystal, recovering and analyzing the rutile crystal from each unique pressure-temperature condition was not possible.

4.4 Results

The experimentally determined Zr concentrations in aqueous fluids containing 2, 3 and 4 wt% NaF, 30 wt% NaCl, 30 wt% KCl and the combined 10 wt% NaCl + 2 wt% NaF fluid are provided in Table 4.1. Zirconium concentrations in the fluid as a function of (a) temperature, (b) pressure and (c) density are presented in Figure 4.4. Lines in Figure 4.4a are trend lines and are not statistical best fits.

The data indicate a positive, albeit weak, temperature dependence (Figure 4.4a) for the concentration of Zr in each fluid composition. The concentrations of Zr in the 2 wt% NaF bearing aqueous fluid at 0.5-2.25 GPa increased from 25 ppm at 250°C to 50 ppm at 650°C. The concentration of Zr in the 3 wt% NaF-bearing aqueous fluid increases from 215 ppm at 300°C to 350 ppm at 500°C. The Zr concentration of the 4 wt% NaF-bearing fluid increases from 590 ppm at 300°C and 1.65 GPa to 665 ppm at 500°C and 2.27 GPa. Zirconium concentrations in 30 wt% NaCl-bearing aqueous fluid at 1.95-2.79 GPa increase from 110 ppm at 300°C to 140 ppm at 510°C. Zirconium concentrations in 30 wt% KCl-bearing aqueous fluid at 0.65-0.89 GPa increase from 58 ppm at 300°C to 75 ppm at 500°C. Zirconium concentrations in aqueous fluid containing both 10 wt% NaCl and 2 wt% NaF at 1.89-2.69 GPa increase from 285 ppm at 300°C to 360 ppm at 600°C.

There appears to be a slight increase in the concentration of Zr with pressure in all of the aqueous fluids (Figure 4.4b); however, this increase is attributed to the fact that the pressure in the HDAC increases as temperature increases. This is best illustrated by data for the 3 wt% NaF-bearing aqueous solution. The data indicate that the concentration of Zr in the fluid changes from 215 to 350 ppm as temperature varies from 300 to 510°C, while pressure remains relatively constant (e.g., 2.34 to 2.37 GPa). Similarly, the concentration of Zr in aqueous fluid appears to be independent of fluid density (Figure 4.4c). The densities for each fluid composition are similar for each temperature-pressure step, except in the fluids containing 3 wt% NaF, where there appears to be a slight negative density dependence.

Fluid composition is the most significant factor affecting the concentration of Zr in the fluid at all P-T conditions (Figure 4.4 and 4.5). The addition of 4 wt% NaF to the fluid increases the Zr concentration (590-665 ppm) of the fluid by up to one order of magnitude relative to a 2 wt% NaF- (25-50 ppm), 30 wt% NaCl- (110-140 ppm) and 30 wt% KCl- (58-75 ppm) bearing fluid, and ca. two times more then the addition of 3 wt% NaF (215-350 ppm) and the combined fluid of 10 wt% NaCl + 2 wt% NaF (285-360 ppm). The abundances of Zr and NaF in the fluid are positively correlated, as demonstrated by the linear fits illustrated in Figure 4.5 and listed in Table 4.2. These fits were used to calculate NaF equivalent concentrations for the 30 wt% NaCl, 30 wt% KCl and combined 10 wt% NaCl + 2 wt% NaF aqueous solution. The addition of 30 wt% NaCl is equivalent to the addition of ∼2.3 wt% NaF (Figure 4.5, triangles), which indicates that F has a much greater effect on Zr concentrations of the fluid than Cl. The addition of 30 wt% KCl is equivalent to the addition of ∼2.1 wt% NaF (Figure 4.5, circles). The combined effect of 10 wt% NaCl + 2 wt% NaF has the same effect as adding ∼3 wt% NaF (Figure 4.5, diamonds).

The concentration of Ti in the experimental aqueous fluid was calculated by assuming congruent dissolution of the starting Zr-rutile crystal (Table 4.1, Figures 4.4,

right axis, and 4.6). The diffusion coefficient of Zr in rutile is on the order of D=10^{-18} to 10^{-23} m^2/s at 800°C and can be extrapolated to lower values at the experimental conditions (Sasaki et al., 1985; Cherniak et al., 2007; Marschall et al., 2014). Over the timescales of the experiments (t <10 hrs) the diffusion distance would be less then 1 μm. Therefore, it can be assumed that the Zr:Ti ratio of the rutile did not change during the experiments.

The results for the solubility of rutile are consistent with and extend the data from Rapp et al. (2010) to lower temperatures and a wider range of fluid compositions. The data indicate an increase in Ti concentration in the fluid with increasing NaCl content (from 10 to 30 wt% NaCl; Figure 4.6, triangles). The data do not demonstrate a distinct difference in Ti concentration between the fluids containing 3 and 4 wt% NaF and 10 wt% NaF, however it must be noted that the 10 wt% NaF data from Rapp et al. (2010) span almost an order of magnitude.

4.5 Discussion

The solubility of SiO_2 and TiO_2 was considered to be dominantly controlled by increasing temperature (Ayers and Watson, 1993; Manning and Boettcher, 1994), however, however, a few studies have determined experimentally that the influence of temperature on mineral solubility was negligible compared to the effects of fluid composition (Knauss et al., 2001; Rapp et al., 2010; and Wu and Konga, 2013). Knauss et al. (2001) demonstrated that over the neutral pH range, where the species $Ti(OH)_4(aq)$ is expected to dominate, the temperature dependence is very small. Rapp et al. (2010) also demonstrated that the influence of F and Cl on the solubility of TiO_2 is more pronounced than the influence of temperature variations (Figure 4.6). Moreover, TiO_2 is more soluble in 10 wt% NaF aqueous solution than in 10 wt% NaCl aqueous solution (Rapp et al., 2010). The results of Wu and Konga (2013) show that the addition of F (at less than 0.7 wt%) slightly increases SiO_2 and Na_2O solubility

in aqueous fluid and promotes incongruent dissolution of hornblende. Our results are consistent with these studies, and demonstrate that fluid composition has the strongest effect, and that temperature effects are minimal in the temperature range investigated (e.g. 250-650°C, Figure 4.4a and 4.5).

The substitution of Ti^{4+} with Zr^{4+} is not only possible because of the same charge but also because of the similar ionic radii (e.g., Ti=74.5 pm and Zr=86pm). Therefore, it could be postulated that the speciation between Ti or Zr with Cl, F, and OH would also be similar. The review of Pokrovski, et al. (2013) showed that the most common metal-OH speciation for typical hydrothermal fluids at temperatures ≤ 500°C were the same for Zr and Ti (e.g., $Zr(OH)_4{}^0$, $Ti(OH)_4{}^0$). The Raman data of Griffith and Wickins (1967) also demonstrated that the dominant species present in acidic solutions were the same for Ti and Zr (e.g., $[(Ti,Zr)F_6]^{2-}$ and $[(Ti,Zr)Cl_6]^{2-}$). Therefore, the complexation data for Zr can be applied to Ti and vice versa.

Very few experimental studies have investigated the speciation and complexation of Cl and F with Zr and Ti. Louvel et al. (2013) reported that x-ray absorption spectroscopic (XAS) measurements and ab initio x-ray absorption near edge spectroscopic (XANES) calculations for dilute (e.g., 2.5 wt% HCl) Cl-bearing aqueous fluids did not provide evidence for extensive Zr-Cl complexation up to 420°C. They reported that Zr speciation is dominated by 8-fold-coordinated $[Zr(H_2O)_8]^{4+}$ hydrated complexes. The results of Louvel et al. (2013) may explain the low (e.g., 113-141 ppm) Zr concentrations in a 30 wt% NaCl aqueous fluid. However, ab initio simulations combined with theoretical XANES indicate that the most probable complexes in chloridic solutions are $ZrCl_4(Cl,OH)(H_2O)$. Jahn and Wilke (2014) performed ab initio molecular dynamics simulations for Zr and Hf speciation in aqueous fluids at high 1 GPa and 727°C. They reported that Zr and Hf are dissolved in aqueous fluid predominantly in octahedral coordination; i.e., each Zr is surrounded by six nearest neighbor anions (O or Cl) and that the coordination number decreases towards a pure

water solvent. These models suggest that complexation between HFSE could occur at higher concentrations of Cl.

Migdisov et al. (2011) showed that zirconium is transported in fluorine-bearing hydrothermal solutions mainly in the form of the uncharged hydroxyfluoride species $ZrF(OH)_3^\circ$ and $ZrF_2(OH)_2^\circ$. They show that the speciation and solubility of zirconium are different from those that have been previously assumed and used to evaluate the ability of natural fluids to mobilize zirconium. Consequently, the previous assumptions resulted in grossly underestimated the solubility of zirconium phases at elevated temperature. Model calculations performed for zircon show aqueous fluids can transport sufficient concentrations of zirconium, which can account for field observations that show zircon is commonly deposited in significant quantities by fluorine-rich hydrothermal fluids. Field observations also show evidence for the enrichment of HFSE in fluorine-rich granitic rock (Pollard et al., 1987) and fluorine-bearing hydrothermal systems (Salvi and Williams-Jones, 1996). Therefore it is not surprising that the addition of F into the aqueous fluid has the strongest affect on the solubility rutile.

If the following complexing reaction describes dissolution of rutile in F-bearing fluid,

$$Ti^{4+}_{(fluid)} + 4F^{-}_{(fluid)} = TiF_{4(fluid)}, \tag{4.1}$$

where TiF_4 is a complex. This complex could contain some H_2O molecules such as $TiF_4(H_2O)_2$. If the above reaction goes almost completely to the right hand side, the solubility reaction may be written as:

$$TiO_{2(rutile)} + 4F^{-}_{(fluid)} \rightarrow TiF_{4(fluid)}, \tag{4.2}$$

Hence, the solubility of rutile is roughly proportional to the fourth power of F concentration and the equilibrium constant for the reaction is $[Ti]/[F]^4$, where Ti is

dissolved Ti concentration in the fluid. This constant is roughly independent of the F concentration (Figure 4.7).

The new data presented here for the solubility of rutile in aqueous fluid demonstrate that fluid composition, specifically the halogen ion concentration, is the dominant control on the solubility of rutile in aqueous fluid (e.g., Figures 4.4 and 4.5). These results are consistent with published studies of HFSE-mineral solubility in complex, halogen-bearing aqueous fluids (Wu and Koga, 2013; Rapp et al., 2010; Louvel et al., 2013), and together evince the important roles for dissolved Cl- and F-salts to moderate HFSE compatibility in geologic fluids (Figure 4.5 and 4.6). The stronger ability of F-bearing fluids to dissolve and transport HFSE (e.g., Ti: Rapp et al., 2010; Nb: Tanis et al., in review), relative to Cl-bearing fluids is related to the local coordination of HFSE in the presence of each halogen.

4.6 Implications

The data presented here indicate that fluid composition, as well as temperature, have the strongest effect rutile solubility in aqueous fluid (Figure 4.6). Naturally, the degree of trace element, specifically HFSE, mobility is dictated by the complex nature of fluid rock interactions, episodic behavior of fluids released, mineral assemblages and element partitioning during phase transformations and mineral breakdown, however the new data give insight on the relationship between the fluid, mineral and trace element (John et al., 2008, 2011; Konrad-Schmolke et al., 2011).

Field based studies show evidence of fluid alteration textures and Zr diffusion profiles in rutile. For example, Luvizotto and Zack (2009) found Zr concentrations in rutile from the IVZ to be characterized by an anomalously large spread (from 500 to 5000 ppm within one sample) and a bimodal distribution. They interpreted the spread to be related to intense fluid influx at high-temperatures and/or to post-peak diffusional resetting favored by slow cooling rates. They describe alteration textures,

characterized by a complex network of micro-veins, as evidence for the late fluid influx that strongly affected the rutiles. By which they describe corrosion of older rutile grains and formation of rutile veinlets.

There are a plethora of studies from natural systems that demonstrate how variable amounts of fluids are released during the transition from basalt to blueschist to eclogite resulting in fluid/rock ratios high enough to mobilize trace elements such as HFSE (John et al., 2004; Gao et al. 2007; Zack and John, 2007; John et al., 2008; Beilich et al., 2010; Gao et al., 2010; Konrad-Schmolke et al., 2011; Guo et al., 2012, Shervais and Jean, 2012). Furthermore, lower fluid rock ratios may still have the ability to dissolve host phases such as rutile and thus mobilize trace elements if halogens such as F and Cl are in the fluid (Rapp et al., 2010; Migdisov et al., 2011; Louvel et al., 2013; Tanis et al., in review). This is consistent with the presented experimental data constraining Zr concentrations in a rutile saturated aqueous fluid which indicate that the addition of Cl, F and K to the aqueous fluid can strongly moderate rutile solubility during fluid rock interactions

Table 4.1: Zr-Rutile HDAC-SXRF experimental conditions and results

Experiment Run[a]	Fluid Type ($wt\%$)	Temperature (°C)	Pressure (GPa)	Fluid Density (g/cm^3)	ppm Zr in the fluid	ppm Ti in the fluid
20131003	2%NaF	250(5)[b]	0.50(0.03)[c]	1.02(0.06)[d]	25(15)[e]	280[f]
20131003	2%NaF	350(5)	1.19(0.05)	1.12(0.05)	35(15)	390
20131003	2%NaF	450(5)	1.60(0.06)	1.13(0.05)	35(10)	390
20131003	2%NaF	550(5)	2.14(0.11)	1.16(0.06)	50(20)	560
20131003	2%NaF	650(5)	2.25(0.22)	1.14(0.11)	50(30)	560
20140102	3%NaF	300(1)	2.34(0.02)	1.28(0.01)	215(50)	2400
20140102	3%NaF	403(6)	2.36(0.05)	1.24(0.03)	320(110)	3570
20140102	3%NaF	507(4)	2.37(0.01)	1.02(0.01)	350(67)	3907
20131001	4%NaF	300(5)	1.65(0.16)	1.02(0.12)	590(40)	6585
20131001	4%NaF	400(5)	1.80(0.17)	1.18(0.11)	590(35)	6585
20131001	4%NaF	500(5)	2.27(0.03)	1.02(0.02)	665(50)	7420
20131002	30%NaCl	300(5)	1.95(0.20)	1.38(0.14)	110(20)	1230
20131002	30%NaCl	397(1)	2.23(0.16)	1.38(0.10)	125(20)	1395
20131002	30%NaCl	509(8)	2.79(0.20)	1.40(0.10)	140(30)	1560
20140104	30%KCl	300(6)	0.65(0.06)	1.10(0.09)	60(15)	650
20140104	30%KCl	400(5)	0.66(0.09)	1.05(0.10)	65(15)	700
20140104	30%KCl	500(3)	0.89(0.08)	1.06(0.10)	75(20)	840
20140103	10%NaCl+2%NaF	300(6)	1.89(0.05)	1.32(0.04)	285(30)	3180
20140103	10%NaCl+2%NaF	396(2)	2.35(0.10)	1.34(0.06)	355(35)	3960
20140103	10%NaCl+2%NaF	496(2)	2.64(0.12)	1.35(0.06)	370(25)	4130
20140103	10%NaCl+2%NaF	596(4)	2.69(0.13)	1.32(0.06)	360(30)	4020

[a]Each experimental SXRF run allows us to measure the concentration of Zr in aqueous fluid at multiple P-T conditions. Rutile crystals are not recovered at each unique PT point; thus, partition coefficients are not reported.

[b]The reported uncertainty for the temperature reflects the 1σ standard deviation of recorded temperatures.

[c]The reported uncertainty for the pressure reflects the 1σ standard deviation of recorded pressures from before and after each temperature step.

[d]Density calculations are described in the text. The reported uncertainty for the density reflects the propagation of error from the pressure and temperature.

[e]The reported uncertainty for the SXRF data reflects the statistical deviation across the sample chamber and propagation of error from the standard calibration.

[f]The concentration of Ti in the fluid is based on the concentration of Zr in the fluid assuming congruent dissolution, as described in the text.

Table 4.2: Linear fits of Zr concentration with NaF concentration in the fluid.

Temperature Range	Equation	R^2
300-350°C	Zr (ppm)=273 * NaF(wt%) - 532	0.97
400-450°C	Zr (ppm)=312 * NaF (wt%) - 594	0.99
500-550°C	Zr (ppm)=311 * NaF (wt%) - 581	0.99

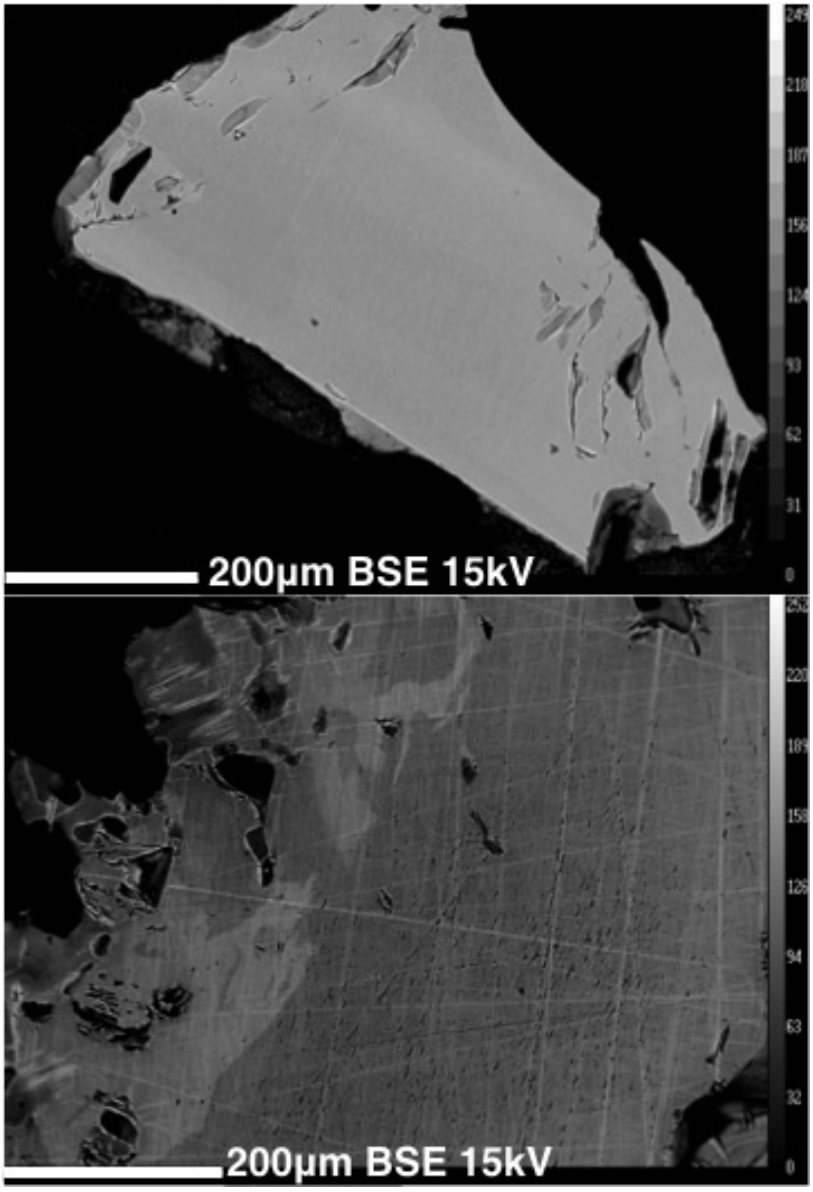

Figure 4.1: BSE images of Zr-rutile crystals. (Top) BSE image of a rutile crystal with less then 15% variation in Zr concentration. (Bottom) BSE image of non-homogeneous rutile crystal that contained large variations in Zr concentrations as an example of crystals that were not considered for experiments.

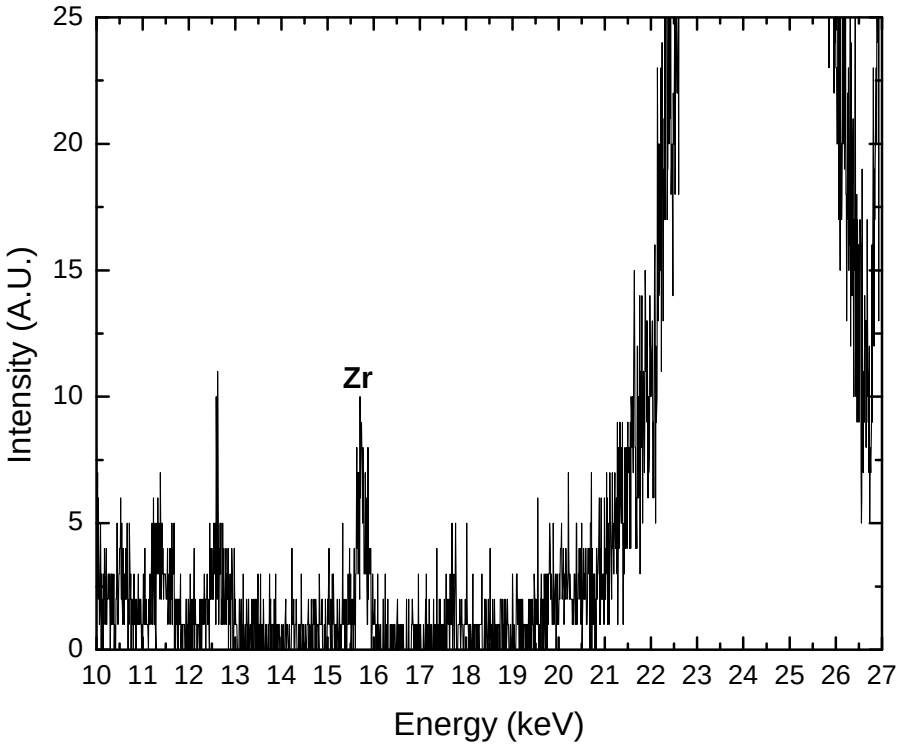

Figure 4.2: The raw XRF spectra of the 1000 ppm Zr standard solution.

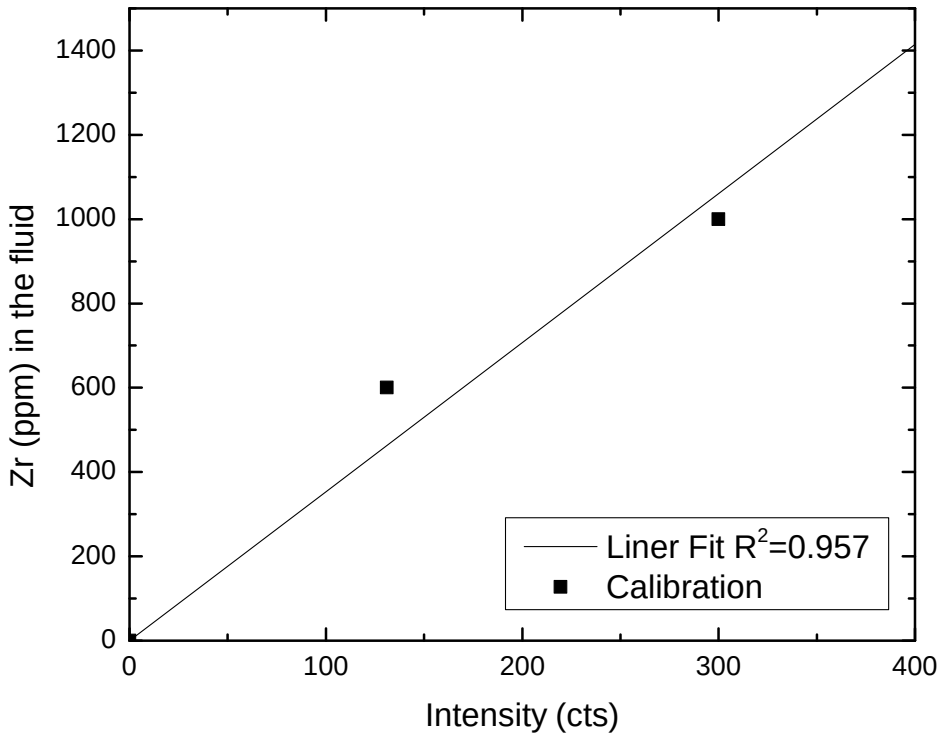

Figure 4.3: The normalized integrated peak area of the Zr standard solutions. A linear relationship (line) between concentration (600 and 1000 ppm Zr) and Zr SXRF peak area is demonstrated.

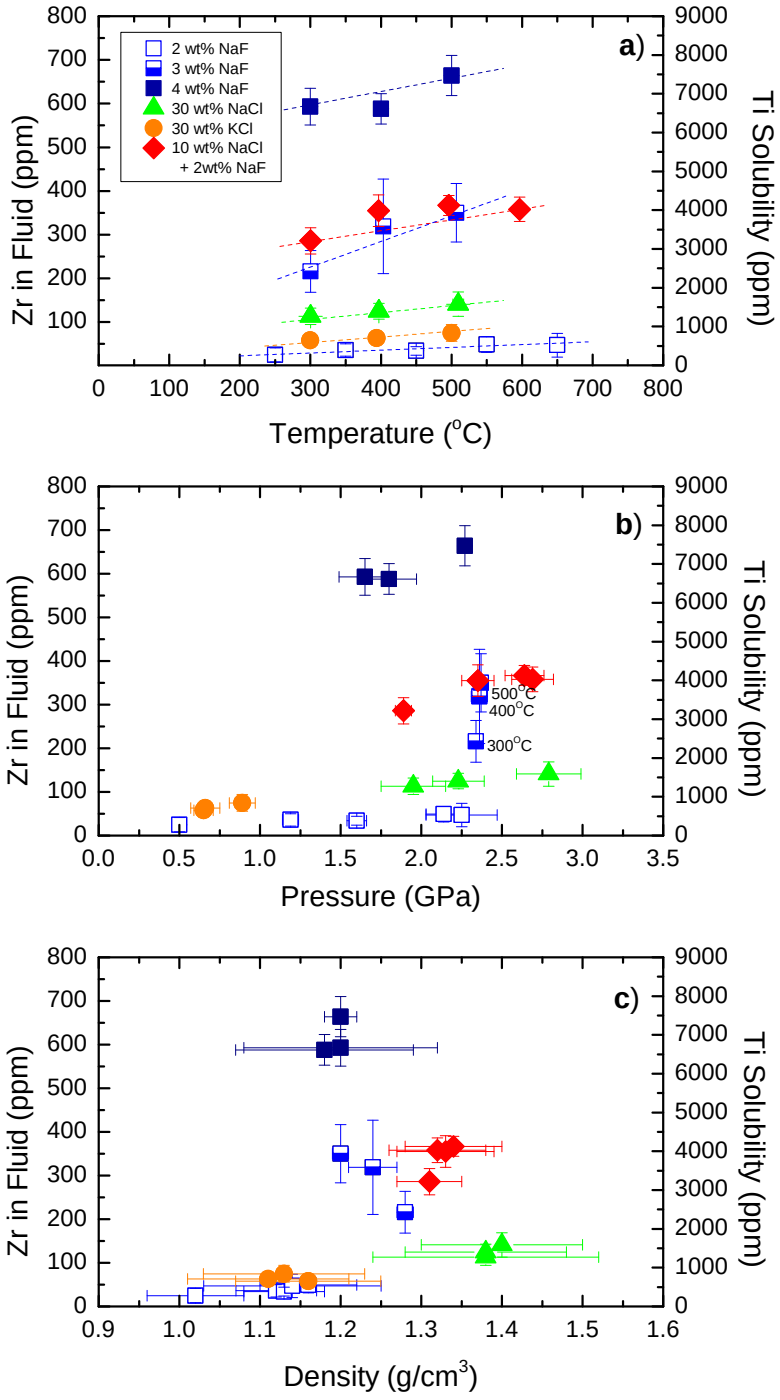

Figure 4.4: The concentrations of Zr (left axis) and Ti solubility (right axis) in experimental aqueous fluids plotted as a function of (a) temperature, (b) pressure, and (c) fluid density. Lines in (a) are trend lines and are not statistical best fits. Uncertainties for Zr (ppm) are discussed in the text, and given in Table 4.1.

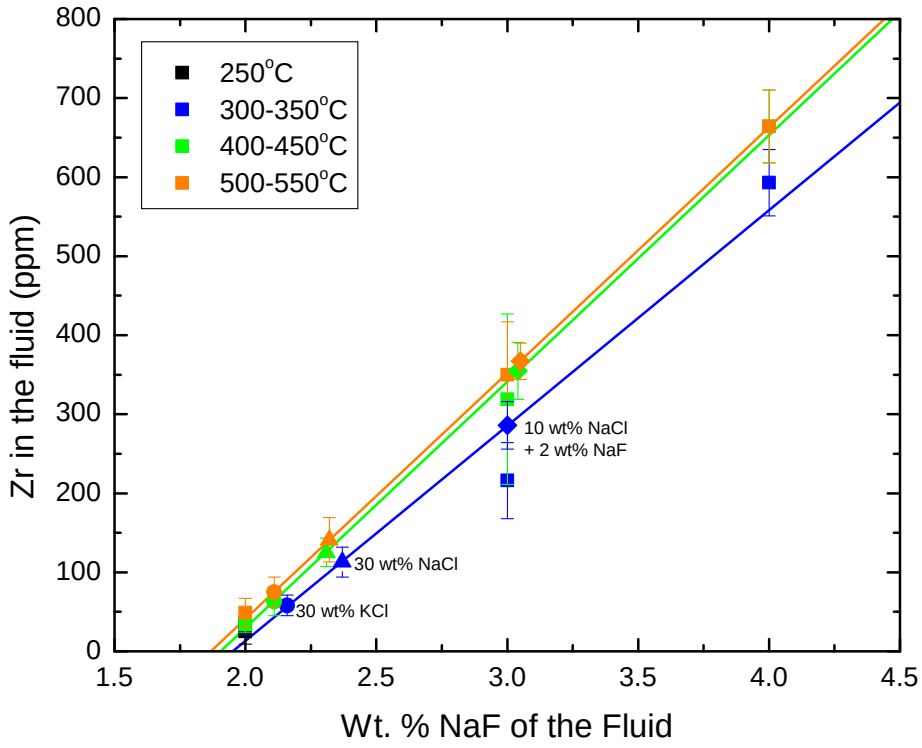

Figure 4.5: The experimentally determined Zr concentrations in aqueous fluids plotted as a function of NaF concentration of the fluid. Each color represents a different temperature, and lines represent linear fits of the Zr vs. NaF data. The concentrations of NaF equivalent wt% were calculated for a 30 wt% NaCl aqueous fluid (triangles) and a 10 wt% NaCl + 2 wt% NaF aqueous fluid (diamonds) based on the linear fits (Table 4.2). The symbols are identical to those used in Figure 4.4.

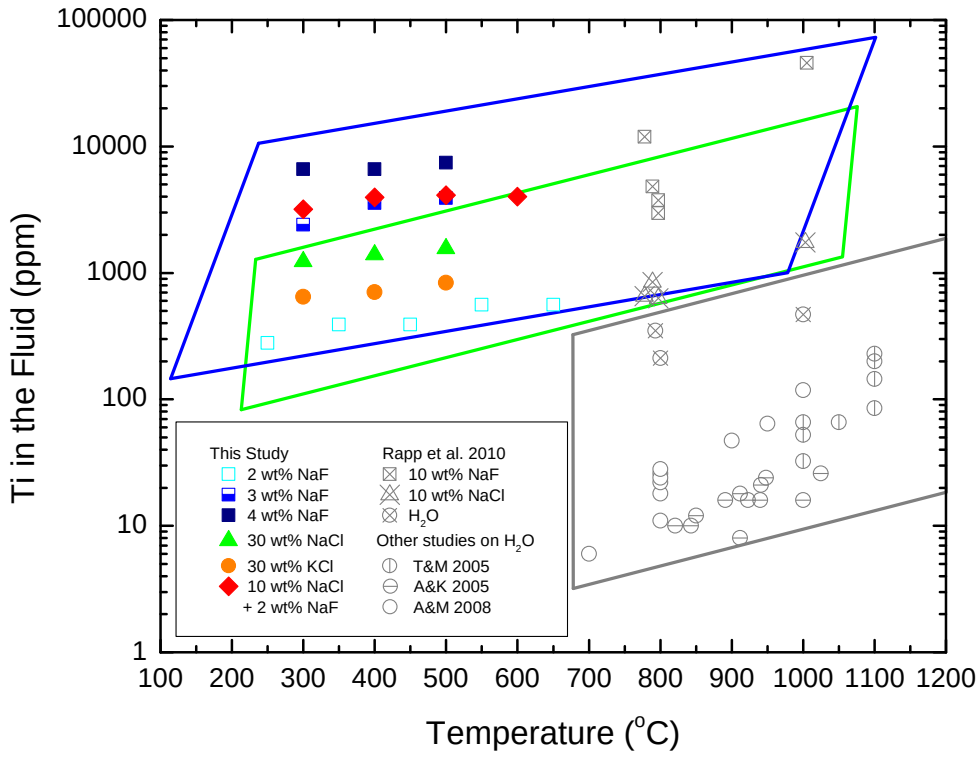

Figure 4.6: The calculated Ti concentrations in the fluid plotted as a function of temperature. The symbols for the data from the current study are in color and are identical to those used in Figure 4.4. The data are plotted with the data from Rapp et al. (2010) whom investigated rutile solubility in pure water (circles) and in aqueous fluids containing 10 wt% NaCl (triangles) or 10 wt% NaF (squares). Experimental data on rutile solubility in pure H_2O are also plotted from Tropper and Manning, 2005 (TM 2005); Audétat and Keppler, 2005 (AK, 2005) and Antignano and Manning, 2008 (AM 2008). The boxes indicate regions of data that are in fluids with the same ligands added (e.g., gray for pure H_2O; green for addition of NaCl; blue for the addition of NaF).

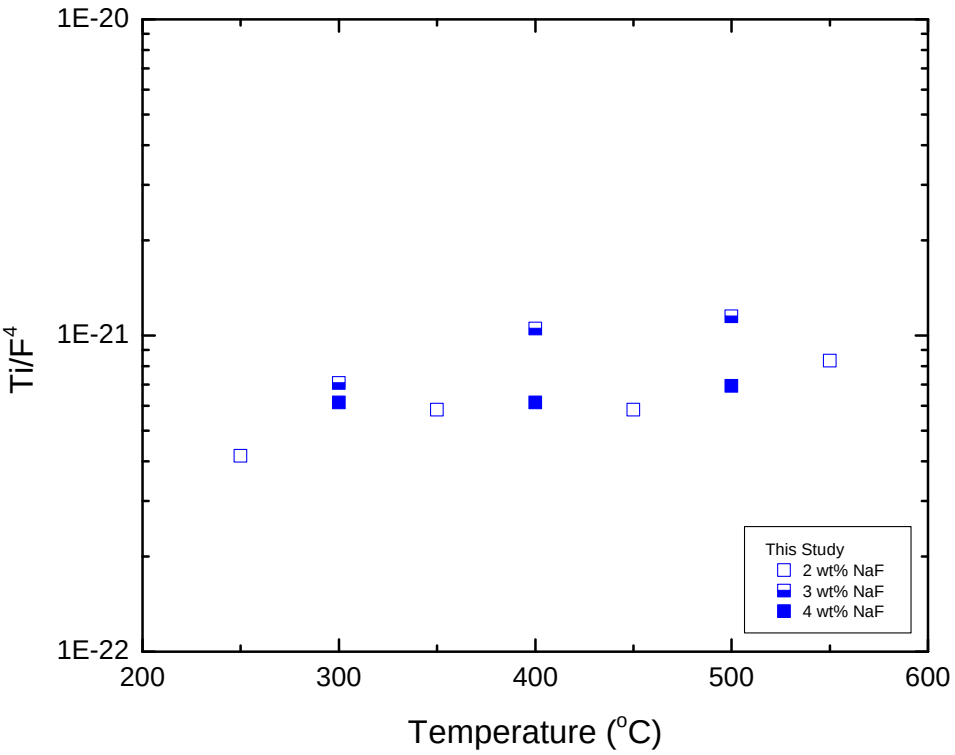

Figure 4.7: The solubility of rutile is roughly proportional to the fourth power of F concentration. The equilibrium constant for the reaction is $[Ti]/[F]^4$, where Ti is dissolved Ti concentration in the fluid. This constant is roughly independent of the F concentration

4.7 Acknowledgements

We acknowledge NSF EAR 1264560 to Simon, Tschauner and Burnley. Portions of this work were performed at HPCAT (Sector 16), Advanced Photon Source (APS), Argonne National Laboratory. HPCAT operations are supported by DOE-NNSA under Award No. DE-NA0001974 and DOE-BES under Award No. DE-FG02-99ER45775, with partial instrumentation funding by NSF. HiPSEC provided the HDACs and part of the beamtime. HiPSEC is supported by the National Nuclear Security Administration through DOE Cooperative Agreement No. DE-NA0001982. APS is supported by DOE-BES, under Contract No. DE-AC02-06CH11357. We acknowledge COMPRESS and GSECARS for the use of the laser drilling system. E.A.T. would like to thank Jaayke Knipping, Yuping Yang, Thomas Toellner and Alex Wong for their help during beamtime. J.M.H. thanks the Canadian Natural Sciences and Research Council (NSERC) for partial support for this research in the form of a Discovery Grant, and Memorial University of Newfoundland, for additional financial support for this project.

4.8 References

Abramson, E.H., and Brown, J.M. (2004) Equation of state of water based on speeds of sound measured in the diamond-anvil cell. Geochimica et Cosmochimica Acta, 68, 18271835.

Antignano, A., and Manning, C.E. (2008) Rutile solubility in H_2O, H_2O-SiO_2, and H_2O-$NaAlSi_3O_8$ fluids at 0.7-2.0 GPa and 700-1000°C: Implications for mobility of nominally insoluble element. Chemical Geology, 255, 283-293.

Audétat, A., and Keppler, H. (2005) Solubility of rutile in subduction zone fluids, as determined by experiments in the hydrothermal diamond anvil cell. Earth and Planetary Science Letters, 232, 393-402.

Ayers, J.C., and Watson, E.B. (1993) Rutile solubility and mobility in supercritical aqueous fluids. Contributions to Mineralogy and Petrology, 114, 321-330.

Bassett, W.A., Shen, A.H., Bucknum, M., and Chou, I.-M. (1993) A new diamond anvil cell for hydrothermal studies to 2.5 GPa and from 190 to 1200°C. Reviews of Scientific Instruments, 64, 2340-2345.

Brenan, J.M., Shaw, H.F., Phinney, D.L., and Ryerson, F.J. (1994) Rutile-aqueous fluid partitioning of Nb, Ta, Hf, Zr, U and Th: implications for high field strength element depletions in island-arc basalts. Earth ad Planetary Science Letters, 128, 327-339.

Brophy, J.G., and Marsh, B.D. (1986) On the Origin of High-Alumina Arc Basalt and the Mechanics of Melt Extraction. Journal of Petrology, 27, 763-789.

Chen, Z., and Li, Q. (2008) Zr-in-rutile thermometry in eclogite at Jinheqiao in the Dabie orogen and its geochemical implications. Chinese Science Bulletin, 53, 768-776.

Cherniak, D.J., Manchester, J., and Watson, E.B. (2007) Zr and Hf diffusion in rutile. Earth and Planetart Science Letters, 261, 267-279.

Dorogokupets, P.I., and Dewaele, A. (2007) Equation of state of MgO, Au, Pt, NaCl-B1 and NaCl-B2: Internally consistent high-temperature pressure scales. High Pressure Research, 27, 431-446.

Ferry, J.M., and Watson, E.B. (2007) New thermodynamic models and revised calibrations for the Ti-in-zircon and Zr-in-rutile thermometers. Contributions to Mineralogy and Petrology, 154, 429-437.

Foley, S.F., Barth, M.G., and Jenner, G.A. (2000) Rutile/melt partition coefficients for trace elements and an assessment of the influence of rutile on the trace element characteristics of subduction zone magmas. Geochimica et Cosmochimica Acta, 64, 933-938.

Foley, S.F., Tiepolo, M., and Vannucci, R. (2002) Growth of early continental crust controlled by melting of amphibolite in subduction zones. Nature, 417, 837-840.

Fu, B., Touret, J.L.R., and Zheng, Y.-F. (2001) Fluid Inclusions in coesite-bearing eclogites and jadeite quartzite at Shuanghe, Dabie Shan (China). Journal of metamorphic Geology, 19, 531-547.

Gao, J., John, T., Klemd, R., and Xiong, X. (2007) Mobilization of Ti-Nb-Ta during subduction: Evidence from rutile-bearing dehydration segregations and veins hosted in eclogite, Tianshan, NW China. Geochimica et Cosmochimica Acta, 71, 4974-4996.

Gao, C., Liu, Y., Zong, K., Hu, Z., and Gao, S. (2010) Microgeochemistry of rutile and zircon in eclogites from the CCSD main hole: Implications for the fluid activity and thermo-history of the UHP metamorphism. Lithos, 115, 51-64.

Green T.H. (1981) Experimental evidence for the role of accessory phases in magma genesis. Journal of Volcanology and Geothermal Research, 10, 405-422.

Griffith and Wickins (1967) Raman Studies on Species in Aqueous Solutions. Part 11. Oxy-species of Metals of Groups VI_A,V_A, and IV_A. Journal of the Chemical Society A: Inorganic, Physical, Theoretical, 0, 675-679.

Hammersley, A.P. (1997) FIT2D: An Introduction and Overview. ESRF Internal Report, ESRF97HA02T.

Hanchar, J.M., Finch, R.J., Hoskin, P.W.O., Watson, E.B., Cherniak, D.J., and Mariano, A.N. (2001) Rare earth elements in synthetic zircon: Part 1. Synthesis, and rare earth element and phosphorus doping. American Mineralogist, 86, 667-680.

Hayden, L.A., and Manning, C.E. (2011) Rutile solubility in supercritical $NaAlSi_3O_8$-H_2O fluids. Chemical Geology, 284, 74-81.

Henk, A., Franz, L., Teufel, S., and Oncken, O. (1997) Magmatic underplating, extension, and crustal reequilibration: insights from a cross-section through the Ivrea Zone and StronaCeneri Zone, northern Italy. Journal of Geology, 105, 367377.

Hofman, A.E., Baker, M.B., and Eiler, J.M. (2013) An experimental study of Ti and Zr partitioning among zircon, rutile and granitic melt. Contributions to Mineralogy and Petrology, 166, 235-253.

Kalfoun, F., Ionov, D., and Merlet, C., (2002) HFSE residence and Nb/Ta ratios in metasomatised, rutile bearing mantle peridotites. Earth and Planetary Science Letters, 199, 49-65.

Klemme, S., Prowatke, S., Hametner, K., and Günther, D. (2005) Partitioning of trace elements between rutile and silicate melts: Implications for subduction zones. Geochimica et Cosmochimica Acta, 69, 2361-2371.

Kerrigan, R.J. (2011) Reaction Rates and textural development of hydrolysis reactions in the system MgO-SiO_2-H_2O. Dissertation, University of Maryland.

Konrad-Schmolke, M., Zack, T., O`Brien, P.J., and Barth, M. (2011) Fluid migration above a subducted slab - Thermodynamic and trace element modelling of fluidrock interaction in partially overprinted eclogite-facies rocks (Sesia Zone, Western Alps). Earth and Planetary Science Letters, 311, 287-298.

Knauss, K.G., Dibley, M.J., Bourcier, W.L., and Shaw, H.F. (2001) Ti(IV) hydrolysis constants derived from rutile solubility measurements made from 100 to 300°C. Applied Geochemistry, 16, 1115-1128.

Jahn, S., and Wilke, M. (2014) Zr and Hf speciation in aqueous fluids at high P and T. Goldschmidt Abstract.

Jenner, G.A., Foley, S.F., Jackson, S.E., Green, T.H., Fryer, B.J., and Longerich, H.P. (1994) Determination of partition coefficients for trace elements in high pressure-temperature experimental run products by laser ablation microprobe-inductively coupled plasma-mass spectrometry (LAM-ICP-MS). Geochemica et Cosmochimica Acta, 58, 5099-5103.

John, T., Klemd, R., Gao, J., and Garbe-Schönberg, C-D. (2008) Trace-element mobilization in slabs due to non steady-state fluid-rock interaction: Constraints from and eclogite-faces transport vein in blueschists (Tianshan, China). Lithos, 103, 1-24.

John, T., Scambelluri, M., Frische, M., Barnes, J.D., and Bach, W. (2011) Dehydration of subducting serpentinite: Implications for halogen mobility in subduction zones and the deep halogen cycle. Earth and Planeary Science Letters, 308, 65-76.

Louvel, M., Sanchez-Valle, C., Malfait, W.J., Testemale, D., and Hazemann, J-L. (2013) Zr Complexation in high pressure fluids and silicate melts and implications for mobilization of HFSE in subduction zones. Geochimica et Cosmochimica Acta, 104, 281-299.

Louvel, M., Sanchez-Valle, C., Malfait, W.J., Cardon, H., Testemale, D., and Hazemann, J-L. (2014) Constraints on the mobilization of Zr in magmatic-hydrothermal processes in subduction zones from in situ fluid-melt partitioning experiments. American Mineralogist, 99, 1616-1625.

Luvizotto, G.L., and Zack, T. (2009) Nb and Zr behavior in rutile during high-grade metamorphism and retrogression: An example from the Ivrea-Verbano Zone. Chemical Geology, 261, 303-317.

Manning, C.E., and Boettcher, S.L. (1994) Rapid-quench hydrothermal experiments at mantle pressures and temperatures. American Mineralogist, 79, 1153-1158.

Manning, C.E. (2004) The chemistry of subduction-zone fluids. Earth and Planetary Science Letters, 223, 1-16.

Manning, C.E., Wilke, M., Schmidt, C., and Cauzid, J. (2008) Rutile solubility in albite-H_2O and $Na_2Si_3O_7$-H_2O at high temperatures and pressures by in-situ synchrotron radiation micro-XRF. Earth and Planetary Science Letters, 272, 730-737.

Mantegazzi, E., Sanchez-Valle, C., and Driesner, T. (2013) Thermodynamic properties of aqueous NaCl solutions to 1073 K and 4.5 GPa, and implications for dehydration reactions in subducting slabs. Geochimica et Cosmochimica Acta, 121, 263-290.

Meinhold, G. (2010) Rutile and its application in earth sciences. Earth-Science Reviews, 102, 1-28.

Migdisov, A.A., Williams-Jones, A.E., van Hinsberg, V., and Salvi, A. (2011) An experimental study of the solubility of baddeleyite (ZrO_2) in fluoride-bearing solutions at elevated temperatures. Geochimica et Cosmochimica Acta, 75, 7426-7434.

Pokrovski, G.S., Borisova, A.Y., and Bychkov, A.Y. (2013) Speciation and Transport of Metals and Metalloids in Geological Vapors. Reviews in Mineralogy and Geochemistry, 76, 165-218.

Pollard, P.J., Pichavant, M., and Charoy, B. (1987) Contrasting evolution of fluorine- and boron-rich tin systems. Mineralium Deposita, 22, 315-321.

Rapp, J.R., Klemme, S., Butler, I.B., and Harley, S.L. (2010) Extremely high solubility of rutile in chloride and fluoride-bearing metamorphic fluids: An experimental investigation. Geology, 38, 323.

Ryerson, F.J., and Watson, E.B. (1987) Rutile saturation in magmas: implications for Ti Nb Ta depletion in island-arc basalts. Earth and Planetary Science Letters, 86, 225-239.

Salvi, S., and Williams-Jones, A.E. (1996) The role of hydrothermal processes in concentrating high-field strength elements in the Strange Lake peralkaline complex, northeastern Canada. Geochimica et Cosmochimica Acta, 60, 1917-1932.

Sanchez-Valle, C., Martinez, I., Daniel, I., Philippot, P., Bohic, S., and Simionovici, A. (2003) Dissolution of strontianite at high P-T conditions: An in situ synchrotron X-ray fluorescence study. American Mineralogist, 88, 978985.

Saunders A.D., Tarney J., and Weaver S.D. (1980) Transverse geochemical variations across the Antarctic Peninsula: implications for the genesis of calc-alkaline magmas. Earth and Planetary Science Letters, 46, 344360.

Schmidt, C., Rickers, K., Bilderback, D.H., and Huang, R. (2007) In situ synchrotron radiation XRF study of REE phosphate dissolution in aqueous fluids to 800°C. Lithos, 95, 87-102.

Spandler, C., Pettke, T., and Rubatto, D. (2011) Internal and External Fluid Sources for Eclogite-facies Veins in the Monviso Meta-ophiolite, Western Alps: Implications for Fluid Flow in Subduction Zones. Journal of Petrology, 52, 1207-1236.

Stalder, R., Foley, S.F., Brey, G.P., and Horn, I. (1998) Mineral-aqueous fluid partitioning of trace elements at 900-1200°C and 3.0-5.7 GPa: New experimental data for garnet, clinopyroxene, and rutile, and implications for mantle metasomatism. Geochimica et Cosmochimica Acta, 62, 1781-1801.

Tomkins, H.S., Powell, R., and Ellis, D.J. (2007) The pressure dependence of the zirconium-in-rutile thermometer. Journal of metamorphic geology, 25, 703-713.

Tropper, P., and Manning, C.E. (2005) Very low solubility of rutile in H_2O at high pressure and temperature, and its implications for Ti mobility in subduction zones. American Mineralogist, 90, 502-505.

Watson, E.B., Wark, D.A., and Thomas, J.B. (2006) Crystallization thermometers for zircon and rutile. Contributions to Mineralogy and Petrology, 151, 413-433.

Wilke, M., Schmidt, C., Dubrail, J., Appel, K., Borchert, M., Kvashnina, K., and Manning, C.E. (2012) Zircon solubility and zirconium complexation in H_2O+Na_2O +SiO_2 ± Al_2O_3 fluids at high pressure and temperature. Earth and Planetary Science Letters, 349-350, 15-25.

Wu, J., and Koga, K. (2013) Fluorine partitioning between hydrous minerals and aqueous fluid and 1 GPa and 770-947°C: A new constraint on slab flux. Geochimica et Cosmochimica Acta, 119, 77-92.

Zack, T., Foley, S.F., and Rivers, T. (2002a) Equilibrium and disequilibrium trace element partitioning in hydrous eclogites (Trescolmen, Central Alps). Journal of Petrology 43, 1947-1974.

Zack, T., Kronz, A., Foley, S.F., and Rivers, T. (2002b) Trace element abundances in rutiles from eclogites and associated garnet mica schists. Chemical Geology 184, 97122.

Zack, T., Moraes, R., and Kronz, A. (2004) Temperature dependence of Zr in rutile: empirical calibration of a rutile thermometer. Contributions to Mineralogy and Petrology, 148, 471-488.

Zheng, Y-F., Xia, Q-X., Chen, R-X., and Gao, X-Y. (2011) Partial melting, fluid supercriticality and element mobility in ultrahigh-pressure metamorphic rocks during continental collision. Earth Science Reviews, 107, 342-374.

CHAPTER 5

Conclusions and Future Work

5.1 Summary

This dissertation presents new high pressure, high temperature experimental data that constrain the solubility of xenotime and rutile containing key trace elements (Y, Nb, Zr) in aqueous fluids containing H_2O with added Cl, F, K and Na. Experiments were conducted by using an HDAC with the analytical methods of synchrotron x-ray fluorescence and a piston-cylinder press with the analytical method of mineral mass loss. These experiments constrain the solubility of important minerals that carry geochemical tracers in aqueous fluid as a function of pressure, temperature and fluid composition and can be directly related to devolatization during subduction. In brief, the three preceding studies concluded the following:

- The solubility of xenotime decreases with increasing fluid density.
- The effect of temperature on the solubility of xenotime in aqueous fluid containing HCl decreases with increasing pressure.
- The solubility of xenotime is influenced greater by HCl, relative to NaCl.
- The concentration of Nb in aqueous fluid increases with halogen addition in the order: 10 wt% NaCl <20 wt% NaCl <4 wt% NaF.

- At higher dissolved salt concentrations, the anion abundance dominates the mobility of Nb over temperature (i.e., the temperature dependence decreases as NaCl is increases from 0 to 10 to 20 wt% NaCl).

- Rutile solubility is positively correlated with the abundances NaF in the fluid.

- The solubility of Zr- rutile in aqueous fluid increases with halogen addition in the order: 2 wt% NaF <30 wt% KCl <30 wt% NaCl <3 wt% NaF <10 wt% NaCl + 2 wt% NaF <4 wt% NaF.

5.2 Implications

The sum of the results indicate that the fluid composition exerts the greatest control on trace element mobility in aqueous fluid, and increasing temperature has a positive, albeit smaller effect then does composition. These results are consistent with field studies of exhumed terranes, which demonstrate that normally fluid immobile minerals and elements (HFSE and REE) are mobile over short (e.g., mm to m), and possibly long (e.g. 10s of m) distances. The HFSE are liberated by enhanced diffusion over long time scales and/or by the solubility of the host phases into fluid pathways. This study has shown that if there is a fluid present containing dissolved components (e.g., Cl, F, K, Na) the solubility will be enhanced and the HFSE mobilized. However, if changes in pressure, temperature, and/or wall rock interaction reduce the ligand concentration, the fluid immobile elements will precipitate into their favored solid mineral phase assemblage or find new host phases to grow in. For example, if Ti (and by extension the other HFSE) is dissolved as a hydrated HFSE-F complex in the aqueous fluid, and the fluid also carries Ca, P and O but a change in conditions causes apatite to precipitate, then the apatite will sequester F from the fluid, which results in destabilization of Ti-F, hence Ti comes out of solution and forms new phases such as rutile, which will also sequester HFSE. The Tian Shan veins investigated by

Gao et al. (2007) suggest that the fluids were able to mobilize the HFSE on the order of 10s to maybe 100s of meters. However, the subducting slab is 1000s of meters thick, therefore, at least in the Tian Shan, the HFSE, retained in rutile and zircon, were never transferred to the overlying mantle wedge. This case, and the case where the slab is not exhumed, but instead subducted deeper into the mantle support the hypothesis (number 3 from the intro) explaining the arc rock depletion signature by stable mineral phases sequester trace elements.

Given that each individual arc has a slightly different rate of subduction, angle of subduction, and sediment deposition load before subduction, the composition of the fluid evolved during subduction will contain variable amounts of dissolved ligands (e.g., Cl, F,K). This could contribute to the variability in HFSE and REE concentrations among arcs can span orders of magnitude. The degree of added ligands would cause the HFSE to be mobilized to different degrees of concentration and over different length scales (10s to 100s of meters). If some HFSE, close to the slab mantle wedge interface, make it into the mantle wedge, this would cause a more shallow depletion. Although, the overwhelming concentration of the LILE still remains, which supports the first hypothesis for the arc rock depletion signature. Our data have demonstrated that the HFSE can be mobilized, which supports the evidence found in exhumed blueschists and eclogites, but also supports two of the arc depletion hypotheses. This investigation has helped bridge what the rock record suggests from two different parts of the subduction zone process, giving key insight into the mobility of trace elements and processes involved during subduction fluid evolution.

5.3 Future work

Certain topics for future work were identified during the course of this investigation.

These topics are listed below:

1. **Solubility based on element doping:** This work demonstrated that rutile solubility could be determined by using synchrotron x- ray fluorescence to measure the concentration of Zr in a Zr-bearing rutile-saturated aqueous fluid. Due to the very slow diffusion of Zr in rutile, the Zr/Ti ratio of the starting rutile does not change during the experiment, and the measured concentration of Zr in the fluid simply reflects rutile dissolution. Hence the observed Zr solubility was used to calculate the concentration if Ti, i.e., solubility of rutile, in the fluid as function of pressure, and temperature and fluid composition. This method could be applied to other mineral systems where the doped trace element has a K_α between 10-20 keV (i.e., energy range available at the APS 16-IDD; e.g., Se, Ke, Rb, Sr, Y, Zr, Nb, Tc, Ru) and does not over lap with elements contained in the HDAC (e.g., Mo). For example, garnet is often considered to sequester the REE and Y. Yttrium-Iron-garnet could be investigated by using SXRF of Y and calculating solubility.

2. **Mineral diffusion into aqueous fluid:** One of the advantages of the SXRF technique is the in situ ability to investigate time resolved diffusion profiles. Spectra could be taken at smaller time increments to develop a diffusion profile during heating steps.

3. **2-D mapping to determine in situ partitioning:** The 2-D SXRF mapping allows for all phases present to analyzed in situ. The partition coefficient for the element under investigation (e.g., Y, Nb, Zr) of between the phases (fluid/crystal/melt) corresponds to the ratio between the concentrations of in each phase. This method has only been done in this dissertation and in Louvel et al. (2014), but is very promising to expand the database of partition coefficients.

APPENDICES

APPENDIX A

Appendix for chapter 3: The mobility of Nb in rutile-saturated NaCl- and NaF-bearing aqueous fluids from 1-6.5 GPa and 300-800°C

A.1 SXRF data of Nb-doped rutile

A.1.1 APS Beamline Information

The experiments require use an undulator source and diamond double crystal (111) monochromators, as the incident beam energy needed to be as high as possible (23 keV or 27 keV). The beamline 16-IDD had major upgrades during between 201108 and 201204 that allowed the incoming energy to be higher. The beam was focused with Kirkpatrick-Baez mirrors to be as small as possible, usually around 30x55 μm. The incident synchrotron beam is projected through the diamonds onto the sample and fluorescence is collected in a 170 back-scattering geometry using a Vortex-EX silicon drift detector $\sim$0.8 meters from the sample. Energy calibration of the multichannel analyzer will be performed with at least two sealed sources, usually Fe-55, Cd-109 and/or Co-57 .

Table A.1: Beamline Energy Calibration Information

Beamtime	Incoming beam energy	Calibration
201010	22.1 keV	Energy = 0.00671 * MCAChannel - 0.13477
201102	23.22 keV	Energy = 0.00671 * MCAChannel - 0.13477
201108	22.1 keV	Energy = 0.00765 * MCAChannel + 0.02300
201204	26.99 keV	Energy = 0.00735 * MCAChannel - 0.04907
201208	27.00 keV	Energy = 0.00735 * MCAChannel - 0.04907
201302	27.00 keV	Energy = 0.00765 * MCAChannel + 0.01560

A.1.2 Results from SXRF experiments containing $NaAlSi_3O_8$

Table A.2: Nb-rutile HDAC-SXRF experimental conditions and results

Experiment[a]	Fluid Type ($wt\%$)	Temperature (°C)	Pressure (GPa)	Fluid Density (g/cm^3)	ppm Nb in the fluid (error)[b]
20120401	$NaAlSi_3O_8$	300	2.7	1.30	374
20120401	$NaAlSi_3O_8$	400	3.3	1.33	600
20120401	$NaAlSi_3O_8$	500	2.7	1.25	634
20120402	$NaAlSi_3O_8$	300	2.4	1.27	2027
20120402	$NaAlSi_3O_8$	500	4.8	1.38	577
20120403	$NaAlSi_3O_8$	275	2.8	1.33	1048
20120403	$NaAlSi_3O_8$	380	5.8	1.50	1044
20120403	$NaAlSi_3O_8$	470	4.4	1.37	443
20120801	$NaAlSi_3O_8$	300	0.4	1.04	197
20120801	$NaAlSi_3O_8$	400	1.4	1.12	101
20120801	$NaAlSi_3O_8$	500	2.1	1.14	145
20120801	$NaAlSi_3O_8$	600	2.3	1.18	263

[a]Each experimental SXRF run allows us to measure the concentration of Nb in aqueous fluid at multiple P-T conditions. Rutile crystals are not recovered at each unique PT point; thus, partition coefficients are not reported.

A.1.3 Sample chamber images

An online camera was set-up inside the experimental hutch starting during beamtime 201108. The camera was used to take images of the sample chamber before and after SXRF data were collected.

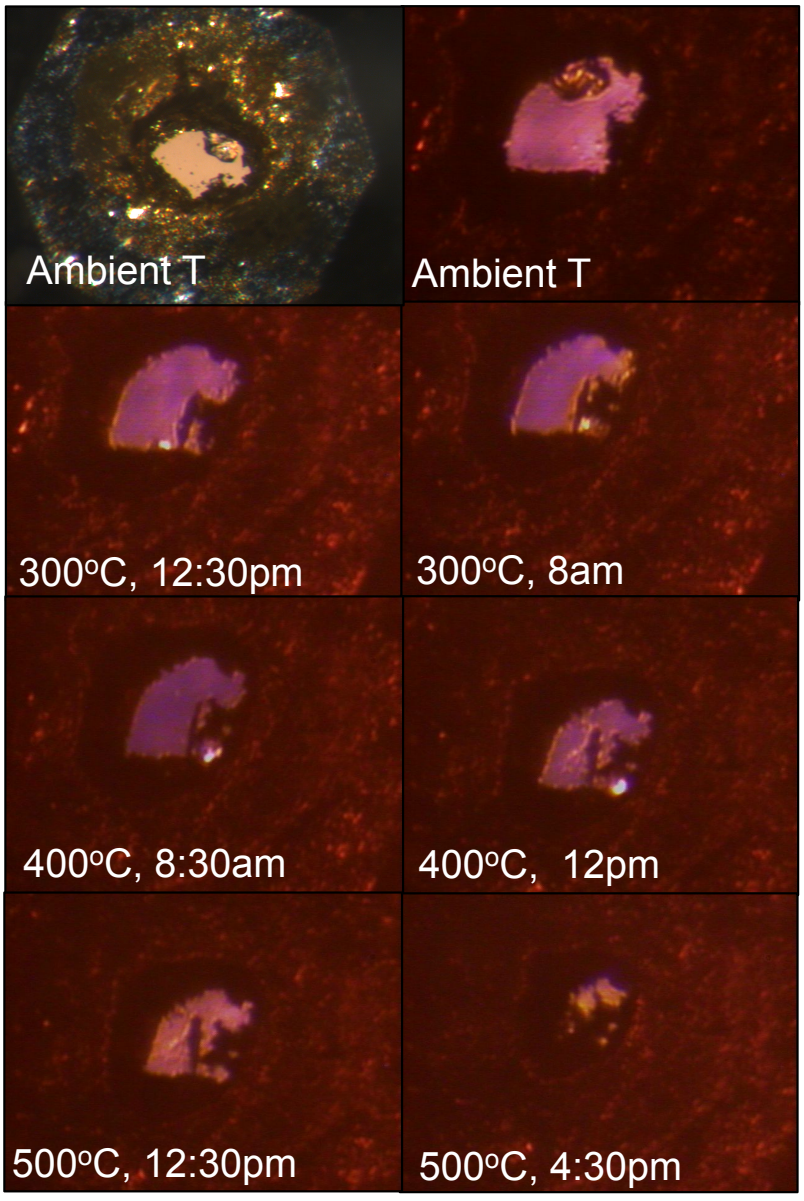

Figure A.1: Images of the sample chamber from run 20120802. A 4 wt% NaF aqueous fluid is loaded into a Au lined, Re gasket along with a Nb-doped rutile crystal.

A.2 BSE and EMPA of Nb-doped rutile data

A.2.1 BSE and EMPA experimental conditions

A beam current of 50 nA (calibration and analysis) and an accelerating voltage of 15 kV were used. The beam spot was approximately 5 μm in diameter. Counting times (30 s at the Nb and Ti peak) yielded detection limits for Nb, Ti, and Mo of approximately 330, 590 and 300 ppm, respectively. Standard ZAF techniques were used for the matrix corrections. The standards used included pure rutile, Nb_2O_5 and pure Mo metal. A different crystal and detector combination was used for each element: LIF for Ti; and LPET for Nb and Mo. Each crystal was imaged by using back scattered electrons (BSE), and an EMPA line traverse across the length of the sample was performed to evaluate chemical homogeneity. The distance between steps on starting crystals ranged between 10-100μm. Line scans on crystals containing a rim consisted of 2 μm steps, 50μm into the center of the crystal. On run crystals 20130522 and 20130527, 15 random points were selected.

A.2.2 Photo and BSE images, and EMPA data of Nb-Rutile run crystals

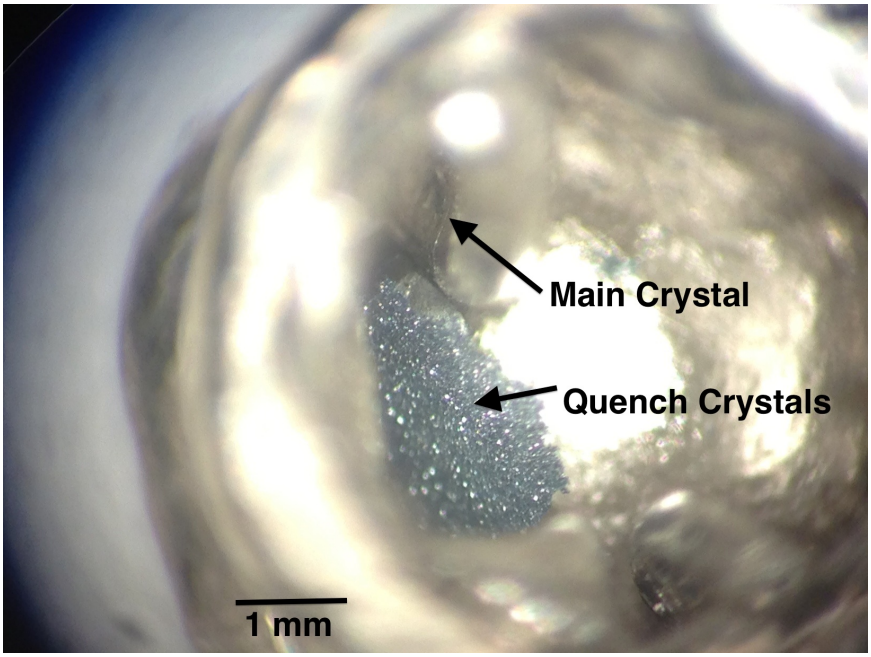

Figure A.2: Photographic image of run crystal from experiment 20130522. The crystals are still inside the Pt capsule.

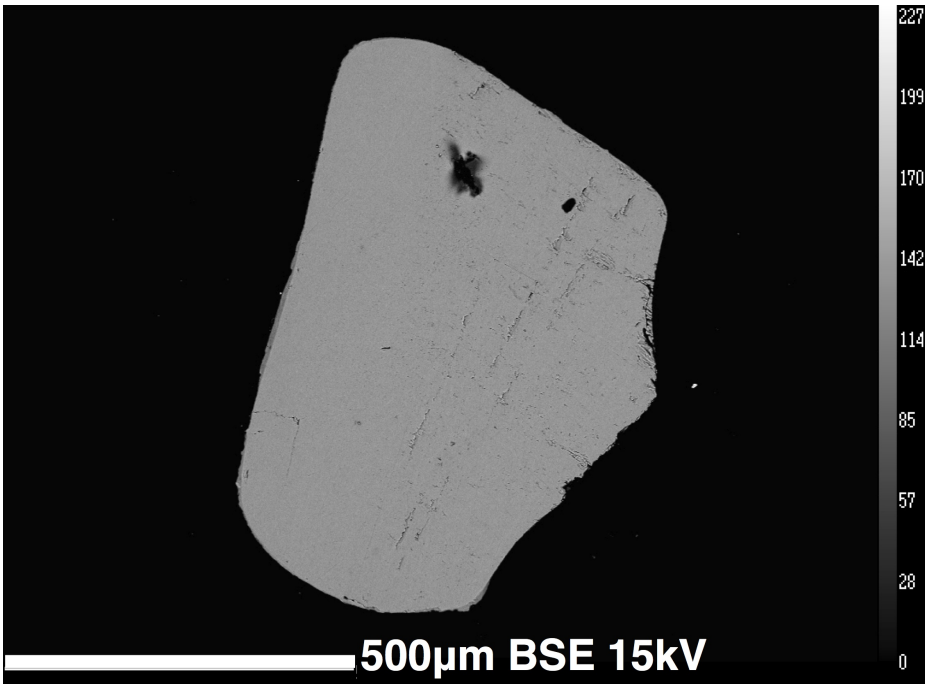

Figure A.3: BSE image of run crystal from experiment 20130522.

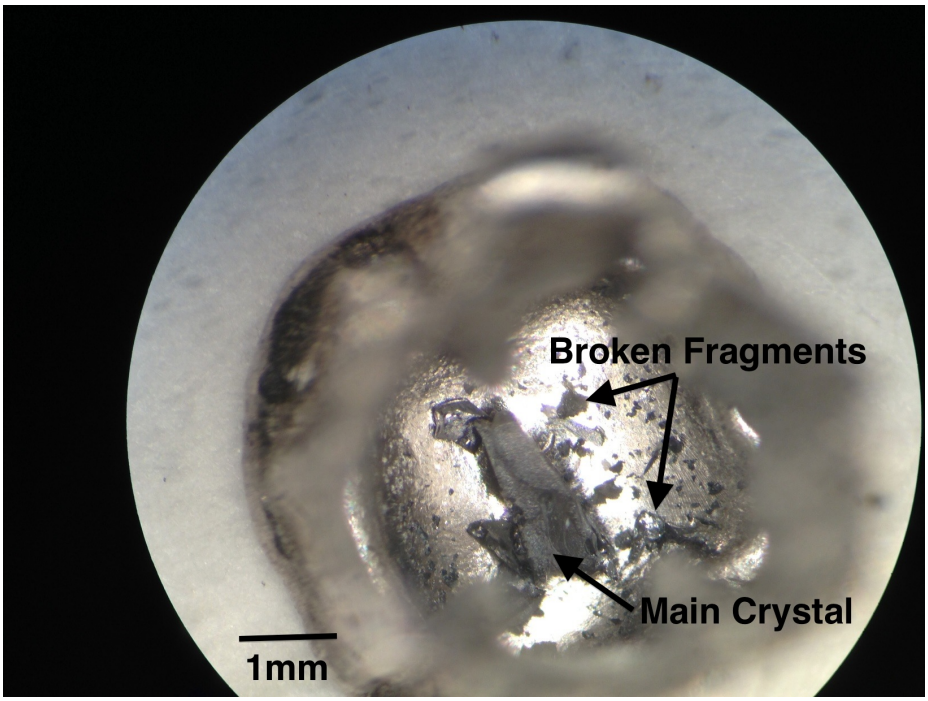

Figure A.4: Photographic image of run crystal from experiment 20130527. The crystals are still inside the Pt capsule.

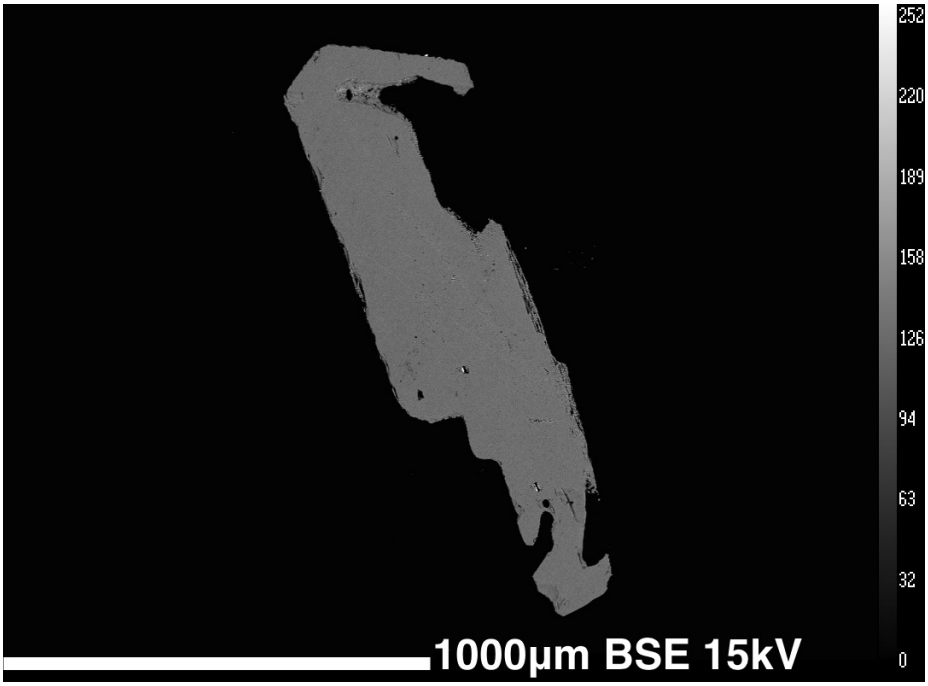

Figure A.5: BSE image of run crystal from experiment 20130527.

Table A.3: EMPA analysis of run crystal from experiment 20130522. Oxygen values are calculated.

DataSet/Point	Ti	Mo	Nb	O	Total	X	Y	Z	Mean Z
1 / 1 .	59.3471	0.0006	0.7284	39.8357	99.9118	11827	-21695	94	16.5421
2 / 1 .	59.3353	-0.0003	0.7674	39.8374	99.9399	11799	-21665	94	16.5553
3 / 1 .	59.3663	0.0135	0.5473	39.8081	99.7352	11808	-21693	94	16.4753
4 / 1 .	59.2872	-0.0048	0.803	39.8122	99.8976	11856	-21693	94	16.5554
5 / 1 .	59.3337	0.187	0.7169	39.917	100.1546	11795	-21784	94	16.6193
6 / 1 .	59.5292	0.0968	0.6777	39.9924	100.2961	11787	-21818	94	16.6144
7 / 1 .	59.1484	0.111	0.6588	39.7402	99.6583	11787	-21842	94	16.5086
8 / 1 .	59.5076	0.0954	0.6824	39.9784	100.2638	11787	-21842	94	16.6098
9 / 1 .	59.5897	0.1052	0.6957	40.0416	100.4321	12165	-22030	94	16.6425
10 / 1 .	59.2974	0.1585	0.7345	39.883	100.0733	12186	-22030	94	16.6037
11 / 1 .	59.1799	0.1834	0.7229	39.814	99.9002	12187	-22010	94	16.5781
12 / 1 .	58.9129	0.1122	0.7294	39.6017	99.3562	12044	-22015	94	16.4752
13 / 1 .	59.4324	0.1005	0.6433	39.9206	100.0968	12003	-22008	94	16.5747
14 / 1 .	59.3233	0.0105	0.6987	39.817	99.8494	12007	-22082	94	16.5273
15 / 1 .	59.3453	0.1509	0.6969	39.9015	100.0945	12303	-22091	94	16.597

Table A.4: EMPA analysis of run crystal from experiment 20130527. Oxygen values are calculated.

DataSet/Point	Ti	Mo	Nb	O	Total	X	Y	Z	Mean Z
16 / 1 .	58.8832	0.0719	1.0101	39.6342	99.5994	13241	-21489	94	16.5694
17 / 1 .	59.6453	0.0753	1.0057	40.1439	100.8701	13186	-21489	94	16.7774
18 / 1 .	58.8504	0.0712	1.0516	39.6226	99.5957	13158	-21480	94	16.5779
19 / 1 .	59.4097	0.0275	1.0006	39.9612	100.399	13054	-21480	94	16.6888
20 / 1 .	59.3502	-0.0088	1.0364	39.9125	100.2903	13032	-21092	94	16.6713
21 / 1 .	59.365	-0.0012	1.0396	39.9271	100.3304	13005	-21092	94	16.6802
22 / 1 .	59.0688	-0.0024	1.0273	39.7254	99.819	12990	-21108	94	16.5933
23 / 1 .	59.639	-0.015	1.0474	40.1052	100.7766	12967	-21108	94	16.7521
24 / 1 .	59.3261	0.0022	1.0594	39.9079	100.2956	13382	-21187	94	16.6797
25 / 1 .	59.109	-0.0062	1.0692	39.7612	99.9333	13372	-21228	94	16.6207
26 / 1 .	59.0756	-0.0057	1.1742	39.7663	100.0104	13372	-21254	94	16.657
27 / 1 .	59.4075	0.0018	1.035	39.9558	100.4001	13372	-21286	94	16.6912
28 / 1 .	59.5446	-0.0102	1.0267	40.0393	100.6004	13421	-21334	94	16.7196
29 / 1 .	58.9368	0.0065	1.0534	39.6485	99.6452	13407	-21340	94	16.5726
30 / 1 .	59.3575	0.0037	0.9834	39.91	100.2546	13401	-21418	94	16.656

A.2.3 BSE and EMPA of example starting crystals

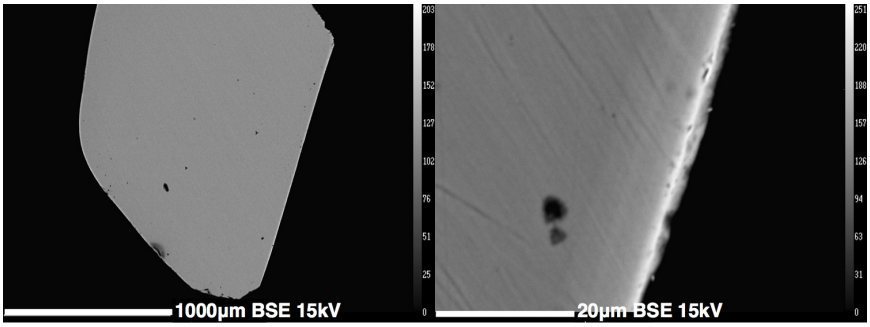

Figure A.6: BSE image of example starting crystal 1.

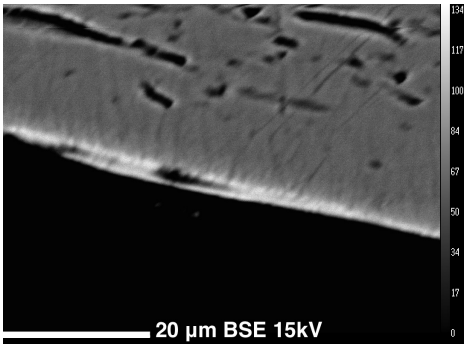

Figure A.7: BSE image of example starting crystal 2.

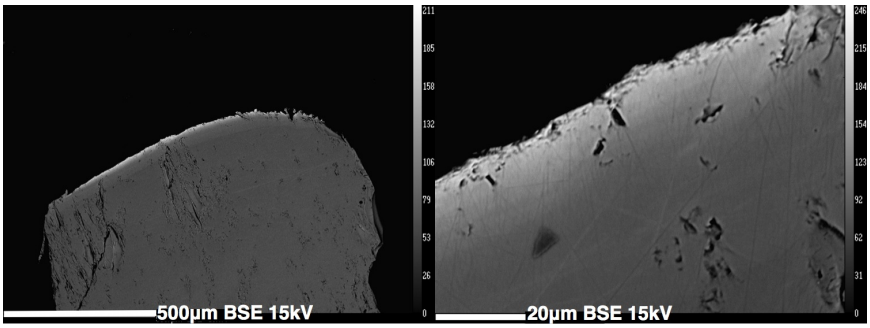

Figure A.8: BSE image of example starting crystal 3.

Table A.5: EMPA analysis of example starting crystals

DataSet/Point	Ti	Mo	Nb	O	Total	X	Y	Z	Distance (μm)	Mean Z
Crystal 1:	**line scan,**	**40μm step**								
3 / 1 .	59.4973	0	1.0233	40.0116	100.5316	9297	-27490	171	0	16.7096
3 / 2 .	59.1988	0	0.9867	39.8021	99.9859	9330.1	-27466.6	171	40.52	16.6117
3 / 3 .	59.5034	0.005	0.9604	40.0022	100.4709	9363.2	-27443.3	171	81.04	16.6868
3 / 4 .	58.8637	0	0.9138	39.5599	99.3366	9396.3	-27419.9	171	121.57	16.4891
3 / 5 .	59.4088	0	0.9481	39.9319	100.2859	9429.4	-27396.5	171	162.09	16.652
3 / 6 .	59.4317	0.0063	0.9324	39.9477	100.3182	9462.5	-27373.2	171	202.61	16.6557
3 / 7 .	59.0108	0.0091	1.0181	39.6901	99.7281	9495.6	-27349.8	171	243.13	16.5789
3 / 8 .	59.202	0	1.0415	39.816	100.053	9528.7	-27326.4	171	283.65	16.634
3 / 9 .	58.9627	0.0076	1.0062	39.6541	99.6306	9561.8	-27303.1	171	324.18	16.5599
3 / 10 .	59.2132	0	1.0107	39.8148	100.0308	9594.9	-27279.7	171	364.7	16.6231
3 / 11 .	58.963	0	0.976	39.6386	99.5695	9628.1	-27256.3	171	405.22	16.5397
3 / 12 .	59.2987	0.0062	0.975	39.8698	100.1498	9661.2	-27233	171	445.74	16.6377
3 / 13 .	59.4689	0	0.975	39.9742	100.4055	9694.3	-27209.6	171	486.27	16.6756
3 / 14 .	59.2392	0.0042	0.8504	39.7969	99.8907	9727.4	-27186.2	171	526.79	16.5668
3 / 15 .	59.6015	0	0.8349	40.0306	100.4627	9760.5	-27162.8	171	567.31	16.6553
3 / 16 .	59.2811	0	0.864	39.8222	99.9592	9793.6	-27139.5	171	607.83	16.5784
3 / 17 .	59.882	0	0.8616	40.2251	100.9647	9826.7	-27116.1	171	648.35	16.7436
3 / 18 .	59.5989	0	0.8981	40.0474	100.5443	9859.8	-27092.7	171	688.88	16.6838
3 / 19 .	59.2336	0	0.9802	39.8233	100.0344	9892.9	-27069.4	171	729.4	16.618
3 / 20 .	59.4412	0	0.9707	39.96	100.3703	9926	-27046	171	769.92	16.6712
Crystal 2:	**rim scan,**	**2μm step**								
4 / 1 .	58.9397	0.009	0.9854	39.6341	99.5681	14015	-25942	171	0	16.5453
4 / 2 .	58.9186	0	1.0178	39.6139	99.5304	14015	-25939.9	171	2.08	16.5401
4 / 3 .	59.1501	0.0056	1.0298	39.7844	99.9699	14015	-25937.8	171	4.17	16.6204
4 / 4 .	59.1529	0	0.9873	39.766	99.8933	14015	-25935.8	171	6.25	16.5943
4 / 5 .	59.1325	0	1.0123	39.763	99.9032	14015	-25933.7	171	8.33	16.6033

Table A.5: EMPA analysis of example starting crystals continued

DataSet/Point	Ti	Mo	Nb	O	Total	X	Y	Z	Distance (μm)	Mean Z
4 / 6 .	58.9195	0	0.9666	39.6098	99.4931	14015	-25931.6	171	10.42	16.5262
4 / 7 .	59.091	0	1.0175	39.7316	99.8255	14015	-25929.5	171	12.5	16.5896
4 / 8 .	58.7729	0	1.0113	39.5158	99.282	14015	-25927.4	171	14.58	16.4984
4 / 9 .	58.7618	0.0094	0.9773	39.5133	99.2618	14015	-25925.3	171	16.67	16.4933
4 / 10 .	58.5027	0	1.0049	39.3412	98.8459	14015	-25923.3	171	18.75	16.4287
4 / 11 .	59.3073	0	0.9708	39.8704	100.1467	14015	-25921.2	171	20.83	16.6345
4 / 12 .	58.9474	0	0.9692	39.6293	99.5434	14015	-25919.1	171	22.92	16.5351
4 / 13 .	58.6902	0	0.9841	39.4624	99.1364	14015	-25917	171	25	16.4722
4 / 14 .	58.6237	0	0.9594	39.4018	98.9651	14015	-25914.9	171	27.08	16.4344
4 / 15 .	58.975	0	0.9886	39.6534	99.6157	14015	-25912.8	171	29.17	16.5516
4 / 16 .	59.1713	0.0063	0.9529	39.779	99.9095	14015	-25910.8	171	31.25	16.5933
4 / 17 .	58.1482	0	0.8912	39.0703	98.0975	14015	-25908.7	171	33.33	16.2785
4 / 18 .	58.594	0	0.9756	39.3869	98.9382	14015	-25906.6	171	35.42	16.434
4 / 19 .	58.5071	0	0.9458	39.328	98.7761	14015	-25904.5	171	37.5	16.4036
4 / 20 .	57.2329	0	0.8691	38.4513	96.5374	14015	-25902.4	171	39.58	16.017
4 / 21 .	58.8158	0.0013	0.9529	39.5391	99.3091	14015	-25900.3	171	41.67	16.4938
4 / 22 .	58.8346	0	1.0133	39.56	99.3946	14015	-25898.3	171	43.75	16.5183
4 / 23 .	58.8741	0	1.0379	39.5915	99.488	14015	-25896.2	171	45.83	16.5386
4 / 24 .	59.0431	0	0.9948	39.6966	99.7257	14015	-25894.1	171	47.92	16.5694
4 / 25 .	58.7373	0	1.0486	39.5055	99.2811	14015	-25892	171	50	16.5082
Crystal 2:	**line scan,**	**98μm step**								
5 / 1 .	58.9366	0	1.1071	39.6545	99.6893	14329	-25863	171	0	16.5886
5 / 2 .	58.802	0	1.0412	39.5481	99.3835	14236.4	-25832.4	171	97.51	16.5239
5 / 3 .	58.5309	0.0135	1.0479	39.3793	98.9716	14143.8	-25801.7	171	195.03	16.4624
5 / 4 .	59.1202	0.0179	1.0368	39.7724	99.9474	14051.3	-25771.1	171	292.55	16.6209
5 / 5 .	58.6334	0	1.0021	39.4258	99.0543	13958.7	-25740.5	171	390.06	16.4613
5 / 6 .	59.1457	0.0057	0.9963	39.7728	99.9205	13866.1	-25709.8	171	487.57	16.6048

Table A.5: EMPA analysis of example starting crystals continued

DataSet/Point	Ti	Mo	Nb	O	Total	X	Y	Z	Distance (μm)	Mean Z
5 / 7 .	59.352	0	0.9823	39.9034	100.2362	13773.5	-25679.2	171	585.09	16.6518
5 / 8 .	58.9407	0	0.98	39.626	99.541	13681	-25648.6	171	682.6	16.5364
5 / 9 .	58.7954	0.0116	1.0034	39.5436	99.3539	13588.4	-25618	171	780.12	16.5147
5 / 10 .	58.1938	0.0268	1.0044	39.1496	98.3746	13495.8	-25587.3	171	877.63	16.3577
5 / 11 .	58.6285	0.0068	0.9719	39.4215	99.0287	13403.2	-25556.7	171	975.15	16.4533
5 / 12 .	58.8336	0.0135	0.9792	39.5639	99.3902	13310.6	-25526.1	171	1072.66	16.5157
5 / 13 .	58.9019	0.0111	1.0034	39.6146	99.531	13218.1	-25495.4	171	1170.18	16.5437
5 / 14 .	58.7894	0.0172	1.0358	39.5508	99.3932	13125.5	-25464.8	171	1267.69	16.5297
5 / 15 .	58.8674	0.0086	0.9997	39.5893	99.4651	13032.9	-25434.2	171	1365.21	16.5315
5 / 16 .	58.7143	0.029	1.0244	39.5036	99.2713	12940.3	-25403.5	171	1462.72	16.5096
5 / 17 .	57.5777	0.0294	0.9595	38.7277	97.2942	12847.7	-25372.9	171	1560.24	16.171
5 / 18 .	58.7797	0.0273	1.184	39.5876	99.5786	12755.2	-25342.3	171	1657.75	16.5954
5 / 19 .	59.1733	0.0144	1.242	39.8591	100.2887	12662.6	-25311.6	171	1755.27	16.7221
5 / 20 .	59.0986	0	1.2271	39.7946	100.1131	12570	-25281	171	1852.78	16.6854
Crystal 3:	**rim scan,**	**2μm step**								
6 / 1 .	53.1274	2.4271	5.0507	38.0111	98.6162	17631	-24797	177	0	17.8191
6 / 2 .	53.6579	1.8874	4.9666	38.0738	98.5857	17631	-24799.1	177	2.08	17.6797
6 / 3 .	54.3294	1.2834	4.6205	38.1308	98.3641	17631	-24801.2	177	4.17	17.4364
6 / 4 .	55.0096	0.6584	4.4626	38.2317	98.3623	17631	-24803.3	177	6.25	17.2669
6 / 5 .	55.4586	0.5338	4.1003	38.3758	98.4685	17631	-24805.3	177	8.33	17.1763
6 / 6 .	55.9858	0.1886	3.8473	38.4899	98.5116	17631	-24807.4	177	10.42	17.0527
6 / 7 .	56.2505	0.1428	3.7573	38.6205	98.7711	17631	-24809.5	177	12.5	17.0652
6 / 8 .	56.5644	0.1131	3.6462	38.7867	99.1103	17631	-24811.6	177	14.58	17.0895
6 / 9 .	56.3107	0.1888	3.8418	38.7056	99.0469	17631	-24813.7	177	16.67	17.1393
6 / 10 .	56.0308	0.1863	3.8739	38.5256	98.6166	17631	-24815.8	177	18.75	17.0754
6 / 11 .	56.2959	0.1204	3.5534	38.587	98.5566	17631	-24817.8	177	20.83	16.9795
6 / 12 .	57.1188	0.0211	3.0685	38.9618	99.1701	17631	-24819.9	177	22.92	16.95

Table A.5: EMPA analysis of example starting crystals continued

DataSet/Point	Ti	Mo	Nb	O	Total	X	Y	Z	Distance (μm)	Mean Z
6 / 13 .	56.7482	0.0141	2.9903	38.6904	98.4429	17631	-24822	177	25	16.8117
6 / 14 .	56.6536	0.0036	2.9148	38.6025	98.1745	17631	-24824.1	177	27.08	16.7486
6 / 15 .	57.1093	0.0056	2.6814	38.8477	98.6441	17631	-24826.2	177	29.17	16.7736
6 / 16 .	57.4385	0.0066	2.5454	39.0329	99.0234	17631	-24828.3	177	31.25	16.8055
6 / 17 .	57.432	0.0031	2.4284	38.9966	98.86	17631	-24830.3	177	33.33	16.7517
6 / 18 .	57.3453	0.0151	2.3484	38.9241	98.6328	17631	-24832.4	177	35.42	16.6991
6 / 19 .	57.2119	0.0176	2.2244	38.8042	98.258	17631	-24834.5	177	37.5	16.6103
6 / 20 .	57.9767	-0.0016	2.0677	39.265	99.3077	17631	-24836.6	177	39.58	16.7432
6 / 21 .	58.1679	0.0014	1.6891	39.2965	99.1549	17631	-24838.7	177	41.67	16.6338
6 / 22 .	58.6178	0.0419	1.0087	39.4415	99.1098	17631	-24840.8	177	43.75	16.4824
6 / 23 .	58.3879	0.0929	0.8595	39.2749	98.6152	17631	-24842.8	177	45.83	16.3787
6 / 24 .	58.4261	0.0668	0.8505	39.285	98.6284	17631	-24844.9	177	47.92	16.3733
6 / 25 .	58.4415	0.0823	0.8625	39.3062	98.6925	17631	-24847	177	50	16.3898
Crystal 3:	**line scan,**	**74μm step**								
7 / 1 .	58.2809	0.0449	0.9146	39.1936	98.4341	17845	-24809	177	0	16.3511
7 / 2 .	58.1837	0.0908	0.8489	39.1346	98.2579	17810.6	-24874.9	177	74.32	16.3173
7 / 3 .	57.883	0.0685	0.8197	38.9151	97.6863	17776.3	-24940.8	177	148.64	16.2123
7 / 4 .	57.8697	0.071	0.8688	38.9201	97.7297	17741.9	-25006.7	177	222.96	16.231
7 / 5 .	58.1835	0.0922	0.8042	39.1237	98.2036	17707.5	-25072.6	177	297.28	16.2987
7 / 6 .	57.7139	0.0812	0.8221	38.8091	97.4264	17673.2	-25138.5	177	371.6	16.173
7 / 7 .	58.0997	0.0603	0.8686	39.0684	98.0969	17638.8	-25204.4	177	445.91	16.2888
7 / 8 .	58.0428	0.0707	0.8457	39.0297	97.9888	17604.4	-25270.3	177	520.23	16.2682
7 / 9 .	58.2659	0.0486	0.7438	39.1413	98.1996	17570.1	-25336.2	177	594.55	16.2752
7 / 10 .	58.3811	0.0559	0.7863	39.2329	98.4562	17535.7	-25402.1	177	668.87	16.3283
7 / 11 .	57.8911	0.0704	0.7798	38.9112	97.6525	17501.3	-25468	177	743.19	16.1982
7 / 12 .	58.1019	0.0634	0.7022	39.0284	97.8958	17467	-25533.8	177	817.51	16.2192
7 / 13 .	58.0391	0.0694	0.8086	39.017	97.9341	17432.6	-25599.7	177	891.83	16.2507

Table A.5: EMPA analysis of example starting crystals continued

DataSet/Point	Ti	Mo	Nb	O	Total	X	Y	Z	Distance (μm)	Mean Z
7 / 14 .	58.1276	0.0498	0.8415	39.0748	98.0938	17398.2	-25665.6	177	966.15	16.28
7 / 15 .	57.4871	0.0663	0.7062	38.6202	96.8799	17363.8	-25731.5	177	1040.46	16.0542
7 / 16 .	57.7131	0.0423	0.7413	38.7683	97.265	17329.5	-25797.4	177	1114.78	16.12
7 / 17 .	58.2048	0.0865	0.8354	39.1431	98.2698	17295.1	-25863.3	177	1189.1	16.3153
7 / 18 .	57.519	0.057	0.9553	38.7012	97.2323	17260.7	-25929.2	177	1263.42	16.1658
7 / 19 .	57.7665	0.0317	0.8602	38.8293	97.4878	17226.4	-25995.1	177	1337.74	16.181
7 / 20 .	57.4918	0	0.9382	38.6501	97.08	17192	-26061	177	1412.06	16.1248

APPENDIX B

Appendix for chapter 4: Rutile solubility in aqueous fluid based on SXRF measurements of Zr in Zr-doped rutile-saturated NaF-, NaCl-, KCl-, and mixed NaF-NaCl- bearing aqueous fluids

B.1 SXRF data of Zr-doped rutile

B.1.1 APS beamline information

The synchrotron X-ray fluorescence (SXRF) experiments were performed at undulator beamline 16-IDD (HPCAT) at the Advanced Photon Source (APS) synchrotron facility at Argonne National Laboratory. The incident beam energy was 27 keV. The beam was focused to a spot size of 25x50 μm full-width at half maximum (FWHM) by using a pair of Kirkpatrick-Baez mirrors. A 100 μm round pinhole was used before the HDAC to reduce the tails of the incident beam, which contained a flux of 1.14x10^{12} photons/s. The incident beam was projected into the sample chamber through the diamonds of the HDAC. The fluorescence from the sample was collected in a 170° backscattering geometry by using a Vortex-EX silicon drift detector that

was positioned ∼0.8 m from the sample. To reduce the background, a pair of large collimating slits was placed before the detector. The energy channels of the multi-channel analyzer were calibrated with ^{55}Fe, ^{57}Co, and ^{109}Cd radioactive sources. The incident beam energy and energy channel calibration are listed in Table B.1 The position and aperture of the detector was optimized by using the SXRF peak of pure Zr metal. There was no Zr contamination from any component of the HDAC, which was confirmed by SXRF analyses of an empty cell. The Zr-rutile crystal position was determined visually by using an online optical microscope and confirmed by mapping the HDAC sample chamber by using SXRF (see B.1.2) Pressure was determined at the beginning of each HDAC run, and monitored throughout the run by collecting XRD patterns of Au from a MAR 165 CCD detector placed in the forward scattering direction.

Table B.1: Beamline Energy Calibration Information

Beamtime	Incoming beam energy	Calibration
201310	27.00 keV	Energy = 0.00909 * MCAChannel + 0.03057
201401	27.00 keV	Energy = 0.00832 * MCAChannel + 0.01439

B.1.2 Sample chamber images

The images below are taken from a microscope mounted on the beamline (Figure 2.1a) of the sample chamber (Figure 2.1b) inside the hydrothermal diamond anvil cell (HDAC) during heating. All HDACs were equipped with two opposing 800 μm culet diamonds. Molybdenum wires, coiled around a tungsten carbide seat that supported each diamond anvil, provided resistive heating. Two K-type (NiCr-NiAl) thermocouples, one on each diamond, were used to measure temperature. The HDAC was heated resistively by using variable transformers that facilitated flexible heating rates and allowed us to maintain temperature to ± 5°C. A 1% H_2-Ar gas mixture flowed constantly through the HDAC during the measurements to prevent corrosion of the diamonds and the heaters.

A rhenium gasket was pre-indented to a thickness of $\sim$120 μm and a hole of $\sim$600 μm diameter was drilled. The hole was filled with Au powder, compressed until the Au turned into a metallic solid and then a second 200-400 μm diameter hole was drilled. A single irregularly shaped Zr-rutile crystal measuring approximately 40x40x20 μm, as determined by using an optical microscope, was loaded into the sample chamber for each experimental run. Deionized H_2O containing either 2, 3, 4 wt% NaF, 30 wt% NaCl, 30 wt% KCl, or mixed 10 wt% NaCl + 2 wt% NaF, was then added by using a micro syringe and the HDAC was immediately sealed and pressurized to $\sim$ 0.5 GPa.

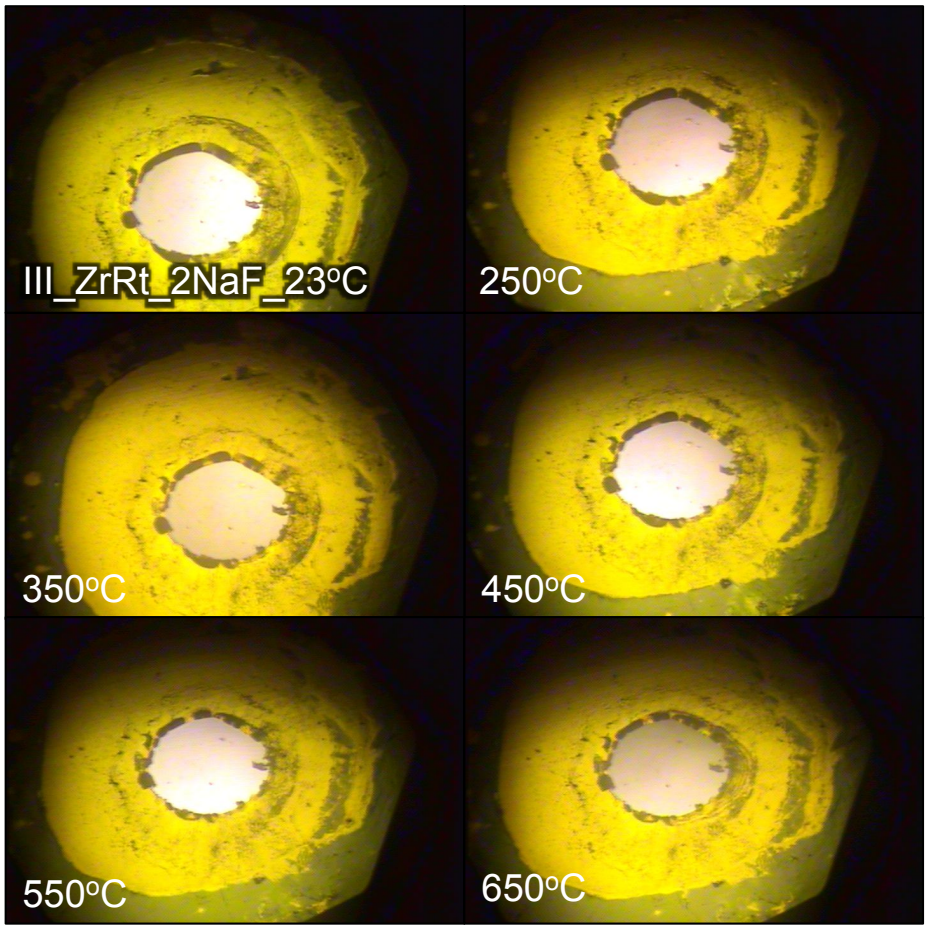

Figure B.1: Sample chamber images of SXRF run 20131003. A Zr-doped rutile crystal is loaded with a 2 wt% NaF aqueous fluid in a Au lined, Re gasket. The sample chamber measures: hole diameter=250 μm, gasket hickness=120μm.

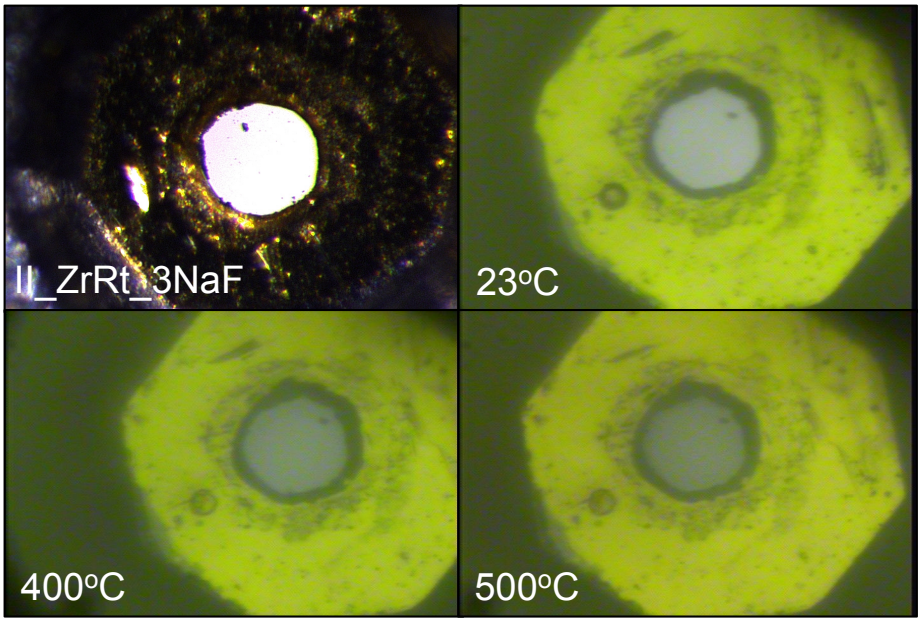

Figure B.2: Sample chamber images of SXRF run 20140102. A Zr-doped rutile crystal is loaded with a 3 wt% NaF aqueous fluid in a Au lined, Re gasket. The sample chamber measures: hole diameter=215μm, gasket hickness=140μm.

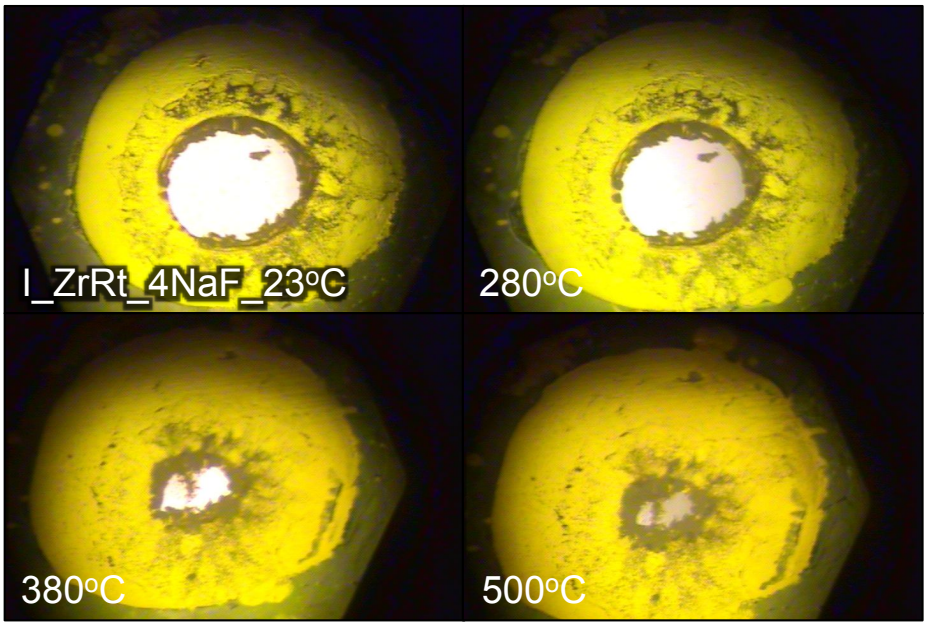

Figure B.3: Sample chamber images of SXRF run 20131001. A Zr-doped rutile crystal is loaded with a 4 wt% NaF aqueous fluid in a Au lined, Re gasket. The sample chamber measures: hole diameter=270μm, gasket thickness=150μm.

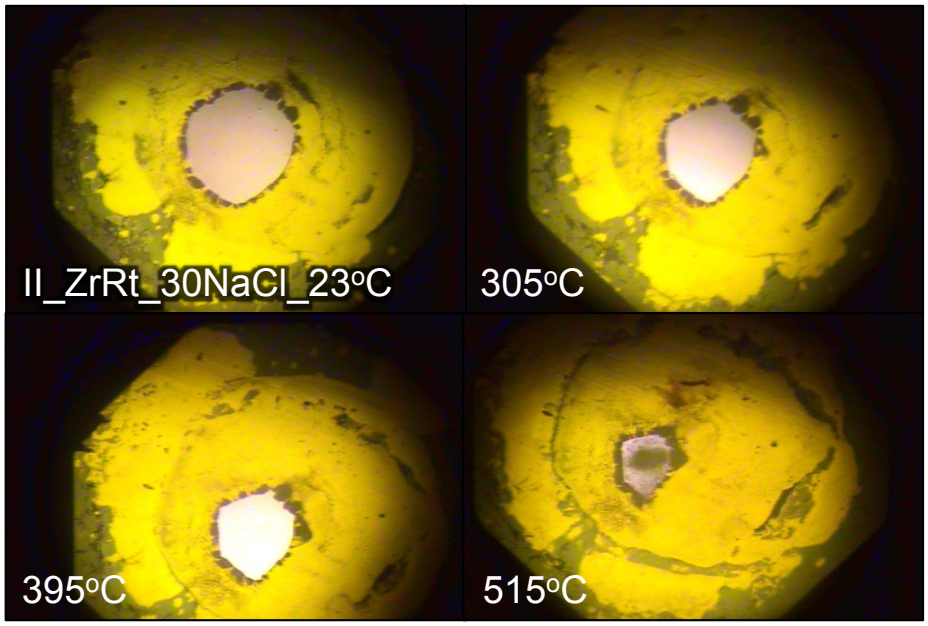

Figure B.4: Sample chamber images of SXRF run 20131002. A Zr-doped rutile crystal is loaded with a 30 wt% NaCl aqueous fluid in a Au lined, Re gasket. The sample chamber measures: hole diameter=200μm, gasket thickness=150μm.

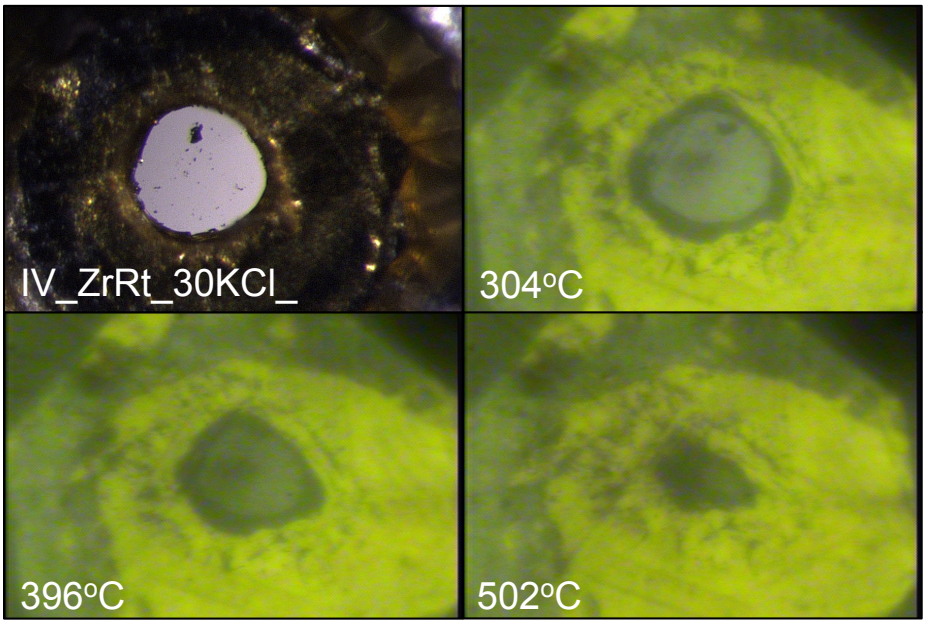

Figure B.5: Sample chamber images of SXRF run 20140104. A Zr-doped rutile crystal is loaded with a 30 wt% KCl aqueous fluid in a Au lined, Re gasket. The sample chamber measures: hole diameter=230μm, gasket thickness=165μm.

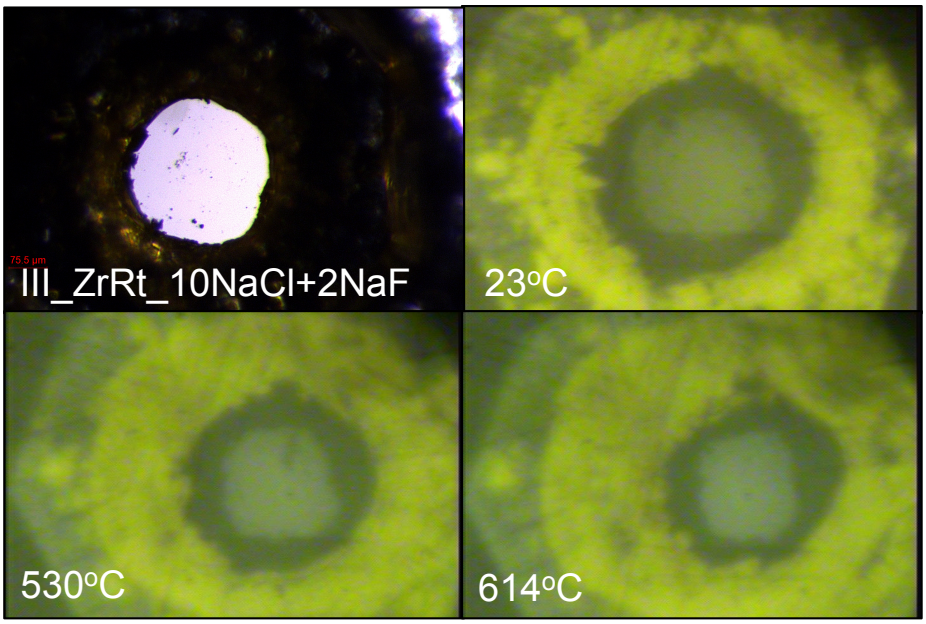

Figure B.6: Sample chamber images of SXRF run 20140103. A Zr-doped rutile crystal is loaded with a 10 wt% NaCl + 2 wt% NaF aqueous fluid in a Au lined, Re gasket. The sample chamber measures: hole diameter=250 μm, gasket thickness=165μm.

B.1.3 EMPA data of SXRF starting crystal

Each starting crystal was imaged by using back-scattered electrons (BSE), and most of the starting crystals displayed slight zoning (Figure 4.1). The concentrations of Zr, Ti and Mo, which was used as a flux during crystal growth, in the starting crystals were quantified by using wavelength dispersive spectroscopy on a Cameca SX100 electron probe microanalyzer (EPMA). A beam current of 50 nA (calibration and analysis) and an accelerating voltage of 15 kV were used. Collimators were used to reduce peak interferences and to maximize peak-to-background ratios. Counting times (30 s at the peak) yielded detection limits for Zr, Ti, and Mo of approximately 580, 290 and 465 ppm, respectively. Standard ZAF techniques were used for the matrix corrections. The standards used included pure natural rutile, zircon and pure Mo metal. A different crystal and detector combination was used for each element: LIF for Ti and LPET for Zr and Mo. An EMPA line traverse, using a 5 μm beam with analyses spaced every 25 μm, was performed across the length of each crystal to evaluate chemical homogeneity.

Table B.2: EMPA analysis of the starting crystal from SXRF experiments. The linescan step-size for dataset 5, across the length of the crystal was 25 μm. The linescan step-size for dataset 6, from the rim to 50 μm into the center of the crystal was 2 μm.

DataSet/Point	TiO_2	MoO_3	ZrO_2	Total	X	Y	Z	Distance (μm)	Mean Z
5 / 1 .	95.8994	0.0356	4.5678	100.5028	-12422	-25409	37	0	17.1792
5 / 2 .	95.4687	0.0809	4.3998	99.9494	-12397.4	-25409	37	24.64	17.0693
5 / 3 .	96.0501	0.0524	4.4825	100.585	-12372.7	-25409	37	49.29	17.1821
5 / 4 .	95.5216	0.0712	4.5243	100.1172	-12348.1	-25409	37	73.93	17.1145
5 / 5 .	95.9743	0.0502	4.4565	100.4809	-12323.4	-25409	37	98.57	17.1607
5 / 6 .	96.2632	0.0594	4.5272	100.8497	-12298.8	-25409	37	123.21	17.2333
5 / 7 .	96.1269	0.0659	4.4931	100.6859	-12274.1	-25409	37	147.86	17.2022
5 / 8 .	95.5485	0.0615	4.4104	100.0204	-12249.5	-25409	37	172.5	17.0798
5 / 9 .	96.1916	0.0443	4.4392	100.6751	-12224.9	-25409	37	197.14	17.189
5 / 10 .	95.5746	0.0638	4.4591	100.0975	-12200.2	-25409	37	221.79	17.1002
5 / 11 .	96.167	0.0564	4.391	100.6144	-12175.6	-25409	37	246.43	17.1734
5 / 12 .	96.2069	0.0603	4.4026	100.6699	-12150.9	-25409	37	271.07	17.1849
5 / 13 .	95.5137	0.0614	4.5227	100.0977	-12126.3	-25409	37	295.71	17.1096
5 / 14 .	96.3095	0.1035	4.424	100.8371	-12101.6	-25409	37	320.36	17.2217
5 / 15 .	96.3478	0.0499	4.556	100.9536	-12077	-25409	37	345	17.2534
6 / 1 .	95.8442	0.0846	4.6633	100.5921	-12488	-25409	37	0	17.2155
6 / 2 .	96.1283	0.0825	4.5232	100.7339	-12485.9	-25409	37	2.08	17.217
6 / 3 .	95.5808	0.0707	4.6968	100.3484	-12483.8	-25409	37	4.17	17.1787
6 / 4 .	95.8799	0.0677	4.6928	100.6404	-12481.8	-25409	37	6.25	17.2255
6 / 5 .	95.6044	0.0906	4.6213	100.3163	-12479.7	-25409	37	8.33	17.1647
6 / 6 .	95.6259	0.0881	4.5674	100.2813	-12477.6	-25409	37	10.42	17.1503
6 / 7 .	95.4518	0.1054	4.508	100.0652	-12475.5	-25409	37	12.5	17.1083
6 / 8 .	95.3336	0.111	4.4648	99.9094	-12473.4	-25409	37	14.58	17.077
6 / 9 .	94.8029	0.0819	4.4511	99.3359	-12471.3	-25409	37	16.67	16.9767
6 / 10 .	95.8628	0.0759	4.5439	100.4826	-12469.3	-25409	37	18.75	17.178

Table B.2: EMPA analysis of starting crystal from SXRF experiments continued

DataSet/Point	TiO_2	MoO_3	ZrO_2	Total	X	Y	Z	Distance (μm)	Mean Z
6 / 11 .	95.0754	0.096	4.6339	99.8052	-12467.2	-25409	37	20.83	17.0836
6 / 12 .	95.6418	0.0874	4.4617	100.1909	-12465.1	-25409	37	22.92	17.1193
6 / 13 .	95.758	0.0859	4.4265	100.2703	-12463	-25409	37	25	17.1267
6 / 14 .	95.9921	0.0999	4.5383	100.6303	-12460.9	-25409	37	27.08	17.2048
6 / 15 .	95.7738	0.0898	4.485	100.3486	-12458.8	-25409	37	29.17	17.149
6 / 16 .	95.7081	0.1031	4.4123	100.2235	-12456.8	-25409	37	31.25	17.1193
6 / 17 .	95.7556	0.103	4.4254	100.284	-12454.7	-25409	37	33.33	17.1312
6 / 18 .	96.0533	0.0831	4.5335	100.6699	-12452.6	-25409	37	35.42	17.2081
6 / 19 .	95.4774	0.1065	4.4593	100.0433	-12450.5	-25409	37	37.5	17.0974
6 / 20 .	95.5961	0.1256	4.418	100.1397	-12448.4	-25409	37	39.58	17.1097
6 / 21 .	95.6486	0.1055	4.3535	100.1076	-12446.3	-25409	37	41.67	17.0917
6 / 22 .	95.5508	0.1103	4.4416	100.1027	-12444.3	-25409	37	43.75	17.105
6 / 23 .	95.6229	0.1204	4.5162	100.2596	-12442.2	-25409	37	45.83	17.1436
6 / 24 .	95.8962	0.1154	4.4995	100.511	-12440.1	-25409	37	47.92	17.1815
6 / 25 .	94.9915	0.1298	4.3888	99.5101	-12438	-25409	37	50	17.0026

B.2 Data from piston cylinder mass loss experiments of Zr-doped rutile

B.2.1 Methods

The mass loss experiments were conducted in a piston-cylinder apparatus at the University of Michigan (Figure B.7). Run conditions are provided in Table B.3. Starting crystals were mounted in epoxy, polished and EMPA performed to determine the Zr concentrations (Tables B.4, B.6, B.8, B.10, B.12) Each starting crystal was weighed four times by using a Mettler XP26 DeltaRange balance, and the values averaged for accuracy, before being loaded into the capsule. The experimental capsule contained a single crystal of Zr-bearing rutile and 40 μg fluid (containing either 3 or 4 wt% NaF) in a 5 mm OD platinum capsule. The capsule design was made by cutting a ∼6.5-7 mm length piece of Pt or Au tubing and welding a circular disk lid onto the bottom and top (after it was loaded). The capsule was weighed before and after welding to ensure no fluid loss. The capsule was enclosed in crushable MgO as the inner pressure medium, with a graphite heater outside and a $BaCO_3$ cell as the outer pressure medium (Figure B.8). The charge was heated and compressed in alternating increments to minimize compression and expansion of the capsule relative to other sample assembly parts by following a P-T path of constant fluid (H_2O) density. Conditions were maintained for 24 hours via a pressure (within <0.2%) and temperature controller (within 0.02%), once the desired pressure and temperature were attained. Actual pressures were calculated by the calibration Hui et al. (2008) which incorporates a 6% correction. The running temperature was measured with a type-S thermocouple ($Pt_{90}Rh_{10}$-Pt) and simultaneously recorded by a computer program. Temperature at the center of the experimental charge is the thermocouple temperature plus a correction based on the calibrated vertical temperature gradient inside the charge (Hui et al., 2008). The overall uncertainty in temperature for each

experiment is listed in Table B.3. Experimental assemblages were rapidly quenched to room temperature within <30 s. This minimizes, if not eliminates, back-reaction between the crystal and fluid during quench (Antignano and Manning, 2008). After quench, the capsule was cleaned and weighed, then punctured and dried at 120°C for 1 hour. The capsule was weighed again, opened, and the crystal was removed. Comparison of the total capsule weight before and after the experiments showed no fluid was lost during the experiment. The crystal was cleaned with isopropanol and weighed four times to determine the average mass loss.

B.2.2 Piston cylinder run products

Piston cylinder run products from experiments 08Au30Zr03 and 04Au24Zr17 included the partially dissolved starting crystal only. These run product crystals were mounted in epoxy, polished and EMPA performed to determine final Zr concentrations (Tables B.3, B.5, B.11). In the 3 wt% NaF experiments at 900°C no partially dissolved starting crystal could be found, however many smaller crystals existed that could be considered transport crystals as described by Tropper and Manning, (2005). The transport crystals in experiment 06Pt26Zr02 were too small and numerous to recover therefore the mass loss could not be determined (Figure B.9, Table B.7). Experiment 12Pt35Zr33 contained no starting crystal but seven transport crystals (Figure B.10). All crystals from this experiment were removed, weighed, mounted in epoxy, polished and EMPA done. The Zr concentrations in the rutile ranged from 0.88 to 1.09 wt%, with an average of 1.02 ± 0.23 wt% Zr (Table B.9). The starting crystal from experiment 05Pt25Zr21 contained some possible transport crystals attached to it, which broke into four pieces during removal (Figure B.11). All crystals from this experiment were also extracted, weighed, and EMPA done. The Zr concentrations ranged from 0.83 to 2.19 wt%, with an average of 1.21 ± 0.79 wt% Zr (Table B.13).

B.2.3 References

Hui, H., Zhang, Y., Xu, Z., Behrens, H. (2008) Pressure dependence of the speciation of dissolved water in rhyolitic melts. Geochimica et Cosmochimica Acta, 72, 3229-3240.

Figure B.7: (Left) Piston cylinder lab. (Right) Close up of piston cylinder assembled.

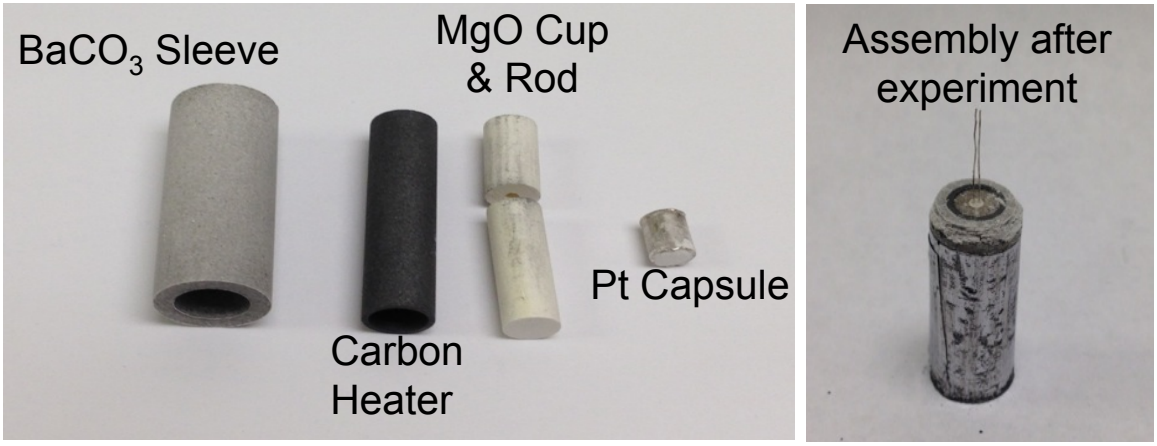

Figure B.8: (Left) Piston cylinder charge components. (Right) Piston cylinder charge assembly after being run in an experiment.

Table B.3: Zr-Rutile Piston cylinder experimental conditions and results

Experiment ID	08Au30Zr03	06Pt26Zr02	12Pt35Zr33	04Au24Zr17	05Pt25Zr21
Starting Capsule Height (mm)	6.65	6.77	6.45	6.93	6.54
Ending Capsule Height (mm)	3.90	4.25	4.10	3.65	3.62
Fluid Composition (wt%)	3% NaF	3% NaF	3% NaF	4% NaF	4% NaF
Time (h)	24	24	24	24	24
Temperature(°C) $\pm\,\sigma$)	703(28)	903(37)	900(35)	690(15)	884(21)
Pressure(GPa)($\pm\sigma$)	1.5(0.002)	1.5(0.002)	1.0(0.002)	1.0(0.002)	1.0(0.002)
Fluid (mg)	40	40	40	40	40
Fluid Density (g/cm$^{\mathbf{3}}$)	1.01(0.01)	0.82(0.01)	0.93(0.01)	0.92(0.01)	0.83(0.01)
$^{\boldsymbol{a}}$Crystal weight in(μg $\pm\sigma$)	374(7)	271(8)	1439(5)	537(13)	936(4)
$^{\boldsymbol{a}}$Crystal weight out(μg $\pm\sigma$)	368(1)	$*$	1257(1)$*$	514(2)	604(4)$*$
Zr in(wt% $\pm\sigma$)	2.83(0.21)	3.07(0.36)	0.93(0.05)	3.31(0.16)	3.39(0.09)
Zr out(wt% $\pm\sigma$)	2.61(0.69)	$-$	1.02(0.23)	2.75(0.16)	1.21(0.79)
$^{\boldsymbol{b}}$ppm Zr in Fluid (error)	59(27)	$**$	$**$	156(51)	793(516)

^{a}The crystal was weighed four times and the average mass is reported. The one sigma standard deviation of the average mass is provided in parentheses.

^{b}Error is calculated by propagating the error from weighing and the analytical error from the EMPA.

$*$Run products contained broken crystal fragments as well as the primary crystals.

$**$Could not determine Zr concentration in the fluid.

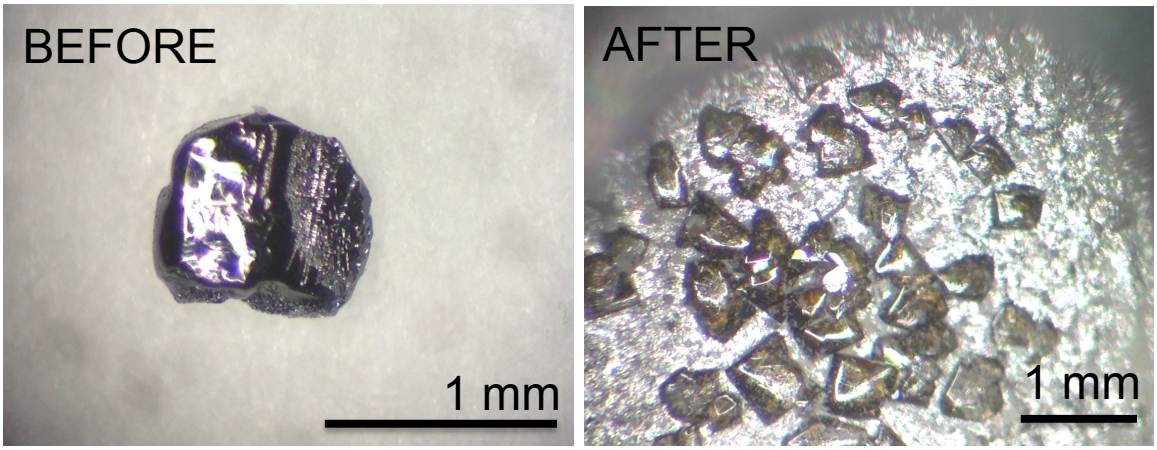

Figure B.9: Starting and run crystal(s) from experiment 06Pt26Zr02. The starting Zr-doped rutile crystal loaded into the experimental Pt capsule (Left). After experiment 06Pt26Zr02 was completed, the capsule contained no starting crystal but multiple transport crystals (right).

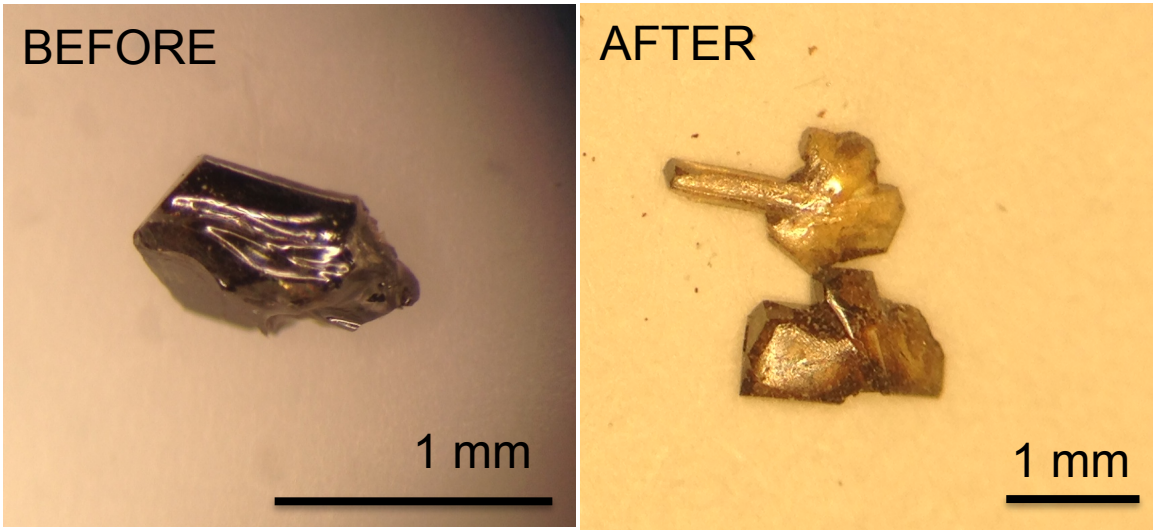

Figure B.10: Starting and run crystal(s) from experiment 12Pt35Zr33. The starting Zr-doped rutile crystal loaded into the experimental capsule (Left). After experiment 12Pt35Zr33 was completed, the capsule contained no starting crystal but seven transport crystals (only 2 are shown, right).

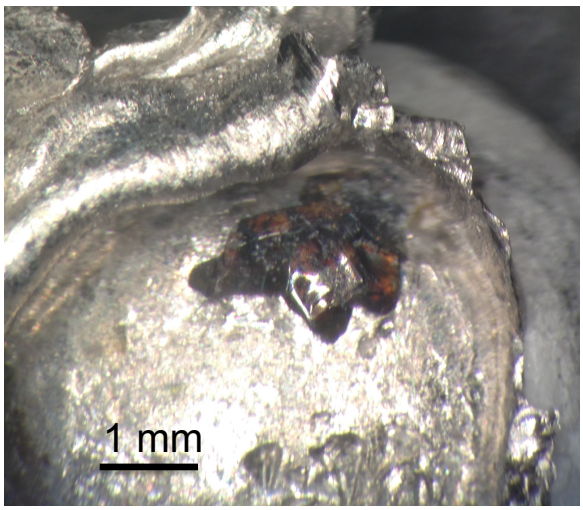

Figure B.11: Run crystal from experiment 05Pt25Zr21. After experiment 12Pt35Zr33 was completed, the starting crystal contained some possible transport crystals attached to it, which broke into four pieces during removal There was no starting crystal image for this experiment.

B.2.4 EMPA data of starting and run crystals

Table B.4: EMPA analysis of starting crystal from experiment 08Au30Zr03. The linescan step-size for dataset 2, across the length of the crystal was 34 μm. Oxygen values are calculated.

DataSet/Point	Ti	Mo	Zr	O	Total	X	Y	Z	Distance (μm)	Mean Z
2 / 1 .	57.5412	0.0309	3.2927	39.6113	100.476	-11758	-18516	187	0	17.158
2 / 2 .	57.8565	0.059	3.1784	39.7959	100.8898	-11758.8	-18549.7	187	33.72	17.2083
2 / 3 .	57.6281	0.0711	3.1095	39.6252	100.434	-11759.6	-18583.4	187	67.45	17.1219
2 / 4 .	58.0317	0.0996	2.9381	39.8489	100.9182	-11760.4	-18617.1	187	101.17	17.1719
2 / 5 .	57.7776	0.1227	2.8347	39.6545	100.3895	-11761.1	-18650.9	187	134.89	17.0689
2 / 6 .	58.1708	0.1472	2.7753	39.9086	101.002	-11761.9	-18684.6	187	168.62	17.1622
2 / 7 .	58.0211	0.1393	2.8325	39.8246	100.8175	-11762.7	-18718.3	187	202.34	17.1421
2 / 8 .	58.0591	0.1357	2.8137	39.8416	100.8501	-11763.5	-18752	187	236.06	17.1428
2 / 9 .	58.0308	0.161	2.6863	39.7907	100.6688	-11764.3	-18785.7	187	269.79	17.0922
2 / 10 .	58.0002	0.1475	2.6873	39.7639	100.5989	-11765.1	-18819.4	187	303.51	17.078
2 / 11 .	58.213	0.1389	2.6458	39.8872	100.8848	-11765.9	-18853.1	187	337.23	17.1145
2 / 12 .	58.045	0.158	2.6453	39.7843	100.6326	-11766.6	-18886.9	187	370.96	17.0771
2 / 13 .	58.274	0.1425	2.6101	39.9172	100.9438	-11767.4	-18920.6	187	404.68	17.1175
2 / 14 .	57.788	0.1451	2.655	39.6096	100.1976	-11768.2	-18954.3	187	438.4	17.005
2 / 15 .	58.1137	0.1599	2.702	39.8511	100.8267	-11769	-18988	187	472.13	17.1211

Table B.5: EMPA analysis of run crystal from experiment 08Au30Zr03. The linescan step-size for dataset 1, across the length of the crystal was 20 μm. The linescan step-size for dataset 2, across the length of the crystal was 15 μm. Oxygen values are calculated.

DataSet/Point	Ti	Zr	O	Total	X	Y	Z	Distance (μm)	Mean Z
1 / 1 .	58.2751	1.9283	39.6075	99.8109	9983	4701	88	0	16.7604
1 / 2 .	58.4112	1.9896	39.7199	100.1207	9999.5	4690.6	88	19.54	16.8239
1 / 3 .	57.7806	2.1172	39.3434	99.2413	10016.1	4680.2	88	39.07	16.7061
1 / 4 .	58.535	2.2003	39.8765	100.6118	10032.6	4669.8	88	58.61	16.9479
1 / 5 .	58.2463	2.2974	39.7177	100.2615	10049.1	4659.4	88	78.14	16.9106
1 / 6 .	57.5309	2.3419	39.2554	99.1282	10065.7	4648.9	88	97.68	16.734
1 / 7 .	57.8095	2.4046	39.4635	99.6776	10082.2	4638.5	88	117.21	16.837
1 / 8 .	57.594	2.4831	39.3471	99.4241	10098.7	4628.1	88	136.75	16.8117
1 / 9 .	57.9137	2.52	39.5736	100.0074	10115.2	4617.7	88	156.28	16.9149
1 / 10 .	57.738	2.5685	39.4732	99.7797	10131.8	4607.3	88	175.82	16.8876
1 / 11 .	57.3827	2.6294	39.2572	99.2693	10148.3	4596.9	88	195.35	16.8165
1 / 12 .	57.5116	2.7084	39.3711	99.591	10164.8	4586.5	88	214.89	16.8856
1 / 13 .	57.2351	2.7173	39.1895	99.1418	10181.4	4576.1	88	234.42	16.8138
1 / 14 .	57.2428	2.8287	39.2337	99.3051	10197.9	4565.6	88	253.96	16.8636
1 / 15 .	56.8428	2.9193	38.9983	98.7604	10214.4	4555.2	88	273.49	16.793
1 / 16 .	57.158	2.9797	39.23	99.3676	10230.9	4544.8	88	293.03	16.905
1 / 17 .	57.3976	3.0232	39.4054	99.8262	10247.5	4534.4	88	312.56	16.9892
1 / 18 .	57.4433	3.1111	39.4667	100.021	10264	4524	89	332.1	17.0393
2 / 1 .	57.9738	3.3311	39.8983	101.2032	10328	4409	98	0	17.2786
2 / 2 .	58.3699	3.3415	40.1665	101.8779	10320.4	4422.4	98	15.4	17.3913
2 / 3 .	57.9205	3.3098	39.8552	101.0855	10312.8	4435.8	98	30.8	17.2549
2 / 4 .	57.6522	2.2325	39.2981	99.1828	10305.1	4449.1	98	46.19	16.7203
2 / 5 .	58.3773	2.7033	39.9476	101.0281	10297.5	4462.5	98	61.59	17.1201
2 / 6 .	58.4019	2.9258	40.0421	101.3698	10289.9	4475.9	98	76.99	17.2221
2 / 7 .	58.0863	3.0098	39.8607	100.9568	10282.3	4489.3	98	92.39	17.1718

Table B.5: EMPA analysis of run crystal from experiment 08Au30Zr03 continued

DataSet/Point	Ti	Zr	O	Total	X	Y	Z	Distance (μm)	Mean Z
2 / 8 .	57.9556	3.0072	39.7725	100.7352	10274.7	4502.7	98	107.79	17.1349
2 / 9 .	58.167	3.0449	39.9269	101.1388	10267.1	4516	98	123.18	17.2089
2 / 10 .	58.6247	3.0044	40.2185	101.8476	10259.4	4529.4	98	138.58	17.3167
2 / 11 .	58.202	3.0365	39.9474	101.1859	10251.8	4542.8	98	153.98	17.2148
2 / 12 .	58.193	2.9472	39.9101	101.0503	10244.2	4556.2	98	169.38	17.1742
2 / 13 .	58.5054	2.9978	40.1365	101.6397	10236.6	4569.6	98	184.78	17.2812
2 / 14 .	58.1408	2.9623	39.8805	100.9835	10229	4583	98	200.17	17.1663
2 / 15 .	58.411	2.8863	40.0343	101.3316	10221.3	4596.3	98	215.57	17.2077
2 / 16 .	58.3628	2.9201	40.014	101.2969	10213.7	4609.7	98	230.97	17.209
2 / 17 .	58.0596	2.8397	39.7832	100.6825	10206.1	4623.1	98	246.37	17.0916
2 / 18 .	59.0381	2.8502	40.4406	102.3289	10198.5	4636.5	98	261.77	17.3637
2 / 19 .	58.2463	2.8552	39.9134	101.0148	10190.9	4649.9	98	277.16	17.1493
2 / 20 .	58.6924	2.3289	40.0268	101.0481	10183.2	4663.2	98	292.56	17.046
2 / 21 .	59.8355	0.0724	39.9989	99.9068	10175.6	4676.6	98	307.96	16.3927
2 / 22 .	56.912	0.115	38.0607	95.0876	10168	4690	98	323.36	15.6115

Table B.6: EMPA analysis of starting crystal from experiment 06Pt26Zr02. The linescan step-size for dataset 1, across the length of the crystal was 50 μm. Oxygen values are calculated.

DataSet/Point	Ti	Mo	Zr	O	Total	X	Y	Z	Distance (μm)	Mean Z
1 / 1 .	56.7592	0.0467	3.3336	39.1111	99.2507	-15076	-18775	187	0	16.969
1 / 2 .	56.5642	0.0855	3.0621	38.905	98.6167	-15026.1	-18775	187	49.93	16.8173
1 / 3 .	56.7327	0.0772	2.802	38.9222	98.534	-14976.1	-18775	187	99.86	16.7482
1 / 4 .	57.315	0.0857	2.4828	39.2035	99.0869	-14926.2	-18775	187	149.79	16.7747
1 / 5 .	57.3235	0.0804	2.5606	39.2338	99.1983	-14876.3	-18775	187	199.71	16.8079
1 / 6 .	57.5826	0.0741	2.549	39.3997	99.6054	-14826.4	-18775	187	249.64	16.8709
1 / 7 .	57.4113	0.1278	2.7209	39.3724	99.6325	-14776.4	-18775	187	299.57	16.9223
1 / 8 .	57.3866	0.1027	2.9841	39.4357	99.9092	-14726.5	-18775	187	349.5	17.0167
1 / 9 .	57.2388	0.1359	3.2048	39.431	100.0105	-14676.6	-18775	187	399.43	17.086
1 / 10 .	56.8786	0.1074	3.2294	39.1847	99.4002	-14626.6	-18775	187	449.36	16.985
1 / 11 .	56.99	0.1021	3.3032	39.2824	99.6777	-14576.7	-18775	187	499.29	17.0446
1 / 12 .	57.094	0.0646	3.335	39.3442	99.8378	-14526.8	-18775	187	549.21	17.0693
1 / 13 .	56.9963	0.0451	3.4227	39.3	99.7641	-14476.9	-18775	187	599.14	17.0712
1 / 14 .	56.67	0.047	3.445	39.0907	99.2527	-14426.9	-18775	187	649.07	16.9924
1 / 15 .	56.4884	0.0383	3.5662	39.0075	99.1003	-14377	-18775	187	699	16.9906

Table B.7: EMPA analysis of run crystal from experiment 06Pt26Zr02. Randomly selected point were chosen based on crystal space available. The run product crystal was very small therefore it was difficult to mount and polish. Oxygen values are calculated.

DataSet/Point	Ti	Zr	O	Total	X	Y	Z	Distance (μm)	Mean Z
18 / 1 .	57.0907	1.5485	38.683	97.3222	13371	4691	100	point	16.274
19 / 1 .	48.8052	1.8393	33.2498	83.8943	13376	4681	100	point	14.1329
20 / 1 .	53.4339	1.1808	36.111	90.7257	13381	4700	100	point	15.1166
21 / 1 .	56.2286	1.3683	38.0438	95.6407	13370	4727	100	point	15.9611
22 / 1 .	58.0613	1.282	39.2379	98.5812	13370	4737	100	point	16.4253
23 / 1 .	54.6682	1.647	37.0992	93.4145	13412	4741	100	point	15.6538

Table B.8: EMPA analysis of starting crystal from experiment 12Pt35Zr33. The linescan step-size for dataset 10, across the length of the crystal was 58 μm. The linescan step-size for dataset 11, across the length of the crystal was 67 μm. Oxygen values are calculated.

DataSet/Point	Ti	Mo	Zr	O	Total	X	Y	Z	Distance (μm)	Mean Z
10 / 1 .	58.5936	0.2078	1.0004	39.5988	99.4006	10197	4359	126	0	16.546
10 / 2 .	58.9979	0.2073	0.943	39.8484	99.9967	10253	4343	125	58.25	16.6317
10 / 3 .	59.1391	0.1973	0.9601	39.9437	100.2401	10309	4327	125	116.49	16.673
10 / 4 .	58.6772	0.2179	0.9124	39.6287	99.4362	10365	4311	125	174.73	16.5358
10 / 5 .	58.9924	0.2174	1.0122	39.8741	100.0961	10421	4295	125	232.97	16.6645
10 / 6 .	59.1071	0.2283	0.9346	39.929	100.199	10477	4279	125	291.21	16.6676
10 / 7 .	59.4	0.2219	0.9713	40.1342	100.7273	10533	4263	125	349.45	16.7604
10 / 8 .	59.1079	0.248	0.9206	39.9344	100.2108	10589	4247	125	407.69	16.6709
10 / 9 .	58.9973	0.1914	0.8864	39.8202	99.8952	10645	4231	125	465.93	16.5999
10 / 10 .	58.4538	0.4127	0.9679	39.5964	99.4308	10701	4215	125	524.17	16.588
11 / 1 .	58.5922	0.4673	0.9738	39.7183	99.7516	10491	4801	122	0	16.6535
11 / 2 .	58.8156	0.1773	0.889	39.6926	99.5745	10521.1	4741.6	121	66.64	16.5449
11 / 3 .	58.4648	0.4031	0.9955	39.6087	99.4721	10551.2	4682.1	121	133.28	16.5985
11 / 4 .	58.4644	0.3593	0.934	39.5649	99.3227	10581.3	4622.7	121	199.91	16.5519
11 / 5 .	58.8248	0.4197	0.9054	39.8258	99.9757	10611.4	4563.2	120	266.55	16.6659
11 / 6 .	58.8116	0.434	0.9269	39.8318	100.0043	10641.6	4503.8	120	333.18	16.6782
11 / 7 .	58.4167	0.4476	0.8923	39.5626	99.3192	10671.7	4444.3	120	399.82	16.5616
11 / 8 .	58.8967	0.247	0.8044	39.752	99.7	10701.8	4384.9	119	466.46	16.5629
11 / 9 .	58.5793	0.2283	0.8406	39.5434	99.1916	10731.9	4325.4	119	533.09	16.4831
11 / 10 .	58.5175	0.3949	0.9876	39.637	99.5369	10762	4266	119	599.73	16.6057

Table B.9: EMPA analysis of run crystals from experiment 12Pt35Zr33. Experiment 12Pt35Zr33 contained no starting crystal but seven transport crystals (A-G below, Figure B.10). The linescan step-size for datasets 1-12, across the length of the crystals were ∼30 μm. The linescan step-size for datasets 13-17, across the length of the crystals were 20 μm. Oxygen values are calculated.

DataSet/Point	Ti	Zr	O	Total	X	Y	Z	Distance (μm)	Mean Z
12Pt35Zr33_A									
1 / 1 .	59.6675	0.905	40.1787	100.7511	12050	4996	96	0	16.7031
1 / 2 .	59.3418	1.0698	40.019	100.4306	12050	4965.3	96	30.68	16.6846
1 / 3 .	59.4065	0.976	40.0292	100.4116	12050	4934.6	96	61.36	16.6621
1 / 4 .	59.2785	1.0843	39.9817	100.3445	12050	4904	97	92.05	16.6735
1 / 5 .	59.555	1.0376	40.1501	100.7427	12050	4873.3	97	122.73	16.7292
1 / 6 .	59.464	1.1544	40.1302	100.7486	12050	4842.6	98	153.42	16.7542
1 / 7 .	59.5513	1.2958	40.2382	101.0853	12050	4811.9	98	184.1	16.8387
1 / 8 .	59.6797	1.2015	40.2908	101.1719	12050	4781.2	99	214.79	16.8334
1 / 9 .	59.6544	0.9625	40.1901	100.8069	12050	4750.5	99	245.47	16.7242
1 / 10 .	59.4311	0.899	40.0187	100.3488	12050	4719.9	100	276.17	16.6359
1 / 11 .	59.7465	0.7577	40.1798	100.6839	12050	4689.2	100	306.84	16.6617
1 / 12 .	59.5023	0.7938	40.0293	100.3255	12050	4658.5	101	337.54	16.6104
1 / 13 .	59.9618	0.8476	40.3552	101.1646	12050	4627.8	101	368.22	16.7591
1 / 14 .	60.1005	0.6412	40.3755	101.1172	12050	4597.1	101	398.9	16.7086
1 / 15 .	59.49	1.0222	40.1012	100.6133	12050	4566.5	102	429.59	16.7047
1 / 16 .	59.4683	0.9203	40.051	100.4395	12050	4535.8	102	460.27	16.6552
1 / 17 .	60.1467	0.8935	40.4948	101.5349	12050	4505.1	103	490.96	16.8292
1 / 18 .	59.9087	1.0025	40.374	101.2852	12050	4474.4	103	521.64	16.8108
1 / 19 .	60.1038	1.0446	40.5191	101.6675	12050	4443.7	104	552.33	16.8822
1 / 20 .	59.5132	1.1862	40.1743	100.8737	12050	4413	104	583.01	16.7813
1 / 21 .	60.2005	1.0759	40.5947	101.8711	12050	4382.4	105	613.7	16.922
1 / 22 .	60.3482	0.8729	40.6222	101.8433	12050	4351.7	105	644.38	16.8756
1 / 23 .	60.0833	0.865	40.4425	101.3907	12050	4321	106	675.07	16.7997

Table B.9: EMPA analysis of run crystal from experiment 12Pt35Zr33 continued

DataSet/Point	Ti	Zr	O	Total	X	Y	Z	Distance (μm)	Mean Z
2 / 1 .	60.0678	0.9825	40.4733	101.5235	11815	4320	105	0	16.8458
2 / 2 .	59.9427	1.0544	40.4149	101.412	11844.9	4322.6	105	30.01	16.8424
2 / 3 .	60.2305	1.0198	40.5951	101.8453	11874.8	4325.2	105	60.03	16.9062
2 / 4 .	60.1959	1.0193	40.5718	101.7871	11904.7	4327.8	105	90.04	16.8966
2 / 5 .	60.1017	1.0169	40.508	101.6266	11934.6	4330.4	105	120.05	16.8698
2 / 6 .	60.1122	0.9396	40.4879	101.5398	11964.5	4333	105	150.06	16.8396
2 / 7 .	60.258	0.9872	40.6021	101.8473	11994.4	4335.6	105	180.08	16.8998
2 / 8 .	59.98	0.7887	40.3467	101.1153	12024.3	4338.2	105	210.09	16.7388
2 / 9 .	60.2369	0.8673	40.5459	101.6501	12054.2	4340.8	105	240.1	16.8427
2 / 10 .	60.0288	0.9355	40.4308	101.3951	12084.1	4343.4	105	270.12	16.815
2 / 11 .	60.506	0.8141	40.707	102.0272	12114	4346	105	300.13	16.8935
2 / 12 .	59.8989	0.8478	40.3132	101.0599	12143.9	4348.6	105	330.14	16.7419
2 / 13 .	60.1814	0.9317	40.5314	101.6444	12173.8	4351.2	105	360.15	16.8551
2 / 14 .	60.3442	0.8442	40.6094	101.7977	12203.7	4353.8	105	390.17	16.8621
2 / 15 .	60.2261	0.7184	40.4864	101.431	12233.6	4356.4	105	420.18	16.776
2 / 16 .	60.5843	0.6797	40.7121	101.9762	12263.5	4359	105	450.19	16.8574
2 / 17 .	60.2244	0.6615	40.4653	101.3511	12293.4	4361.6	105	480.21	16.7512
2 / 18 .	59.9066	0.8879	40.3324	101.1269	12323.3	4364.2	105	510.22	16.7612
2 / 19 .	59.6055	1.2339	40.2527	101.0922	12353.2	4366.8	105	540.23	16.827
2 / 20 .	59.8779	1.3099	40.4613	101.6491	12383.1	4369.4	105	570.24	16.934
2 / 21 .	59.7755	1.2658	40.3775	101.4188	12413	4372	106	600.26	16.8872
12Pt35Zr33_B									
3 / 1 .	59.626	0.8331	40.1257	100.5848	12238	2312	101	0	16.661
3 / 2 .	59.4752	0.8854	40.0434	100.404	12238	2342	101	30	16.6422
3 / 3 .	59.5806	0.8153	40.0892	100.4851	12238.1	2372	101	60	16.641
3 / 4 .	59.3297	0.8577	39.9364	100.1237	12238.1	2402	101	90	16.5905
3 / 5 .	59.1361	0.8538	39.8058	99.7958	12238.2	2432	101	120	16.536

Table B.9: EMPA analysis of run crystal from experiment 12Pt35Zr33 continued

DataSet/Point	Ti	Zr	O	Total	X	Y	Z	Distance (μm)	Mean Z
3 / 6 .	59.8709	0.8003	40.2778	100.949	12238.2	2462	101	150	16.714
3 / 7 .	60.0481	1.1575	40.5215	101.7271	12238.2	2492	101	180	16.9153
3 / 8 .	58.875	1.0493	39.6999	99.6242	12238.3	2522	101	210	16.5482
3 / 9 .	59.1859	1.1648	39.9481	100.2987	12238.3	2552	101	240	16.6827
3 / 10 .	59.075	1.4835	39.9858	100.5444	12238.4	2582	101	270	16.7888
3 / 11 .	59.1784	1.0941	39.9183	100.1908	12238.4	2612	101	300	16.6504
3 / 12 .	59.1412	1.5254	40.0448	100.7113	12238.4	2642	101	330	16.8248
3 / 13 .	59.4086	1.0018	40.0397	100.4502	12238.5	2672	101	360	16.6738
3 / 14 .	59.0559	0.8812	39.7618	99.6988	12238.5	2702	101	390	16.5257
3 / 15 .	59.152	0.835	39.8097	99.7967	12238.6	2732	101	420	16.5322
3 / 16 .	58.5264	0.9748	39.4409	98.942	12238.6	2762	101	450	16.421
3 / 17 .	59.5748	1.069	40.1743	100.8181	12238.6	2792	101	480	16.748
3 / 18 .	59.1254	1.4149	39.9954	100.5357	12238.7	2822	101	510	16.7732
3 / 19 .	59.227	1.1117	39.957	100.2957	12238.7	2852	101	540	16.6712
3 / 20 .	59.2801	0.9505	39.9358	100.1663	12238.8	2882	101	570	16.6167
3 / 21 .	59.4257	0.8874	40.011	100.3241	12238.8	2912	101	600	16.6295
3 / 22 .	59.5245	1.0096	40.1199	100.6539	12238.8	2942	101	630	16.7088
3 / 23 .	59.0824	0.9613	39.8076	99.8513	12238.9	2972	101	660	16.5673
3 / 24 .	59.2005	0.9982	39.8994	100.0982	12238.9	3002	101	690	16.6154
3 / 25 .	59.2117	0.9531	39.8911	100.0558	12239	3032	101	720	16.5991
3 / 26 .	59.3963	0.9307	40.0066	100.3336	12239	3062	101	750	16.64
4 / 1 .	59.0318	1.0561	39.807	99.8949	11989	3068	102	0	16.594
4 / 2 .	59.4529	1.1211	40.1111	100.6851	11983.3	3039.2	102	29.37	16.737
4 / 3 .	59.2943	1.051	39.9806	100.326	11977.5	3010.4	102	58.73	16.6636
4 / 4 .	59.4701	0.9128	40.0496	100.4325	11971.8	2981.6	102	88.1	16.6525
4 / 5 .	60.3183	0.7982	40.576	101.6925	11966.1	2952.8	102	117.46	16.8354
4 / 6 .	59.2503	0.9023	39.8991	100.0517	11960.3	2924	102	146.83	16.5879

Table B.9: EMPA analysis of run crystal from experiment 12Pt35Zr33 continued

DataSet/Point	Ti	Zr	O	Total	X	Y	Z	Distance (μm)	Mean Z
4 / 7 .	59.3255	0.9377	39.9617	100.2249	11954.6	2895.2	102	176.19	16.6236
4 / 8 .	59.5255	0.9295	40.0924	100.5473	11948.9	2866.4	102	205.56	16.6748
4 / 9 .	59.5253	1.1833	40.1813	100.89	11943.1	2837.6	102	234.92	16.7834
4 / 10 .	59.4564	1.1829	40.1351	100.7744	11937.4	2808.8	102	264.29	16.7644
4 / 11 .	59.2173	1.0084	39.9142	100.1399	11931.7	2780	102	293.65	16.6243
4 / 12 .	58.4078	1.0376	39.3836	98.829	11925.9	2751.2	102	323.02	16.4154
4 / 13 .	59.1654	1.1593	39.9324	100.2571	11920.2	2722.4	102	352.38	16.6747
4 / 14 .	59.8339	1.2248	40.402	101.4607	11914.5	2693.6	102	381.75	16.8855
4 / 15 .	58.8877	1.1829	39.7552	99.8258	11908.7	2664.8	102	411.11	16.6089
4 / 16 .	59.2208	1.4198	40.0609	100.7015	11903	2636	102	440.48	16.8014
12Pt35Zr33_C									
5 / 1 .	59.508	1.0825	40.1344	100.7248	12043	1388	102	0	16.7355
5 / 2 .	59.5373	1.1674	40.1837	100.8884	12069.4	1402.4	102	30.11	16.7798
5 / 3 .	58.9875	1.598	39.9675	100.553	12095.9	1416.8	102	60.21	16.8139
5 / 4 .	59.1699	1.5196	40.0619	100.7514	12122.3	1431.2	102	90.32	16.8302
5 / 5 .	59.3915	0.9752	40.0189	100.3856	12148.8	1445.6	102	120.42	16.6577
5 / 6 .	59.1734	0.8692	39.836	99.8786	12175.2	1459.9	102	150.53	16.5527
5 / 7 .	58.8633	1.6799	39.9133	100.4565	12201.7	1474.3	102	180.63	16.8149
5 / 8 .	58.7941	1.557	39.8239	100.175	12228.1	1488.7	102	210.74	16.7434
5 / 9 .	59.7788	0.8886	40.2473	100.9146	12254.6	1503.1	102	240.85	16.7265
5 / 10 .	59.17	1.6541	40.1091	100.9331	12281	1517.5	102	270.95	16.8877
5 / 11 .	58.4821	1.7018	39.6663	99.8503	12307.4	1531.9	102	301.06	16.7201
5 / 12 .	59.3441	0.9188	39.9675	100.2303	12333.9	1546.3	102	331.16	16.6206
5 / 13 .	59.4606	1.1239	40.1173	100.7018	12360.3	1560.7	102	361.27	16.7403
5 / 14 .	59.0775	1.1054	39.8548	100.0377	12386.8	1575.1	102	391.37	16.6276
5 / 15 .	59.1551	1.1937	39.9377	100.2865	12413.2	1589.4	102	421.48	16.6866
5 / 16 .	59.1321	1.0883	39.8853	100.1057	12439.7	1603.8	102	451.58	16.6352

Table B.9: EMPA analysis of run crystal from experiment 12Pt35Zr33 continued

DataSet/Point	Ti	Zr	O	Total	X	Y	Z	Distance (μm)	Mean Z
5 / 17 .	59.8764	1.081	40.38	101.3374	12466.1	1618.2	102	481.69	16.8356
5 / 18 .	59.1891	1.0125	39.8968	100.0985	12492.6	1632.6	102	511.8	16.6184
5 / 19 .	59.7746	0.9763	40.2753	101.0262	12519	1647	102	541.9	16.763
6 / 1 .	59.0588	1.0051	39.8072	99.8711	12450	1335	103	0	16.5796
6 / 2 .	59.2256	1.0109	39.9206	100.1571	12429.7	1356.8	103	29.8	16.6276
6 / 3 .	59.7232	0.9908	40.246	100.9601	12409.3	1378.5	103	59.6	16.7551
6 / 4 .	59.6292	1.1069	40.2239	100.96	12388.9	1400.3	103	89.4	16.7791
6 / 5 .	59.288	1.2241	40.0371	100.5492	12368.6	1422.1	103	119.19	16.736
6 / 6 .	59.1528	1.1502	39.9209	100.2239	12348.2	1443.8	103	148.99	16.6674
6 / 7 .	59.161	1.1318	39.9199	100.2126	12327.9	1465.6	104	178.79	16.6617
6 / 8 .	59.1736	1.1688	39.9413	100.2837	12307.5	1487.4	104	208.59	16.681
6 / 9 .	58.6179	1.7439	39.7718	100.1336	12287.2	1509.1	104	238.39	16.7752
6 / 10 .	59.8331	1.1516	40.3758	101.3605	12266.8	1530.9	104	268.19	16.854
6 / 11 .	58.8007	1.8055	39.9155	100.5217	12246.5	1552.6	104	297.99	16.8516
6 / 12 .	59.1396	1.7241	40.1134	100.9771	12226.1	1574.4	104	327.78	16.9094
6 / 13 .	59.5137	1.8196	40.3968	101.7301	12205.8	1596.2	105	357.59	17.0526
6 / 14 .	60.3532	0.8321	40.6112	101.7966	12185.4	1617.9	105	387.38	16.8595
6 / 15 .	59.9459	0.8477	40.3445	101.138	12165.1	1639.7	105	417.18	16.7547
6 / 16 .	60.2208	0.8283	40.5214	101.5705	12144.7	1661.5	105	446.98	16.8216
6 / 17 .	60.3288	0.8202	40.5908	101.7398	12124.4	1683.2	105	476.78	16.8477
6 / 18 .	59.9926	0.839	40.3727	101.2043	12104	1705	106	506.58	16.7638
12Pt35Zr33_D									
7 / 1 .	58.7159	0.9098	39.5446	99.1703	12398	581	102	0	16.445
7 / 2 .	59.3667	0.8941	39.9739	100.2347	12420.4	562.3	102	29.21	16.6162
7 / 3 .	59.5016	0.8248	40.0397	100.3661	12442.9	543.6	102	58.42	16.6235
7 / 4 .	58.7586	0.9143	39.5748	99.2477	12465.3	524.9	102	87.63	16.4586
7 / 5 .	59.7333	0.8826	40.2148	100.8308	12487.7	506.1	102	116.84	16.7116

Table B.9: EMPA analysis of run crystal from experiment 12Pt35Zr33 continued

DataSet/Point	Ti	Zr	O	Total	X	Y	Z	Distance (μm)	Mean Z
7 / 6 .	59.7967	0.9018	40.2639	100.9624	12510.1	487.4	102	146.05	16.7371
7 / 7 .	59.8193	1.0111	40.3173	101.1476	12532.6	468.7	102	175.26	16.7901
7 / 8 .	59.5076	1.0932	40.1379	100.7386	12555	450	102	204.47	16.74
8 / 1 .	59.4563	1.2324	40.1525	100.8412	12145	313	102	0	16.7856
8 / 2 .	59.3121	1.2426	40.0597	100.6144	12166	333.3	102	29.23	16.7505
8 / 3 .	59.5005	1.1769	40.1625	100.8399	12187	353.7	102	58.46	16.7739
8 / 4 .	59.218	1.2198	39.9889	100.4267	12208	374	102	87.69	16.715
8 / 5 .	59.732	1.3654	40.3833	101.4806	12229	394.3	102	116.92	16.9179
8 / 6 .	59.5452	1.5001	40.3057	101.351	12250	414.7	102	146.15	16.9244
8 / 7 .	59.5251	1.3001	40.2222	101.0473	12271	435	102	175.39	16.8333
9 / 1 .	58.9582	1.2297	39.8187	100.0066	12387	89	102	0	16.6482
9 / 2 .	59.4814	1.1295	40.1331	100.744	12410.3	108.5	102	30.41	16.7484
9 / 3 .	59.3447	0.8782	39.9537	100.1765	12433.7	128	102	60.82	16.6034
9 / 4 .	58.9182	1.11	39.75	99.7782	12457	147.5	102	91.23	16.586
9 / 5 .	59.122	1.0717	39.8727	100.0664	12480.3	167	102	121.63	16.6253
9 / 6 .	59.4767	0.9463	40.0657	100.4886	12503.7	186.5	102	152.04	16.6686
9 / 7 .	59.652	1.0528	40.2202	100.9251	12527	206	102	182.45	16.7622
12Pt35Zr33_E									
10 / 1 .	59.741	0.9298	40.2365	100.9073	12257	-1196	101	0	16.7339
10 / 2 .	59.6355	0.8455	40.1365	100.6175	12286.6	-1190.2	101	30.17	16.6689
10 / 3 .	59.4895	1.0474	40.1097	100.6465	12316.2	-1184.4	101	60.34	16.7154
10 / 4 .	60.1459	0.9438	40.5119	101.6017	12345.8	-1178.7	101	90.51	16.8506
10 / 5 .	60.32	0.8053	40.5797	101.705	12375.4	-1172.9	101	120.68	16.8389
10 / 6 .	59.8919	0.7476	40.2734	100.9129	12405.1	-1167.1	101	150.85	16.6972
10 / 7 .	59.481	0.7289	39.9923	100.2022	12434.7	-1161.3	101	181.02	16.5768
10 / 8 .	59.5764	0.7796	40.0739	100.4299	12464.3	-1155.6	101	211.19	16.6246
10 / 9 .	58.5011	0.7826	39.3565	98.6402	12493.9	-1149.8	101	241.36	16.3318

Table B.9: EMPA analysis of run crystal from experiment 12Pt35Zr33 continued

DataSet/Point	Ti	Zr	O	Total	X	Y	Z	Distance (μm)	Mean Z
10 / 10 .	59.1065	0.9379	39.8155	99.8599	12523.5	-1144	101	271.53	16.5638
10 / 11 .	59.782	0.601	40.1485	100.5315	12553.1	-1138.2	101	301.7	16.6043
10 / 12 .	59.7955	0.7559	40.2119	100.7633	12582.7	-1132.4	101	331.87	16.6743
10 / 13 .	59.5986	0.7758	40.0874	100.4617	12612.3	-1126.7	101	362.03	16.629
10 / 14 .	59.2487	0.8083	39.865	99.922	12641.9	-1120.9	101	392.2	16.5472
10 / 15 .	59.622	0.7559	40.096	100.4739	12671.6	-1115.1	101	422.37	16.6269
10 / 16 .	59.334	0.8154	39.9244	100.0738	12701.2	-1109.3	101	452.54	16.5736
10 / 17 .	59.584	0.8732	40.1118	100.569	12730.8	-1103.6	101	482.71	16.6667
10 / 18 .	59.3901	1.0958	40.0603	100.5461	12760.4	-1097.8	101	512.88	16.709
10 / 19 .	59.6349	1.0685	40.2143	100.9177	12790	-1092	101	543.05	16.7642
11 / 1 .	59.3637	0.8708	39.9637	100.1981	12236	-1092	101	0	16.6054
11 / 2 .	59.8756	0.875	40.3072	101.0579	12261.4	-1075	101	30.59	16.7472
11 / 3 .	59.8778	0.8012	40.2828	100.9618	12286.9	-1058	101	61.18	16.7162
11 / 4 .	59.6837	0.8892	40.184	100.757	12312.3	-1041	101	91.76	16.7008
11 / 5 .	59.6135	0.8321	40.117	100.5625	12337.7	-1024	101	122.35	16.6571
11 / 6 .	58.9335	0.9794	39.7144	99.6272	12363.1	-1007	101	152.94	16.5343
11 / 7 .	59.2519	1.2062	40.0067	100.4647	12388.6	-990	101	183.53	16.7184
11 / 8 .	59.4448	1.137	40.1113	100.6931	12414	-973	101	214.11	16.7416
11 / 9 .	59.5924	0.9586	40.1474	100.6984	12439.4	-956	101	244.7	16.7056
11 / 10 .	59.5112	1.2404	40.1919	100.9435	12464.9	-939	101	275.29	16.804
11 / 11 .	59.2895	1.0976	39.9938	100.3809	12490.3	-922	101	305.88	16.6823
11 / 12 .	59.2107	0.8701	39.8613	99.9421	12515.7	-905	101	336.47	16.5633
11 / 13 .	59.0271	1.5441	39.975	100.5462	12541.1	-888	101	367.05	16.8016
11 / 14 .	58.7032	1.2857	39.668	99.6569	12566.6	-871	101	397.64	16.6024
11 / 15 .	58.654	0.9731	39.5255	99.1526	12592	-854	101	428.23	16.4552
12 / 1 .	58.7669	1.2637	39.7029	99.7334	12593	-768	101	0	16.6104
12 / 2 .	58.6323	1.4238	39.6691	99.7251	12588.5	-738.3	101	30.01	16.6421

Table B.9: EMPA analysis of run crystal from experiment 12Pt35Zr33 continued

DataSet/Point	Ti	Zr	O	Total	X	Y	Z	Distance (μm)	Mean Z
12 / 3 .	58.5854	1.47	39.654	99.7094	12583.9	-708.7	101	60.02	16.6491
12 / 4 .	58.5775	1.5382	39.6727	99.7884	12579.4	-679	101	90.03	16.6762
12 / 5 .	58.0957	1.2248	39.2408	98.5613	12574.9	-649.3	101	120.04	16.4102
12 / 6 .	58.2348	1.1992	39.3248	98.7587	12570.3	-619.7	101	150.06	16.4373
12 / 7 .	59.2037	1.1044	39.9388	100.2468	12565.8	-590	101	180.07	16.6617
12 / 8 .	59.2802	1.1272	39.9979	100.4052	12561.3	-560.3	101	210.08	16.6923
12 / 9 .	59.6376	1.1218	40.2348	100.9941	12556.7	-530.7	101	240.09	16.7878
12 / 10 .	59.5059	1.2352	40.1866	100.9276	12552.2	-501	101	270.1	16.8003
12 / 11 .	59.1183	1.1726	39.9057	100.1965	12547.7	-471.3	101	300.11	16.6675
12 / 12 .	59.7068	1.2595	40.3294	101.2957	12543.1	-441.7	101	330.12	16.8657
12 / 13 .	59.591	1.233	40.2426	101.0666	12538.6	-412	101	360.13	16.8226
12 / 14 .	59.5893	1.199	40.2296	101.0179	12534.1	-382.3	101	390.14	16.8076
12 / 15 .	59.399	1.2059	40.1049	100.7099	12529.5	-352.7	101	420.15	16.7586
12 / 16 .	60.1292	1.0722	40.5458	101.7472	12525	-323	101	450.17	16.901
12Pt35Zr33_F									
13 / 1 .	58.3899	0.7495	39.2707	98.4101	12431	-1797	99	0	16.2872
13 / 2 .	59.9048	0.7829	40.2944	100.9822	12451.2	-1796.4	99	20.23	16.7158
13 / 3 .	59.5777	0.7813	40.0753	100.4344	12471.4	-1795.9	99	40.46	16.6257
13 / 4 .	59.6371	0.7039	40.0879	100.4289	12491.7	-1795.3	99	60.69	16.6088
13 / 5 .	59.695	0.81	40.1637	100.6687	12511.9	-1794.8	99	80.92	16.67
13 / 6 .	59.6359	1.008	40.1937	100.8376	12532.1	-1794.2	99	101.15	16.7386
13 / 7 .	59.6433	1.0359	40.2085	100.8877	12552.3	-1793.7	99	121.38	16.7526
13 / 8 .	59.6285	0.8201	40.1228	100.5714	12572.6	-1793.1	99	141.61	16.6561
13 / 9 .	59.3033	0.8719	39.9237	100.0988	12592.8	-1792.6	99	161.84	16.5894
13 / 10 .	59.376	0.6739	39.9029	99.9527	12613	-1792	99	182.07	16.5245
14 / 1 .	59.2031	0.9672	39.8903	100.0605	12639	-2569	95	0	16.6028
14 / 2 .	58.9441	0.9491	39.7109	99.6041	12654.7	-2583.7	95	21.55	16.5242

Table B.9: EMPA analysis of run crystal from experiment 12Pt35Zr33 continued

DataSet/Point	Ti	Zr	O	Total	X	Y	Z	Distance (μm)	Mean Z
14 / 3 .	59.0692	0.952	39.7955	99.8167	12670.5	-2598.5	95	43.09	16.5597
14 / 4 .	59.5907	0.8804	40.1188	100.5899	12686.2	-2613.2	95	64.64	16.6716
14 / 5 .	59.3709	0.8052	39.9456	100.1217	12701.9	-2627.9	95	86.19	16.5793
14 / 6 .	59.5174	0.7218	40.0142	100.2533	12717.6	-2642.6	95	107.73	16.5837
14 / 7 .	59.2776	0.7007	39.8466	99.8249	12733.4	-2657.4	95	129.28	16.5091
14 / 8 .	59.94	0.7419	40.3036	100.9855	12749.1	-2672.1	95	150.82	16.7079
14 / 9 .	59.2072	0.6862	39.7944	99.6878	12764.8	-2686.8	95	172.37	16.4836
14 / 10 .	59.186	0.8098	39.8236	99.8194	12780.6	-2701.5	95	193.92	16.5307
14 / 11 .	59.0605	0.7644	39.7239	99.5488	12796.3	-2716.3	95	215.46	16.477
14 / 12 .	59.5353	0.8119	40.0577	100.405	12812	-2731	95	237.01	16.6271
15 / 1 .	58.7887	0.8116	39.5588	99.1592	12291	-2503	95	0	16.4229
15 / 2 .	59.5089	0.8364	40.0487	100.3941	12278	-2488.5	95	19.44	16.6304
15 / 3 .	58.7627	1.0922	39.6399	99.4948	12265	-2474.1	95	38.88	16.5359
15 / 4 .	58.899	1.0393	39.7124	99.6508	12252	-2459.6	95	58.32	16.5505
15 / 5 .	58.9137	1.0665	39.7318	99.712	12239	-2445.2	95	77.76	16.5662
15 / 6 .	59.0855	1.0685	39.8473	100.0013	12226	-2430.7	95	97.2	16.614
15 / 7 .	59.4021	1.0473	40.0513	100.5006	12213	-2416.3	95	116.64	16.6915
15 / 8 .	59.6408	0.978	40.1865	100.8052	12200	-2401.8	95	136.08	16.7271
15 / 9 .	58.8229	1.0398	39.6618	99.5245	12187	-2387.4	95	155.52	16.5299
15 / 10 .	59.8079	1.0125	40.3102	101.1306	12174	-2372.9	95	174.96	16.7875
15 / 11 .	58.8445	1.0465	39.6786	99.5697	12161	-2358.5	95	194.41	16.5387
15 / 12 .	58.978	0.8007	39.6815	99.4602	12148	-2344	95	213.85	16.47
12Pt35Zr33_G									
16 / 1 .	57.9611	0.8181	39.0082	97.7874	12448	-3214	91	0	16.1993
16 / 2 .	57.6104	0.8998	38.8026	97.3128	12464.2	-3202.7	91	19.74	16.1384
16 / 3 .	57.7257	0.9291	38.8899	97.5447	12480.3	-3191.3	91	39.49	16.1825
16 / 4 .	57.1263	0.7115	38.4132	96.251	12496.5	-3180	91	59.23	15.9254

Table B.9: EMPA analysis of run crystal from experiment 12Pt35Zr33 continued

DataSet/Point	Ti	Zr	O	Total	X	Y	Z	Distance (μm)	Mean Z
16 / 5 .	57.7757	0.6995	38.8428	97.318	12512.7	-3168.7	91	78.97	16.0979
16 / 6 .	56.6756	0.7989	38.1427	95.6171	12528.8	-3157.3	91	98.72	15.8396
16 / 7 .	57.1623	0.8722	38.4936	96.5281	12545	-3146	91	118.46	16.0041
16 / 8 .	57.5442	0.9386	38.772	97.2548	12561.2	-3134.7	91	138.2	16.1369
16 / 9 .	56.8747	0.9377	38.3244	96.1367	12577.3	-3123.3	91	157.95	15.9534
16 / 10 .	56.6438	0.9938	38.1899	95.8274	12593.5	-3112	91	177.69	15.9143
16 / 11 .	57.3629	1.1253	38.7164	97.2047	12609.7	-3100.7	91	197.44	16.1673
16 / 12 .	56.8171	1.1492	38.3601	96.3264	12625.8	-3089.3	91	217.18	16.0282
16 / 13 .	56.5916	1.2157	38.2328	96.0401	12642	-3078	91	236.92	15.9951
17 / 1 .	56.593	1.2051	38.23	96.0281	12635	-3078	91	0	15.9909
17 / 2 .	56.5153	1.1087	38.1443	95.7683	12614.8	-3078.9	91	20.22	15.9284
17 / 3 .	56.7075	0.9918	38.2317	95.931	12594.6	-3079.8	91	40.44	15.9309
17 / 4 .	56.8492	1.0221	38.337	96.2084	12574.4	-3080.7	91	60.66	15.9826
17 / 5 .	56.9386	0.9416	38.3685	96.2487	12554.2	-3081.6	91	80.88	15.9726
17 / 6 .	57.3949	0.8049	38.6253	96.825	12534	-3082.5	91	101.1	16.0388
17 / 7 .	57.1948	0.7973	38.489	96.481	12513.8	-3083.4	91	121.32	15.9809
17 / 8 .	57.2783	0.8	38.5458	96.6242	12493.6	-3084.3	91	141.54	16.0049
17 / 9 .	57.8674	0.7505	38.9219	97.5398	12473.4	-3085.2	91	161.76	16.1448
17 / 10 .	57.5857	0.826	38.7602	97.1719	12453.2	-3086.1	91	181.98	16.1001
17 / 11 .	57.8252	0.9262	38.9554	97.7068	12433	-3087	91	202.2	16.2085

Table B.10: EMPA analysis of starting crystal from experiment 04Au24Zr17. The linescan step-size for dataset 8, across the length of the crystal was 41 μm.

DataSet/Point	Ti	Mo	Zr	O	Total	X	Y	Z	Distance (μm)	Mean Z
16 / 1 .	54.4821	0.0307	3.4101	37.6087	95.5315	-14141	-26442	187	0	16.3717
16 / 2 .	54.828	0.0512	3.3962	37.8452	96.1206	-14142.7	-26483.1	187	41.11	16.4698
16 / 3 .	54.4436	0.0447	3.291	37.5482	95.3275	-14144.4	-26524.1	187	82.21	16.3166
16 / 4 .	54.3636	0.0598	3.3185	37.512	95.254	-14146.1	-26565.2	187	123.32	16.3135
16 / 5 .	54.637	0.0539	3.285	37.6799	95.6558	-14147.9	-26606.3	187	164.43	16.3712
16 / 6 .	53.8439	0.0301	3.3083	37.1463	94.3286	-14149.6	-26647.4	187	205.54	16.1533
16 / 7 .	54.0626	0.026	3.2538	37.2713	94.6137	-14151.3	-26688.4	187	246.64	16.1879
16 / 8 .	54.217	0.0279	3.3077	37.3943	94.9469	-14153	-26729.5	187	287.75	16.2541
16 / 9 .	54.303	0.0399	3.283	37.4491	95.0751	-14154.7	-26770.6	187	328.86	16.2726
16 / 10 .	54.6154	0.0311	3.1224	37.597	95.3659	-14156.4	-26811.6	187	369.96	16.2852
16 / 11 .	54.3498	0.0359	3.2863	37.4795	95.1514	-14158.1	-26852.7	187	411.07	16.2849
16 / 12 .	53.4199	0.0445	3.3043	36.8689	93.6376	-14159.9	-26893.8	187	452.18	16.0423
16 / 13 .	54.6264	0.0527	3.312	37.6817	95.6727	-14161.6	-26934.9	187	493.29	16.3793
16 / 14 .	54.3943	0.0552	3.4441	37.5743	95.4679	-14163.3	-26975.9	187	534.39	16.3735
16 / 15 .	54.29	0.036	3.3793	37.4722	95.1775	-14165	-27017	187	575.5	16.3084

Table B.11: EMPA analysis of run crystal from experiment 04Au24Zr17. The linescan step-size for dataset 8, across the length of the crystal was 41 μm.

DataSet/Point	Ti	Mo	Zr	O	Total	X	Y	Z	Distance (μm)	Mean Z
8 / 1 .	56.7687	0.0085	3.1228	39.0244	98.9244	14777	7753	118	0	16.8638
8 / 2 .	57.2884	0.014	2.943	39.3113	99.5567	14759.2	7716.6	117	40.55	16.9314
8 / 3 .	57.5323	0.0301	2.8362	39.4448	99.8434	14741.4	7680.1	117	81.08	16.9598
8 / 4 .	57.447	0.0277	2.8278	39.3837	99.6862	14723.6	7643.7	117	121.62	16.9318
8 / 5 .	57.3646	0.0095	2.6983	39.2741	99.3464	14705.9	7607.3	117	162.16	16.8454
8 / 6 .	57.373	0.0398	2.7272	39.305	99.445	14688.1	7570.9	117	202.7	16.8741
8 / 7 .	57.4888	0.0336	2.8102	39.4084	99.7411	14670.3	7534.4	117	243.23	16.9384
8 / 8 .	57.592	0.0479	2.8146	39.486	99.9405	14652.5	7498	117	283.77	16.9751
8 / 9 .	57.5566	0.0265	2.6885	39.4074	99.679	14634.7	7461.6	117	324.31	16.9016
8 / 10 .	57.3355	0.046	2.7377	39.2867	99.4059	14616.9	7425.1	117	364.85	16.8711
8 / 11 .	57.5873	0.0287	2.7132	39.4377	99.7668	14599.1	7388.7	117	405.39	16.9216
8 / 12 .	57.3366	0.0294	2.6274	39.2405	99.2339	14581.4	7352.3	117	445.92	16.8166
8 / 13 .	57.5189	0.0394	2.7127	39.3971	99.668	14563.6	7315.9	117	486.46	16.9075
8 / 14 .	57.905	0.0382	2.5385	39.5934	100.075	14545.8	7279.4	117	527	16.938
8 / 15 .	57.6258	0.0473	2.4471	39.3794	99.4996	14528	7243	117	567.54	16.8268

Table B.12: EMPA analysis of starting crystal from experiment 05Pt25Zr21. The linescan step-size for dataset 20, across the length of the crystal was 41 μm. Oxygen values are calculated.

DataSet/Point	Ti	Mo	Zr	O	Total	X	Y	Z	Distance (μm)	Mean Z
20 / 1 .	52.7107	0.046	3.438	36.4427	92.6374	-18091	-29171	187	0	15.9063
20 / 2 .	52.9343	0.0586	3.3791	36.5778	92.9498	-18051.1	-29160.7	187	41.16	15.948
20 / 3 .	51.6393	0.0574	3.4284	35.7293	90.8544	-18011.3	-29150.4	187	82.33	15.6144
20 / 4 .	52.0052	0.0332	3.4727	35.9772	91.4884	-17971.4	-29140.1	187	123.49	15.7224
20 / 5 .	52.6473	0.0341	3.4219	36.3888	92.4921	-17931.6	-29129.9	187	164.65	15.8766
20 / 6 .	52.7682	0.0207	3.4548	36.4744	92.7181	-17891.7	-29119.6	187	205.81	15.9176
20 / 7 .	52.6921	0.0487	3.3165	36.3891	92.4464	-17851.9	-29109.3	187	246.98	15.8505
20 / 8 .	52.1623	0.0412	3.4186	36.0672	91.6893	-17812	-29099	187	288.14	15.7458
20 / 9 .	52.6374	0.0565	3.4169	36.3916	92.5024	-17772.1	-29088.7	187	329.3	15.882
20 / 10 .	52.4617	0.0421	3.4384	36.2746	92.2169	-17732.3	-29078.4	187	370.47	15.8366
20 / 11 .	52.6899	0.0296	3.3552	36.3916	92.4664	-17692.4	-29068.1	187	411.63	15.8576
20 / 12 .	52.4256	0.0396	3.3814	36.2292	92.0758	-17652.6	-29057.9	187	452.79	15.8012
20 / 13 .	52.4905	0.0312	3.4574	36.2951	92.2742	-17612.7	-29047.6	187	493.95	15.8476
20 / 14 .	51.9475	0.0498	3.1144	35.8213	90.9329	-17572.9	-29037.3	187	535.12	15.5608
20 / 15 .	53.9805	0.0578	3.3245	37.2571	94.6198	-17533	-29027	187	576.28	16.2103

Table B.13: EMPA analysis of run products from experiment 05Pt25Zr21. The starting crystal from experiment 05Pt25Zr21 contained some possible transport crystals attached to it, which broke into four pieces during removal (A-D below; Figure B.11). The linescan step-size for dataset 1, across the length of the crystal was 14 μm. The linescan step-size for dataset 2, across the length of the crystal was 17 μm. The linescan step-size for dataset 3, across the length of the crystal was 24 μm. The linescan step-size for dataset 4, across the length of the crystal was 33 μm. The linescan step-size for dataset 5, across the length of the crystal was 15 μm. The linescan step-size for dataset 6, across the length of the crystal was 25 μm. The linescan step-size for dataset 7, across the length of the crystal was 50 μm. Oxygen values are calculated.

DataSet/Point	Ti	Mo	Zr	O	Total	X	Y	Z	Distance (μm)	Mean Z
ZrTiO2_X21_A										
1 / 1 .	57.4355	-0.0605	0.8652	38.6434	96.8837	9450	7112	122	0	16.048
1 / 2 .	58.0187	-0.0511	0.7952	39.0131	97.7759	9439.4	7103.6	121	13.61	16.1818
1 / 3 .	58.1451	-0.0624	0.833	39.1051	98.0207	9428.7	7095.1	121	27.17	16.2273
1 / 4 .	57.8616	-0.0524	0.8488	38.9263	97.5842	9418.1	7086.7	121	40.74	16.1612
1 / 5 .	57.741	-0.0463	0.9176	38.8729	97.4852	9407.4	7078.3	120	54.34	16.1604
1 / 6 .	57.7691	-0.0597	0.9592	38.8996	97.5681	9396.8	7069.9	120	67.91	16.1797
1 / 7 .	57.9705	-0.0588	0.9741	39.0398	97.9255	9386.1	7061.4	120	81.48	16.2416
1 / 8 .	57.6151	-0.0664	0.9922	38.805	97.3459	9375.5	7053	120	95.05	16.1487
1 / 9 .	57.8927	-0.0503	0.9951	38.9995	97.837	9364.9	7044.6	119	108.65	16.2333
1 / 10 .	57.6007	-0.0574	1.0765	38.8294	97.4492	9354.2	7036.1	119	122.22	16.185
1 / 11 .	57.8806	-0.0675	1.0751	39.0109	97.8991	9343.6	7027.7	119	135.79	16.2563
1 / 12 .	58.1494	-0.0704	1.0504	39.1803	98.3097	9332.9	7019.3	118	149.39	16.3179
1 / 13 .	58.1492	-0.0525	1.0948	39.2047	98.3962	9322.3	7010.9	118	162.96	16.3451
1 / 14 .	57.5812	-0.0523	1.1304	38.8379	97.4972	9311.6	7002.4	118	176.54	16.2051
1 / 15 .	57.4779	-0.0503	1.0953	38.7575	97.2804	9301	6994	118	190.11	16.1627
ZrTiO2_X21_B										
2 / 1 .	57.3044	0.0419	3.1975	39.4252	99.9689	10260	7037	122	0	17.0576
2 / 2 .	57.2196	0.0348	3.2071	39.3684	99.8299	10276.9	7033.1	122	17.33	17.0353
2 / 3 .	57.2066	0.0506	3.343	39.4153	100.0156	10293.8	7029.2	122	34.66	17.0972
2 / 4 .	56.9632	0.0195	3.3227	39.2299	99.5353	10310.7	7025.3	122	51.99	17.0076

Table B.13: EMPA analysis of run crystal from experiment 05Pt25Zr21 continued

DataSet/Point	Ti	Mo	Zr	O	Total	X	Y	Z	Distance (μm)	Mean Z
2 / 5 .	57.1255	0.011	3.4042	39.3627	99.9034	10327.6	7021.4	122	69.32	17.0829
2 / 6 .	59.1373	-0.0486	0.7617	39.7499	99.6004	10344.4	7017.6	122	86.65	16.4745
2 / 7 .	59.3875	-0.0618	0.7267	39.8982	99.9506	10361.3	7013.7	122	103.98	16.5218
2 / 8 .	59.3622	-0.0528	0.754	39.8954	99.9588	10378.2	7009.8	122	121.32	16.5308
2 / 9 .	57.8946	0.0058	2.7504	39.6446	100.2953	10395.1	7005.9	122	138.65	17.011
2 / 10 .	59.4806	-0.0621	0.4489	39.8628	99.7303	10412	7002	122	155.98	16.4283
3 / 1 .	57.1652	0.0519	3.1538	39.3219	99.6927	10369	7079	122	0	17.0054
3 / 2 .	57.1325	0.0384	3.2327	39.3209	99.7246	10359.8	7057.2	122	23.65	17.0241
3 / 3 .	58.9618	-0.0569	0.7754	39.6333	99.3137	10350.6	7035.4	122	47.3	16.4285
3 / 4 .	59.808	-0.0481	0.6334	40.1532	100.5464	10341.3	7013.7	122	70.95	16.6031
3 / 5 .	57.8292	0.0524	2.1033	39.3972	99.3822	10332.1	6991.9	122	94.6	16.7376
3 / 6 .	57.9329	0.0343	2.3151	39.5317	99.814	10322.9	6970.1	122	118.25	16.8482
3 / 7 .	57.3414	0.0348	2.5437	39.217	99.137	10313.7	6948.3	122	141.9	16.7846
3 / 8 .	55.4392	0.0461	2.4266	37.9108	95.8226	10304.4	6926.6	122	165.55	16.2195
3 / 9 .	59.2467	-0.0529	0.3522	39.6772	99.2232	10295.2	6904.8	122	189.2	16.3271
3 / 10 .	59.3024	-0.047	0.5168	39.7751	99.5472	10286	6883	122	212.85	16.4155
ZrTiO2_X21_C										
4 / 1 .	59.1337	-0.0562	0.9802	39.8203	99.878	10847	6975	125	0	16.5635
4 / 2 .	59.2723	-0.0608	0.9739	39.9084	100.0938	10876.8	6960.7	125	33.05	16.5966
4 / 3 .	58.8328	-0.06	0.9885	39.6204	99.3816	10906.6	6946.3	125	66.1	16.483
4 / 4 .	58.9785	-0.0676	0.9692	39.7071	99.5872	10936.3	6932	125	99.14	16.5111
4 / 5 .	59.3538	-0.0639	0.8996	39.9353	100.1247	10966.1	6917.7	125	132.19	16.5857
4 / 6 .	58.9369	-0.0578	0.9549	39.6792	99.5132	10995.9	6903.3	125	165.24	16.4981
4 / 7 .	59.0709	-0.0604	0.9739	39.7741	99.7585	11025.7	6889	125	198.29	16.5417
4 / 8 .	58.7587	-0.0626	1.2011	39.6441	99.5413	11055.4	6874.7	125	231.33	16.5526
4 / 9 .	58.6094	-0.0428	1.2663	39.5772	99.41	11085.2	6860.3	125	264.38	16.5488
4 / 10 .	58.8239	-0.0759	0.97	39.6	99.318	11115	6846	125	297.43	16.4654

Table B.13: EMPA analysis of run crystal from experiment 05Pt25Zr21 continued

DataSet/Point	Ti	Mo	Zr	O	Total	X	Y	Z	Distance (μm)	Mean Z
ZrTiO2_X21_D										
5 / 1 .	59.3509	-0.0685	0.8728	39.9216	100.0768	11949	6689	118	0	16.5713
5 / 2 .	59.3709	-0.0681	0.8567	39.9295	100.089	11961.1	6680.7	118	14.7	16.57
5 / 3 .	59.3867	-0.0604	0.8303	39.9347	100.0913	11973.2	6672.3	118	29.4	16.5666
5 / 4 .	59.7318	-0.0554	0.78	40.1501	100.6065	11985.3	6664	118	44.1	16.6417
5 / 5 .	59.4924	-0.0576	0.8054	39.998	100.2382	11997.4	6655.7	118	58.8	16.5862
5 / 6 .	59.2213	-0.0479	0.823	39.8279	99.8244	12009.6	6647.3	118	73.51	16.524
5 / 7 .	56.0816	-0.0624	0.764	37.7024	94.4856	12021.7	6639	118	88.21	15.6335
5 / 8 .	59.5045	-0.0513	0.8407	40.0216	100.3154	12033.8	6630.7	118	102.91	16.6074
5 / 9 .	58.8628	-0.0554	0.8393	39.5903	99.237	12045.9	6622.3	118	117.61	16.4295
5 / 10 .	59.3617	-0.0592	0.9297	39.9534	100.1855	12058	6614	118	132.31	16.6028
6 / 1 .	59.5965	-0.0568	0.7316	40.042	100.3132	12281	6895	118	0	16.5834
6 / 2 .	59.3665	-0.0777	0.7845	39.8965	99.9697	12288	6870.7	118	25.32	16.5335
6 / 3 .	59.3071	-0.0561	0.7208	39.8453	99.8171	12295	6846.3	118	50.64	16.5
6 / 4 .	59.4077	-0.0643	0.7541	39.92	100.0175	12302	6822	118	75.96	16.5379
6 / 5 .	59.5614	-0.0682	0.768	40.0256	100.2868	12309	6797.7	118	101.28	16.5841
6 / 6 .	59.5485	-0.0568	0.7633	40.0211	100.276	12316	6773.3	118	126.6	16.5838
6 / 7 .	59.352	-0.0674	0.6685	39.8513	99.8045	12323	6749	118	151.92	16.4847
6 / 8 .	59.3477	-0.0567	0.7239	39.8731	99.888	12330	6724.7	118	177.24	16.5121
6 / 9 .	59.4204	-0.0566	0.7918	39.9456	100.1012	12337	6700.3	118	202.56	16.5611
6 / 10 .	58.9806	-0.0485	0.7508	39.6415	99.3244	12344	6676	118	227.88	16.427
7 / 1 .	59.5376	-0.0648	0.9518	40.0759	100.5005	12304	7179	118	0	16.6578
7 / 2 .	59.2313	-0.0566	0.928	39.8671	99.9699	12344.7	7150.1	118	49.88	16.5677
7 / 3 .	58.9268	-0.0545	0.8657	39.6428	99.3808	12385.3	7121.2	118	99.77	16.4587
7 / 4 .	59.4432	-0.064	0.9607	40.0164	100.3562	12426	7092.3	118	149.65	16.6362
7 / 5 .	59.1071	-0.054	1.1158	39.8512	100.0201	12466.7	7063.4	118	199.53	16.6153
7 / 6 .	59.0752	-0.0762	1.0298	39.7887	99.8175	12507.3	7034.6	118	249.42	16.5596

Table B.13: EMPA analysis of run crystal from experiment 05Pt25Zr21 continued

DataSet/Point	Ti	Mo	Zr	O	Total	X	Y	Z	Distance (μm)	Mean Z
7 / 7 .	59.3432	-0.0581	1.0034	39.9675	100.256	12548	7005.7	118	299.3	16.6299
7 / 8 .	59.3844	-0.0651	0.9755	39.9818	100.2766	12588.7	6976.8	118	349.18	16.626
7 / 9 .	59.3543	-0.0537	1.0088	39.979	100.2883	12629.3	6947.9	118	399.07	16.6372
7 / 10 .	59.0962	-0.0573	1.1277	39.8465	100.013	12670	6919	118	448.95	16.6159